Modulation of Charge Distribution in Cobalt-α-Diimine Complexes toward Valence Tautomerism

Moya A Hay, Jett T Janetzki, Varshini J Kumar, Robert W Gable, Rodolphe Clérac, Alyona A Starikova, Paul J Low, Colette Boskovic

Modulation of Charge Distribution in Cobalt-α-Diimine Complexes toward Valence Tautomerism

Moya A. Hay,[⊥] Jett T. Janetzki,[⊥] Varshini J. Kumar, Robert W. Gable, Rodolphe Clérac, Alyona A. Starikova, Paul J. Low, and Colette Boskovic*

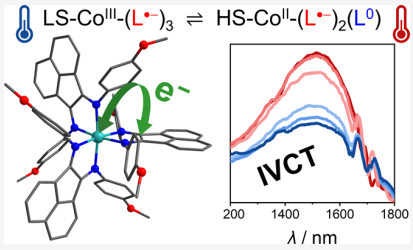

Valence tautomerism (VT) and spin crossover (SCO) are promising avenues for developing a range of molecular materials for sensing, memory, and optoelectronic applications. However, these phenomena arise only when specific metal−ligand combinations are employed. The underexplored combination of cobalt(II/III) paired with bis((aryl)imino)acenapthene (Ar-BIAN) ligands, which can exist as neutral Ar-BIAN^0 (L^0), monoanionic radical Ar-BIAN$^{\bullet-}$ (L$^{\bullet-}$), and dianionic Ar-BIAN^{2-} (L^{2-}) forms, has potential to afford both VT and SCO. Aiming to develop a new family of switchable molecules, we systematically explored a dual-tuning approach by varying the redox state and aryl substituents in a series of homoleptic $[Co(Ar\text{-}BIAN)_3]^{n+}$ complexes (Ar = Ph, n = 2 (**1**$^{2+}$), 1 (**1**$^+$), 0 (**1**); Ar = 3,5-CF_3-Ph, n = 0 (**2**); Ar = 4-MeO-Ph, n = 2 (**3**$^{2+}$), 0 (**3**)). As a prelude to synthetic and experimental studies, density functional theory (DFT) calculations were used to explore the structure and relative energies of the different electronic forms of each complex, comprising different cobalt oxidation and spin states and different ligand oxidation states. Except for compound **3**, DFT identified a HS-Co^{II}-L^0 containing ground state for all complexes, precluding thermally induced SCO or VT. For **3**, calculations suggested a possible thermally accessible LS-Co^{III}-(L$^{\bullet-}$)$_3$ ⇌ HS-Co^{II}-(L$^{\bullet-}$)$_2$(L^0) VT interconversion. Experimentally, structural and magnetic data reveal a HS-Co^{II}-L^0 containing ground state for all six compounds in the solid state, including **3**, discounting thermally induced VT or SCO. In solution, electrochemical and spectroscopic analysis also indicate that all compounds exist as the HS-Co^{II}-L^0-containing electromer at 298 K. Intervalence charge transfer (IVCT) bands observed for neutral **1**, **2**, and **3** at room temperature suggest the mixed-valence HS-Co^{II}-(L$^{\bullet-}$)$_2$(L^0) charge distribution. However, cooling **3** to 243 K in acetonitrile uniquely affords a substantial reduction in the intensity of this IVCT band, consistent with thermally induced VT interconversion to the LS-Co^{III}-(L$^{\bullet-}$)$_3$ ground state as predicted by DFT calculations. This study emphasizes the utility of computationally guided molecular design for complicated systems with redox activity at the metal and multiple ligands, thus opening new avenues for tuning electronic structure and developing new families of switchable molecules.

Research into molecular materials has flourished over the past several decades, with the potential to facilitate the miniaturization of current technologies.[1−4] To this end, a variety of functional molecules have been investigated within innovative device structures, with a view to introducing, for example, spintronic effects, quantum information processing, and sensing behavior.[5−12] A simple molecular functionality arises from the ability to reversibly switch between energetically accessible states upon application of some stimulus, with accompanying changes in chemical and physical properties.[13−16] The phenomenon of spin crossover (SCO), where coordination compounds undergo a metal-centered spin-state change from low spin (LS) to high spin (HS) in response to changes in temperature or pressure or on application of light, has been extensively described in the literature and represents a classic example molecular switching behavior.[14,17,18] Further degrees of control over molecular electronic and magnetic properties can be engineered in metal complexes that incorporate redox-active ligands. In certain circumstances, such complexes can be stimulated to switch between states through intramolecular metal−ligand charge transfer in a process known as valence tautomerism (VT).[16,19] As a consequence of the complex interplay between metal ion and ligand redox states, valence tautomeric complexes offer fascinating potential for redox (electrical) control of materials properties when integrated into devices.[9,20−23]

Cobalt complexes have proven capable of exhibiting either SCO or VT in the presence of a suitable ligand environment.[19,24−26] Spin crossover in cobalt complexes is most prevalent with N-donor ligands,[26,27] the archetypal example

being $[Co(terpy)_2]^{2+}$ (terpy = 2,2′:6′,2″-terpyridine),[28−30] and derivatives.[31,32] While valence tautomerism in cobalt systems has been most commonly observed with complexes bearing redox-active O-donor ortho-dioxolene ligands,[16,19] recent reports of VT in cobalt complexes featuring redox-active N-donor ligands hint at enticing opportunities to expand switchable behavior through the rational design of complexes able to exhibit either SCO or VT.[33,34]

In the context of switching systems with a dual mode of action, the bis((aryl)imino)acenapthene (Ar-BIAN) ligand family provides a promising basis for exploration.[35−39] The Ar-BIAN ligands are characterized by rich-redox chemistry, comparable to ortho-dioxolene ligands, and are readily accessible in the neutral Ar-BIAN^0 (L^0), monoanionic radical Ar-BIAN$^{\bullet-}$ ($L^{\bullet-}$), and dianionic Ar-BIAN^{2-} (L^{2-}) forms (Scheme 1).[40] Second, the straightforward synthesis of these

Scheme 1. Neutral Ar-BIAN^0 (L^0), Monoanionic Ar-BIAN$^{\bullet-}$ ($L^{\bullet-}$), and Dianionic Ar-BIAN^{2-} (L^{2-}) Redox States

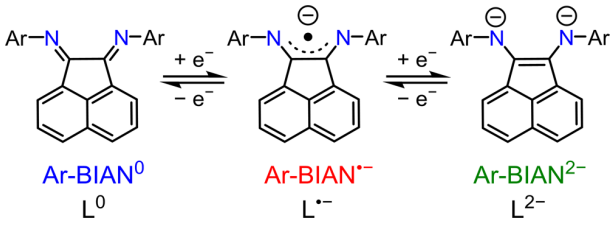

bis(α-diimine) compounds via condensation of acenaphthenequinone with 2 equiv of an aryl amine (Ar-NH_2) allows for convenient tuning of the electronic properties via variation of the aryl (Ar) substituents,[41] a factor that is important in modulating the relative energies of the different charge distributions.[42−44] An Fe(II) compound has been reported to undergo SCO when coordinated with bis[(phenyl)imino]-acenaphthene (Ph-BIAN) in the $L^{\bullet-}$ state,[45] and VT has been reported involving the L^{2-} and $L^{\bullet-}$ states of bis[(1,4-bis(2,6−diisopropyl)phenyl)imino]acenaphthene with ytterbium(II/III) and bis[(3,5-bis(dimethyl)phenyl)imino]acenaphthene with vanadium(IV/V).[36,37,46] A density functional theory (DFT) study has also predicted VT behavior in a series of octahedral heteroleptic $[Co(Ph\text{-}BIAN)(L^{NO})_2]$ and $[Co(H\text{-}BIAN)(L^{NO})_2]$ complexes (H-BIAN = bis(imino)-acenaphthene; L^{NO} = iminovinylketonate ligand) involving the LS-Co^{III}-$L^{\bullet-}$ and HS-Co^{II}-L^0 tautomers.[47] The synthetic challenges associated with preparing the complexes used in that computational study prompted attention here to be focused on the preparation of a series of homoleptic $[Co(Ar\text{-}BIAN)_3]^{n+}$ complexes to gain a deeper understanding of the redox chemistry of these species, and how charge distribution within the molecular framework may be influenced by the the formal redox state of the metal and ligand(s) and the electronic nature of the supporting aryl groups.[48]

Pursuing a strategy to achieve VT or SCO behavior in homoleptic Ar-BIAN Co complexes, we adopted a dual approach examining: (1) the impact of the Ar-BIAN oxidation state on the electronic structure of $[Co(Ar\text{-}BIAN)_3]^{n+}$ (n = 0−2) and (2) the influence of substituents on the Ar-BIAN aryl (Ar) group. First, we focused on the case of complexes derived from Ph-BIAN with the redox ladder $[Co(Ph\text{-}BIAN)_3]^{2+}$ (**1**$^{2+}$), $[Co(Ph\text{-}BIAN)_3]^{+}$ (**1**$^{+}$), and $[Co(Ph\text{-}BIAN)_3]$ (**1**) (Scheme 2). Subsequently, we turned our attention to complexes with

Scheme 2. Representation of the $[Co(Ar\text{-}BIAN)_3]^{n+}$ (n = 0, 1, 2) Complexes and the Ar-BIAN Ligands Used in This Work, with Numbering Scheme[a]

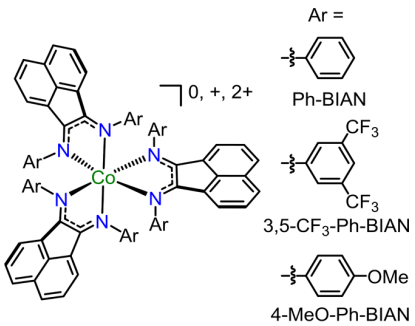

$[Co(Ph\text{-}BIAN)_3]^{2+}$	(**1**$^{2+}$)
$[Co(Ph\text{-}BIAN)_3]^{+}$	(**1**$^{+}$)
$[Co(Ph\text{-}BIAN)_3]$	(**1**)
$[Co(3,5\text{-}CF_3\text{-}Ph\text{-}BIAN)_3]$	(**2**)
$[Co(4\text{-}MeO\text{-}Ph\text{-}BIAN)_3]$	(**3**)
$[Co(4\text{-}MeO\text{-}Ph\text{-}BIAN)_3]^{2+}$	(**3**$^{2+}$)

[a]The cationic complexes were isolated as PF_6^- salts.

the ligands bis[(3,5-bis(trifluoromethyl)phenyl)imino]-acenaphthene (3,5-CF_3-Ph-BIAN) and bis[(4-methoxyphenyl)imino]acenaphthene (4-MeO-Ph-BIAN), which feature electron-withdrawing (CF_3) and electron-donating (OMe) substituents on the aryl rings, respectively, to isolate compounds: $[Co(3,5\text{-}CF_3\text{-}Ph\text{-}BIAN)_3]$ (**2**), $[Co(4\text{-}MeO\text{-}Ph\text{-}BIAN)_3]$ (**3**), and $[Co(4\text{-}MeO\text{-}Ph\text{-}BIAN)_3]^{2+}$ (**3**$^{2+}$) (Scheme 2). An initial density functional theory (DFT) survey was carried out to identify the most promising candidates for VT or SCO. The complexes were synthesized with the cationic complexes isolated as hexaflurophosphate salts, and a systematic study of this family of complexes was carried out in their various redox forms in both the solid and solution state. The focus was on establishing the electronic structure (Co oxidation- and spin-state, and ligand oxidation states) adopted by each compound and exploring the possibility of thermally-induced SCO or VT switchable behavior. The electronic structure of the compounds can differ in the solid vs solution state. Through this study of the electronic structure and redox properties of this series of compounds, we achieved the targeted VT behavior and illuminate a strategy to achieve switchable behavior in $Co(Ar\text{-}BIAN)_3$ compounds.

Density Functional Theory. To provide a guide prior to synthetic work and subsequent experimental studies, an initial survey of the electronic structures and the relative stability of **1**$^{2+}$(PF_6)$_2$, **1**$^{+}$(PF_6), **1**, **2**, **3**, and **3**$^{2+}$(PF_6)$_2$ was carried out using density functional theory (DFT) calculations based on optimized gas-phase geometries (Tables S1−S3; Figures S1−S6). The electromer energies (E, kcal mol^{-1}) were calculated using the UTPSSh/6-311++G(d,p)[49,50] DFT method (Table S4) with the inclusion of zero-point energy (ZPE) in Gaussian 16,[51] a method that has previously been successful in the

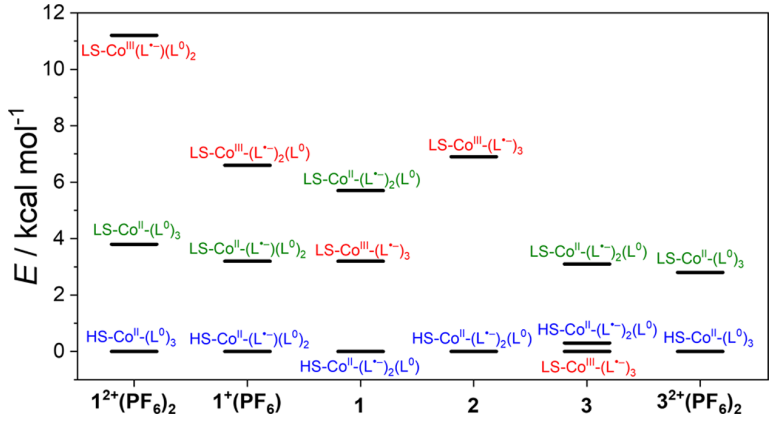

Figure 1. Calculated relative energies of the three different electronic forms for the cobalt Ar-BIAN complexes in compounds $\mathbf{1}^{2+}(\mathbf{PF_6})_2$, $\mathbf{1}^{+}(\mathbf{PF_6})$ **1**, **2**, **3**, and $\mathbf{3}^{2+}(\mathbf{PF_6})_2$ calculated by DFT (UTPSSh/6-311++G(d,p)) with zero-point energy.

calculation of electromer energies for cobalt complexes with redox-active ligands.[24,52−55] It is important to note that factors such as lattice effects and solvent can complicate the straightforward translation of relative energies from calculations performed on isolated molecules in the gas phase to experimental systems.

For these homoleptic $[Co(Ar\text{-}BIAN)_3]^{n+}$ complexes, three electronic states were considered in each case. Compounds $\mathbf{1}^{2+}(\mathbf{PF_6})_2$ and $\mathbf{3}^{2+}(\mathbf{PF_6})_2$ can adopt HS-Co^{II}-$(L^0)_3$, LS-Co^{II}-$(L^0)_3$ or LS-Co^{III}-$(L^{\bullet-})(L^0)_2$; $\mathbf{1}^{+}(\mathbf{PF_6})$ can adopt HS-Co^{II}-$(L^{\bullet-})(L^0)_2$, LS-Co^{II}-$(L^{\bullet-})(L^0)_2$, or LS-Co^{III}-$(L^{\bullet-})_2(L^0)$; and **1**, **2**, and **3** can adopt HS-Co^{II}-$(L^{\bullet-})_2(L^0)$, LS-Co^{II}-$(L^{\bullet-})_2(L^0)$, or LS-Co^{III}-$(L^{\bullet-})_3$. For simplification, we refer to the electronic states in abbreviated form as containing the HS-Co^{II}-L^0, LS-Co^{II}-L^0, or LS-Co^{III}-$L^{\bullet-}$ moieties that are conserved accross all three oxidation states of the complexes.

In general, thermally induced SCO and VT interconversions would require respective LS-Co^{II}-L^0 or LS-Co^{III}-$L^{\bullet-}$ containing ground states and the HS-Co^{II}-L^0 containing tautomer destabilized by no more than 12 kcal mol^{-1}.[52,54] Thermally induced SCO and VT are both entropically driven, with the HS-Co^{II}-L^0 containing electromer favored upon increasing temperature due to the increase in entropy associated with longer bond lengths, higher density of vibrational states, and greater spin-degeneracy of the charge distribution.[19]

The Ph-BIAN redox family of compounds ($\mathbf{1}^{2+}(\mathbf{PF_6})_2$, $\mathbf{1}^{+}(\mathbf{PF_6})$, and **1**) were first investigated to examine the impact of successive reductions of the Ph-BIAN ligands on the relative energies of the different electromers (Figure 1). In all three cases, the HS-Co^{II}-L^0 containing electromer was found to be the ground state, with the LS-Co^{II}-L^0- and LS-Co^{III}-$L^{\bullet-}$ containing electromers at higher energies. Thus, the calculations suggest that $\mathbf{1}^{2+}(\mathbf{PF_6})_2$, $\mathbf{1}^{+}(\mathbf{PF_6})$, and **1** should remain in the HS-Co^{II}-L^0 containing state at all temperatures with no possibility of either VT or SCO interconversions.

However, the relative energy of the LS-Co^{III}-$L^{\bullet-}$ containing electromer decreases with the total charge of the complex, following $\mathbf{1}^{2+}(\mathbf{PF_6})_2$ > $\mathbf{1}^{+}(\mathbf{PF_6})$ > **1** (Figure 1). This is attributed to the increasing electron donation arising from the successive introduction of anionic Ph-BIAN$^{\bullet-}$ ligands that stabilizes the shorter bond lengths associated with LS-Co^{III}. This provides a critical insight for accessing VT as it suggests that neutral $[Co(Ar\text{-}BIAN)_3]$ complexes are more promising than the cationic complexes for achieving the LS-Co^{III}-$L^{\bullet-}$ containing ground state necessary for an LS-Co^{III}-$L^{\bullet-}$ ⇌ HS-Co^{II}-L^0-based VT interconversion. On the other hand, an LS-Co^{II}-L^0 ground state and subsequent SCO appear to be inaccessible with this family. These observations prompted explorations of variation of substituents on the Ar-BIAN ligand to further stabilize the LS-Co^{III}-$L^{\bullet-}$ state, focusing on the neutral compounds. Neutral compounds $[Co(3,5\text{-}CF_3\text{-}Ph\text{-}BIAN)_3]$ (**2**) and $[Co(4\text{-}MeO\text{-}Ph\text{-}BIAN)_3]$ (**3**), containing Ar-BIAN ligands with the most electron-withdrawing and -donating substituents, respectively, were selected for further exploration.[56,57]

The DFT calculations of complex **2** indicate that the electron-withdrawing 3,5-CF_3-Ph-BIAN ligand significantly destabilizes the LS-Co^{III}-$(L^{\bullet-})_3$ electromer from the HS-Co^{II}-$(L^{\bullet-})_2(L^0)$ ground state (Figure 1), and thus VT is not accessible. In contrast, the strongly electron-donating methoxy groups of 4-MeO-Ph-BIAN in complex **3** result in the reversal of the energy ordering of the states and afford the LS-Co^{III}-$(L^{\bullet-})_3$ tautomer as lowest in energy, albeit with the HS-Co^{II}-$(L^{\bullet-})_2(L^0)$ state in very close proximity (0.3 kcal mol^{-1}). This suggests the possibility of a thermally induced LS-Co^{III}-$(L^{\bullet-})_3$ ⇌ HS-Co^{II}-$(L^{\bullet-})_2(L^0)$ VT interconversion (Scheme 3) for **3**.

Neutral $[Co(Ar\text{-}BIAN)_3]$ complexes with several other aryl substituents with a range of Hammett σ-parameters were also

Scheme 3. Valence Tautomeric Equilibrium Predicted for Compound 3 via DFT

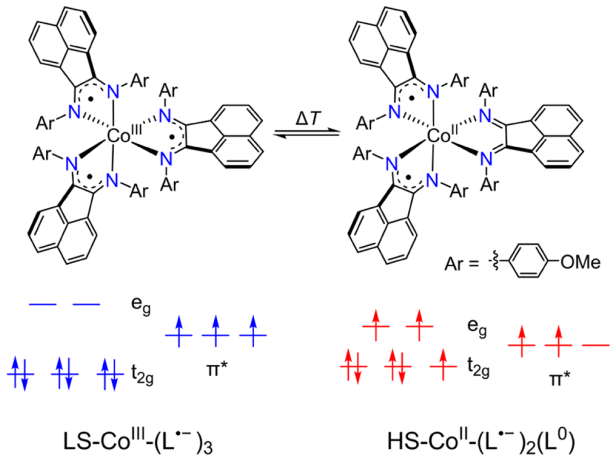

explored (Figure S7), with a clear linear trend showing stabilization of the LS-Co^{III}-$(L^{\bullet-})_3$ state with increasing electron donation (Figure S8). The ground state of $\mathbf{3}^{2+}(\mathbf{PF_6})_2$, as in the case of $\mathbf{1}^{2+}(\mathbf{PF_6})_2$, was found to be the HS-Co^{II}-$(L^0)_3$ electromer, with the LS-Co^{II}-$(L^0)_3$ electromer relatively destabilized (Figure 1). In addition, for $\mathbf{3}^{2+}(\mathbf{PF_6})_2$, numerous attempts to find the LS-Co^{III}-$(L^{\bullet-})(L^0)_2$ electromer invariably gave the LS-Co^{II}-$(L^0)_3$ state on the potential energy surface of the same multiplicity (S = 1/2), due to the symmetric structure being more energetically preferable. The computational results thus clearly suggest that of the compounds investigated here, the combination of the maximum number of monoanionic Ar-BIAN$^{\bullet-}$ ligands and electron-donating ligand substituents incorporated into **3** afford the best prospects for achieving VT.

Exchange coupling parameters can alter the relative energy stabilization of the different charge distributions and must be considered for electromers where at least two open-shell sites (HS-Co^{II}, LS-Co^{II}, and $L^{\bullet-}$) are present (which excludes all electromers of dicationic compounds $\mathbf{1}^{2+}(\mathbf{PF_6})_2$ and $\mathbf{3}^{2+}(\mathbf{PF_6})_2$). Exchange spin coupling parameters J ($-2J\hat{S}_1\cdot\hat{S}_2$ formalism) were estimated using the broken symmetry (BS) approximation (Table S5).[58] In this method, the calculated exchange is isotropic and does not consider spin−orbit coupling (SOC) contributions. Unfortunately, at the level of theory employed, an exact value of the exchange cannot be conclusively determined, particularly in the case of anisotropic ions such as HS-Co^{II}.[43,59,60] However, it is nonetheless important to consider, due to the likelihood of magnetic exchange interactions in such systems.

For compound $\mathbf{1}^{+}(\mathbf{PF_6})$, in the HS-$Co^{II}$-$(L^{\bullet-})(L^0)_2$ state, very strong antiferromagnetic exchange (−620 cm^{-1}) was calculated between HS-Co^{II} and $L^{\bullet-}$, whereas weaker ferromagnetic exchange (39 cm^{-1}) was predicted between LS-Co^{II} and $L^{\bullet-}$ for the LS-Co^{II}-$(L^{\bullet-})(L^0)_2$ state. For the LS-Co^{III}-$(L^{\bullet-})_2(L^0)$ electromer of $\mathbf{1}^{+}(\mathbf{PF_6})$, only a moderate antiferromagnetic $L^{\bullet-}\cdots L^{\bullet-}$ interaction (−21 cm^{-1}) was calculated. For compound **1**, the HS-Co^{II}-$(L^{\bullet-})_2(L^0)$ tautomer is suggested to have strong antiferromagnetic exchange (−143 cm^{-1}) between the HS-Co^{II} center and the $L^{\bullet-}$ ligands, as well as a competing strong antiferromagnetic $L^{\bullet-}\cdots L^{\bullet-}$ interaction (−218 cm^{-1}). For the LS-Co^{II}-$(L^{\bullet-})_2(L^0)$ state of **1**, strong ferromagnetic coupling (400 cm^{-1}) is instead predicted between the LS-Co^{II} center and the $L^{\bullet-}$ ligands, with a moderate $L^{\bullet-}\cdots L^{\bullet-}$ ferromagnetic exchange (47 cm^{-1}). In the LS-Co^{III}-$(L^{\bullet-})_3$ electromer of **1**, moderate ferromagnetic exchange is calculated (32 cm^{-1}) between the $L^{\bullet-}$ ligands. The magnitude and sign of the exchange coupling parameters for the three analogous electromers in compounds **2** and **3** are similar to those of **1** (Table S5). For the HS-Co^{II}-$(L^{\bullet-})_2(L^0)$ electromers of **2** and **3**, again antiferromagnetic HS-$Co^{II}\cdots L^{\bullet-}$ (−76 and −498 cm^{-1}, respectively) and $L^{\bullet-}\cdots L^{\bullet-}$ (−401 and −30 cm^{-1}, respectively) interactions were calculated. Notably calculations for **3** suggest a significantly larger HS-$Co^{II}\cdots L^{\bullet-}$ coupling constant than for **1** and **2**. As per **1**, the $L^{\bullet-}\cdots L^{\bullet-}$ exchange in the LS-Co^{III}-$(L^{\bullet-})_3$ electromer for **2** (50 cm^{-1}) and **3** (46 cm^{-1}) is calculated to be weakly ferromagnetic. For the LS-Co^{II}-$(L^{\bullet-})_2(L^0)$ state of **3**, similar strong ferromagnetic LS-$Co^{II}\cdots L^{\bullet-}$ and $L^{\bullet-}\cdots L^{\bullet-}$ interactions (493 and 112 cm^{-1}, respectively) are obtained from the calculations. For **1**, **2**, and **3**, the strong exchange interactions (Table S5) predicted for the different energetically accessible electromers are expected to have a pronounced impact on the experimentally observed charge distributions. For example, if compounds **1**, **2**, and/or **3** are isolated in the HS-Co^{II}-$(L^{\bullet-})_2(L^0)$ charge distribution, the predicted large antiferromagnetic HS-$Co^{II}\cdots L^{\bullet-}$ and $L^{\bullet-}\cdots L^{\bullet-}$ coupling may result in lower-than-expected magnetic response.

The combined DFT results therefore set out a series of structure−property relationships and predictions of the electronic and magnetic properties of this family of Ar-BIAN complexes in their various redox states. Of the six compounds calculated, the most promising candidate for achieving molecular switchability was determined to be neutral compound **3**, which is calculated to have the necessary energy ordering of the LS-Co^{III}-$(L^{\bullet-})_3$ and HS-Co^{II}-$(L^{\bullet-})_2(L^0)$ electromers to possibly achieve thermally induced VT (Scheme 3). Next, our attention turned to experimental verification, with a focus on establishing the electronic state of the six compounds in the solid and solution state, as well as determining whether **3** displays thermally induced VT.

Synthesis. As detailed in the Supporting Information, compounds $\mathbf{1}^{2+}(\mathbf{PF_6})_2$ and $\mathbf{3}^{2+}(\mathbf{PF_6})_2$ were synthesized by reacting cobalt acetate ($Co(OAc)_2$) with 3 equiv of Ph-BIAN or 4-MeO-Ph-BIAN in air, with subsequent addition of 2 equiv of PF_6^- as counterions, yielding a red precipitate. The compound was recrystallized by layering a concentrated dichloroethane (DCE) solution with diisopropyl ether (iPr$_2$O). The higher-boiling-point DCE and iPr$_2$O solvents (compared to dichloromethane and diethyl ether) were chosen to limit solvent loss from the bulk crystalline sample. Compound $\mathbf{1}^{+}(\mathbf{PF_6})$ was synthesized in tetrahydrofuran (THF) under N_2 by first forming complex $[Co(Ph\text{-}BIAN)]^{2+}$, followed by reduction with 1 equiv of cobaltocene ($CoCp_2$). The product was isolated as the PF_6^- salt and recrystallized from acetonitrile (MeCN) and diethyl ether (Et_2O). An analytically pure bulk sample of $\mathbf{1}^{+}(\mathbf{PF_6})$ could not be consistently obtained due to its similar solubility with the $(CoCp_2)(PF_6)$ byproduct.

Synthesis of neutral **2** was achieved by reaction of 6 equiv of 3,5-CF_3-Ph-BIAN with $Co_2(CO)_8$, in toluene under N_2, in a process that leads to in situ reduction of 3,5-CF_3-Ph-BIAN by the Co(0) source. The complex was subsequently isolated as dark purple crystals. Compound **2** has been previously reported from a different synthetic method,[61] and while originally formulated as $[Co^{I}(3,5\text{-}CF_3\text{-}Ph\text{-}BIAN^{\bullet-})(3,5\text{-}CF_3\text{-}Ph\text{-}BIAN^{0})_2]$, consideration of the crystallographically determined bond lengths suggests that this description is not definitive (see the Structure Description section). Attempts to synthesize neutral **1** and **3** using the same procedure for **2** yielded a mixture of products, presumably due to the lower reduction potentials of Ph-BIAN and 4-MeO-Ph-BIAN. Instead, a comproportionation approach was developed. The reaction of a 2:1 combination of Ar-BIAN and Ar-BIAN^{2-} (Ar = Ph and 4-MeO-Ph) resulted in the formation of 2 equiv of Ar-BIAN$^{\bullet-}$ and one Ar-BIAN. Subsequent addition of $Co(OAc)_2$ to this ligand mixture allowed the formation and isolation of neutral compounds **1** and **3**. The compounds were separated from NaOAc byproduct by extraction of the compound into toluene, and then washing with ethanol. Elemental and thermogravimetric analysis (Figure S9) confirmed the purity and solvation of all five compounds (**1**, **2**, **3**, $\mathbf{1}^{2+}(\mathbf{PF_6})_2$, $\mathbf{3}^{2+}(\mathbf{PF_6})_2$). In solution, **1**, **2**, and **3** are highly air-sensitive and also unstable, decomposing after 4−5 h even under inert conditions.

Structure Descriptions. Structures of $\mathbf{1}^{2+}(\mathbf{PF_6})_2$, $\mathbf{1}^{+}(\mathbf{PF_6})$, **1**, **2**, **3**, and $\mathbf{3}^{2+}(\mathbf{PF_6})_2$ were determined by single-crystal X-ray

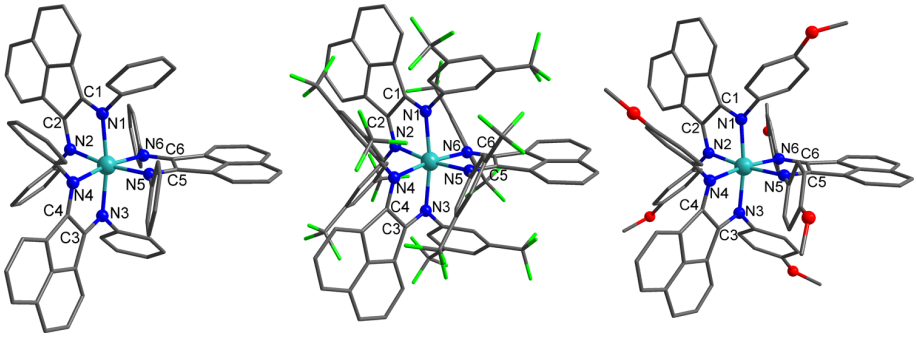

Figure 2. Molecular structures of neutral complexes **1** (100 K) (left), **2** (100 K) (middle), and **3** (120 K) (right) as determined via single-crystal X-ray diffraction with relevant atoms labeled. Hydrogen atoms and solvent molecules have been omitted for clarity. Color code: C (dark gray), N (blue), O (red), Co (light blue), F (green).

Table 1. Selected Interatomic Distances (Å), Distortion Parameters, and BVS Values for $1^{2+}(PF_6)_2$·2.5DCE·1.5*i*Pr$_2$O (Molecules A and B), $1^{+}(PF_6)$·2Et$_2$O·0.6MeCN, 1·2.5THF·pentane, 2·tol, 3, and $3^{2+}(PF_6)_2$·DCE

	$1^{2+}(PF_6)_2$ A	$1^{2+}(PF_6)_2$ B	$1^{+}(PF_6)$	1	2	3	$3^{2+}(PF_6)_2$
temperature (K)	100	100	100	100	100	120	100
			Interatomic Distances				
Co−N_1	2.127(2)	2.152(2)	2.112(2)	2.142(4)	2.114(2)	2.182(4)	2.120(3)
Co−N_2	2.154(2)	2.163(2)	2.127(2)	2.116(4)	2.135(2)	2.114(5)	2.141(3)
Co−N_3	2.133(2)	2.156(2)	2.137(2)	2.142(4)	2.114(2)	2.182(4)	2.123(3)
Co−N_4	2.123(2)	2.128(2)	2.152(2)	2.116(4)	2.135(2)	2.114(5)	2.120(3)
Co−N_5	2.159(2)	2.133(2)	2.104(2)	2.096(4)	2.131(2)	2.106(5)	2.142(3)
Co−N_6	2.150(2)	2.124(2)	2.123(2)	2.096(4)	2.131(2)	2.106(5)	2.135(3)
Co−N_{avg}	2.141(2)	2.143(2)	2.126(2)	2.118(4)	2.126(2)	2.134(5)	2.131(3)
C_1−N_1	1.288(3)	1.280(3)	1.296(3)	1.299(6)	1.302(3)	1.300(6)	1.286(5)
C_2−N_2	1.283(3)	1.275(3)	1.297(3)	1.305(5)	1.303(3)	1.318(7)	1.298(5)
C_3−N_3	1.283(3)	1.282(3)	1.290(3)	1.299(6)	1.302(3)	1.300(6)	1.282(5)
C_4−N_4	1.276(3)	1.278(3)	1.286(3)	1.305(5)	1.303(3)	1.318(7)	1.286(5)
C_5−N_5	1.278(4)	1.283(3)	1.297(2)	1.284(5)	1.330(3)	1.279(7)	1.288(5)
C_6−N_6	1.277(4)	1.273(3)	1.303(3)	1.284(5)	1.330(3)	1.279(7)	1.290(5)
C_1−C_2	1.522(3)	1.509(3)	1.483(3)	1.460(7)	1.481(3)	1.449(8)	1.504(5)
C_3−C_4	1.508(4)	1.517(3)	1.493(2)	1.460(7)	1.481(3)	1.449(8)	1.511(5)
C_5−C_6	1.512(4)	1.507(4)	1.479(3)	1.474(9)	1.440(4)	1.50(1)	1.508(5)
Co···Co[a]	12.133(1)	12.133(1)	16.897(1)	10.914(2)	10.807(2)	10.826(5)	
			Distortion and Oxidation State Parameters				
SHAPE (O_h)[b]	1.088	1.116	1.277	1.180	1.119	1.216	0.987
$\sum$/deg[c]	75.9	76.8	76.9	75.3	74.8	74.9	70.3
Θ/deg[c]	233.9	237.5	242.1	239.9	242.0	237.2	229.2
BVS[d]	1.93	1.88	2.00	2.08	2.00	1.97	1.98

[a]Closest intermolecular distance. [b]SHAPE index for octahedral geometry in SHAPE 2.1.[66] A value of 0 represents a perfect octahedron. [c]$\sum$ = sum of the deviation of the 12 N−Co−N angles from 90°. Θ = sum of the deviation of 24 unique torsional angles between the N atoms on opposite triangular faces of the octahedron from 60°, providing the degree of trigonal distortion from an octahedron to trigonal prism. These were calculated using OctaDist—a program for determining the structural distortion of the octahedral complexes. For a perfect octahedron, $\sum$ and Θ are zero.[65] [d]Value close to 2 indicates Co^{II} and 3 indicates Co^{III}.[64,70,71]

diffraction (Tables S6 and S7) to aid in determining the electronic state adopted by each complex in the solid state. Data were collected at 100 K for compounds $1^{2+}(PF_6)_2$, $1^{+}(PF_6)$, **1**, **2**, and $3^{2+}(PF_6)_2$, and at 120 K for **3**. As the collection temperature will influence the electromeric state of a compound if it displays thermal VT or SCO, each structure was collected in the same low-temperature range (100−120 K) to access the ground state. Multiple attempts were made to collect data for the poorly diffracting crystals of **1** and **3** using synchrotron radiation (detailed in the Supporting Information),[62,63] and as such, the *R*-values are higher.

The presence of solvent in the crystal structures is consistent with the compositions $1^{2+}(PF_6)_2$·2.5DCE·1.5*i*Pr$_2$O, $1^{+}(PF_6)$·2Et$_2$O·0.6MeCN, **1**·2.5THF·pentane, **2**·tol, **3**, and $3^{2+}(PF_6)_2$·DCE, as detailed in the Supporting Information. Compound $1^{2+}(PF_6)_2$·2.5DCE·1.5*i*Pr$_2$O crystallizes with two independent cobalt complexes in the structure, which are labeled 1^{2+}**A** and 1^{2+}**B** in the discussion below. The formulas in the crystal structure differ from those in the bulk samples, which were analyzed as $1^{2+}(PF_6)_2$·0.5DCE·0.5*i*Pr$_2$O, **1**·0.8EtOH, **2**, **3**·EtOH, $3^{2+}(PF_6)_2$·DCE. For complexes $1^{2+}(PF_6)_2$, **2**, and $3^{2+}(PF_6)_2$, this arises from partial desolvation upon collection of the bulk sample, and for **1** and **3**, the different methods by which the single-crystal and bulk samples were obtained. Powder X-ray diffraction (PXRD) confirmed the phase purity of the bulk samples and matched with the diffraction pattern

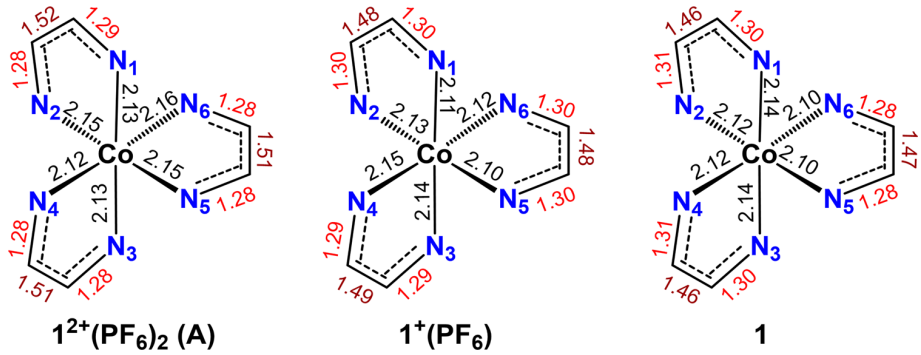

Figure 3. Comparison of bond lengths observed for $\mathbf{1}^{2+}(\mathbf{PF_6})_2$ (**A**), $\mathbf{1}^{+}(\mathbf{PF_6})$, and **1** at 100 K used to assign oxidation states.

calculated from the single-crystal X-ray structural analysis (Figures S10−S12). Despite the inability to reliably obtain a pure bulk of $\mathbf{1}^{+}(\mathbf{PF_6})$, we have included the single-crystal data for the purposes of assisting with bond length analysis.

In the solid-state structures, all of the metal complexes possess approximate D_3 point symmetry and share a Co(Ar-BIAN)$_3$ motif, with the cobalt center coordinated by three bidentate Ar-BIAN ligands, giving a distorted octahedral coordination geometry (Figures 2 and S13−S15). For the neutral compounds (**1**, **2**, and **3**), the asymmetric unit comprises half a molecule of [Co(Ar-BIAN)$_3$], in contrast to compounds $\mathbf{1}^{2+}(\mathbf{PF_6})_2$, $\mathbf{1}^{+}(\mathbf{PF_6})$, and $\mathbf{3}^{2+}(\mathbf{PF_6})_2$, which contain a full molecule with three crystallographically inequivalent Ar-BIAN ligands. The oxidation and spin state of the cobalt center can be determined by the Co−N bond lengths, bond valence sum (BVS) parameters (Table S8),[64] octahedral distortion parameters ($\sum$, Θ),[65] and the octahedral SHAPE index (Table 1).[66] In general, Co−N bond lengths and octahedral distortions increase following the trend LS-Co^{III} < LS-Co^{II} < HS-Co^{II}. The oxidation state of the Ar-BIAN ligands can be assigned via analysis of the α-diimine C−N and C−C bonds.[40,45,61,67−69] The monoanionic $L^{\bullet-}$ state has longer C−N and shorter C−C bonds compared to the neutral L^0 form as a result of populating formally π^* orbitals.

Analysis of the average Co−N bond lengths (Co−N$_{avg}$) and octahedral distortion parameters for $\mathbf{1}^{2+}\mathbf{A}$ and $\mathbf{1}^{2+}\mathbf{B}$ in $\mathbf{1}^{2+}(\mathbf{PF_6})_2$·2.5DCE·1.5*i*Pr$_2$O, $\mathbf{1}^{+}(\mathbf{PF_6})$·2Et$_2$O·0.6MeCN, **1**·2.5THF·pentane, **2**·tol, **3**, and $\mathbf{3}^{2+}(\mathbf{PF_6})_2$·DCE (Table 1) indicates the oxidation and spin state adopted by the cobalt center in each complex in the solid state. The Co−N$_{avg}$ bond lengths and lack of Jahn−Teller distortions in $\mathbf{1}^{2+}(\mathbf{PF_6})_2$ and $\mathbf{3}^{2+}(\mathbf{PF_6})_2$ at 100 K are consistent with HS-Co^{II} and are in good agreement with the DFT-optimized geometry values for the HS-Co^{II}-$(L^0)_3$ state, as opposed to LS-Co^{II}-$(L^0)_3$ or LS-Co^{III}-$(L^{\bullet-})(L^0)_2$ (Tables S1 and S3). Likewise for $\mathbf{1}^{+}(\mathbf{PF_6})$, the Co−N$_{avg}$ bond lengths and absence of Jahn−Teller distortions are also consistent with HS-Co^{II}, with bond lengths in good agreement with the DFT calculated lengths for the HS-Co^{II}-$(L^{\bullet-})(L^0)_2$ state (Table S1). Thus, crystallographic data at 100 K indicate a HS-Co^{II}-$(L^0)_3$ electromeric state for $\mathbf{1}^{2+}(\mathbf{PF_6})_2$ and $\mathbf{3}^{2+}(\mathbf{PF_6})_2$, and a HS-Co^{II}-$(L^{\bullet-})(L^0)_2$ state for $\mathbf{1}^{+}(\mathbf{PF_6})$.

The experimental Co−N$_{avg}$ bond lengths, BVS, and distortion parameters for compounds **1** and **3**, collected at 100 and 120 K, respectively, are consistent with HS-Co^{II} (Tables S2 and S3). The experimental Co−N$_{avg}$ bond lengths for compound **2** at 100 K are intermediate between the DFT-optimized geometries for the HS-Co^{II}-$(L^{\bullet-})_2(L^0)$ and LS-Co^{III}-$(L^{\bullet-})_3$ states (Table S2). However, in conjunction with BVS analysis and distortion parameters, a HS-Co^{II} center is still suggested. In previous work, compound **2** was assigned the electronic state [Co^{I}(3,5-CF$_3$-Ph-BIAN$^{\bullet-}$)(3,5-CF$_3$-Ph-BIAN^0)$_2$] based on structural analysis.[61] However, attempts to locate the [Co^{I}(3,5-CF$_3$BIAN$^{\bullet-}$)(3,5-CF$_3$-Ph-BIAN^0)$_2$] state using DFT were unsuccessful, suggesting that Co^{I} is too high in energy.

The three neutral compounds **1**, **2**, and **3** are also assigned as having a HS-Co^{II} center based on bond length, BVS, and distortion parameter analysis. However, they all show some suggestion of Jahn−Teller distortion in the experimental values, typical of LS-Co^{II}.[26,27,71] This is most obvious for **3**, while more subtle for **1** and **2**. It is possible that the slightly higher (120 K) collection temperature for **3** compared to **1** and **2** (100 K) is the reason for the more obvious elongation. In all cases, the distortion is not to the extent indicated by the DFT-optimized geometry of the LS-Co^{II}-$(L^{\bullet-})_2(L^0)$ state (Table S9). This could be due to: (1) disorder (either static or dynamic) of the Jahn−Teller distortion as previously observed for LS-Co^{II}; or (2) a mixture of LS and HS-Co^{II} at the measured temperatures.[28,71] For all three compounds, the experimental values are closer to the geometry-optimized HS-Co^{II}-$(L^{\bullet-})_2(L^0)$ geometry than LS-Co^{II}-$(L^{\bullet-})_2(L^0)$, suggesting a mixture of spin states (Table S9). To estimate the fraction of LS-Co^{II} present, we compared the difference between the Co−N$_{axial}$ and Co−N$_{equatorial}$ (averaged) lengths for the geometry-optimized structure versus the experimentally obtained bond lengths (details in the SI). This gave an approximate LS-Co^{II} percentage of 16% for **1**, 8% for **2**, and 33% for **3**. Although only an approximation, especially considering the higher *R*-values for **1** and **3**, the analysis of the experimental data for **1**, **2**, and **3** suggests divalent cobalt, with dominant HS-Co^{II}, ruling out the possibility of LS-Co^{III} at the measured temperature. Overall compounds **1**, **2**, and **3** can be assigned as predominantly the HS-Co^{II}-$(L^{\bullet-})_2(L^0)$ electromer in the solid state at 100 or 120 K.

Consideration of the bond lengths and oxidation states of the Ar-BIAN ligands provides support for the assignment of the solid-state electronic configurations for $\mathbf{1}^{2+}(\mathbf{PF_6})_2$ and $\mathbf{3}^{2+}(\mathbf{PF_6})_2$ as HS-Co^{II}-$(L^0)_3$, for $\mathbf{1}^{+}(\mathbf{PF_6})$ as HS-Co^{II}-$(L^{\bullet-})$-$(L^0)_2$, and for **1**, **2**, and **3** as HS-Co^{II}-$(L^{\bullet-})_2(L^0)$ at 100 or 120 K. The α-diimine C−N and C−C bond distances for each Ar-BIAN in $\mathbf{1}^{2+}\mathbf{A}$ and $\mathbf{1}^{2+}\mathbf{B}$, and $\mathbf{3}^{2+}(\mathbf{PF_6})_2$ are consistent with neutral Ar-BIAN^0 oxidation state,[45,48] confirming the HS-Co^{II}-$(L^0)_3$ charge distribution at 100 K in the solid state. The π-acceptor capacity of neutral Ph-BIAN and 4-MeO-Ph-BIAN is illustrated by the observed shortening of the C−C bond and elongation of the C−N bonds experimentally upon coordina-

tion compared to uncoordinated Ph-BIAN (C−N bond distance 1.275 Å, C−C bond distance 1.526 Å) and 4-MeO-Ph-BIAN (C−N bond distance 1.277 Å, C−C bond distance 1.527 Å).[45,72]

On comparing the α-diimine bond distances of the redox series of compounds $\mathbf{1}^{2+}(\mathbf{PF_6})_2$, $\mathbf{1}^{+}(\mathbf{PF_6})$, **1** (Figure 3) at 100 K, an elongation of the C−N bonds and a contraction of the C−C bond is observed with increased equivalents of Ph-BIAN$^{\bullet-}$. In compound $\mathbf{1}^{+}(\mathbf{PF_6})$, the C−N and C−C bond lengths lie between the values expected for Ph-BIAN^0 and Ph-BIAN$^{\bullet-}$,[40,45,61,67] and arise from the presence of a single L$^{\bullet-}$ and two L^0 ligands either crystallographic disordered or electronically delocalized. This supports the electromeric state adopted by $\mathbf{1}^{+}(\mathbf{PF_6})$ as HS-Co^{II}-(L$^{\bullet-}$)(L^0)$_2$ in the solid state at 100 K. The C−N and C−C bonds of **1** are further elongated and contracted, respectively, while still lying between the values expected for Ph-BIAN^0 and Ph-BIAN$^{\bullet-}$, consistent with the mixed-valent HS-Co^{II}-(L$^{\bullet-}$)$_2$(L^0) state at 100 K in the solid state. The same observation is made for **2** at 100 K (Figure S16). For **3**, shorter experimentally observed C−C and C−N bonds compared to $\mathbf{3}^{2+}(\mathbf{PF_6})_2$ that are still too long and short for pure 4-MeO-Ph-BIAN$^{\bullet-}$ indicate two L$^{\bullet-}$ and one L^0 ligands, confirming HS-Co^{II}-(L$^{\bullet-}$)$_2$(L^0) state at 120 K (Figure S16). Overall, structural analysis thus confirms that in the solid state at 100 K (**3** at 120 K), the electromeric state of $\mathbf{1}^{2+}(\mathbf{PF_6})_2$ and $\mathbf{3}^{2+}(\mathbf{PF_6})_2$ is HS-Co^{II}-(L^0)$_3$, $\mathbf{1}^{+}(\mathbf{PF_6})$ is HS-Co^{II}-(L$^{\bullet-}$)-(L^0)$_2$, and **1**, **2**, and **3** is HS-Co^{II}-(L$^{\bullet-}$)$_2$(L^0). Compound **3**, predicted to have an LS-Co^{III}-(L$^{\bullet-}$)$_3$ ground state by DFT, adopts an HS-Co^{II}-(L$^{\bullet-}$)$_2$(L^0) ground state in the solid sample.

Infrared Spectroscopy. Infrared (IR) spectra of $\mathbf{1}^{2+}(\mathbf{PF_6})_2$·0.5DCE·0.5*i*Pr$_2$O, **1**·0.8EtOH, **2**, **3**·EtOH, and $\mathbf{3}^{2+}(\mathbf{PF_6})_2$·DCE were acquired in the solid state (ATR; 4000−400 cm^{-1}; Figures S17−S19). All compounds share vibrational patterns associated with the neutral L^0 ligand in the range 1670−1580 cm^{-1}, with the presence of ligands in different redox states in the neutral species accounting for the more complex spectra than their dicationic counterparts.[48,73] These observations are consistent with structural analysis that $\mathbf{1}^{2+}(\mathbf{PF_6})_2$·0.5DCE·0.5*i*Pr$_2$O and $\mathbf{3}^{2+}(\mathbf{PF_6})_2$·DCE exist as HS-Co^{II}-(L^0)$_3$ at 100 K with no L$^{\bullet-}$ present, and structural analysis of **1**·0.8EtOH, **2**, and **3**·EtOH at 100 or 120 K that indicated a dominant HS-Co^{II}-(L$^{\bullet-}$)$_2$(L^0) state in the solid state, which would give rise to both Ar-BIAN^0 and Ar-BIAN$^{\bullet-}$. For the neutral compounds, the ν(C═N) bands shift toward higher energies in the order **3** < **1** < **2** following the inductive effects of the ligand substituent. To improve the resolution in the region of interest for C−N stretches of α-diimine (1800−1550 cm^{-1}), solution-state (CH_2Cl_2) infrared spectra were recorded (Figure S20). Good agreement in the region of interest is observed when comparing solid- and solution-state measurements for all compounds.

Magnetic Measurements. Variable-temperature magnetic susceptibility measurements were conducted for $\mathbf{1}^{2+}(\mathbf{PF_6})_2$·0.5DCE·0.5*i*Pr$_2$O, $\mathbf{3}^{2+}(\mathbf{PF_6})_2$·0.6DCE, **1**·0.8EtOH, **2**, and **3**·EtOH (Figure 4) between 1.85 and 300 K to further probe the electronic state adopted by each compound in the solid state and the variation with temperature. Variable-field magnetization measurements are presented in Figures S21 and S22. At 300 K, the thermal product of the molar magnetic susceptibility ($\chi_M T$) values for both dicationic compounds $\mathbf{1}^{2+}(\mathbf{PF_6})_2$·0.5DCE·0.5iPr$_2$O and $\mathbf{3}^{2+}(\mathbf{PF_6})_2$·0.6DCE of 3.0 and 2.7 cm^3 K mol^{-1}, respectively, are consistent with an HS-Co^{II}-(L^0)$_3$ charge distribution. This is in agreement with the

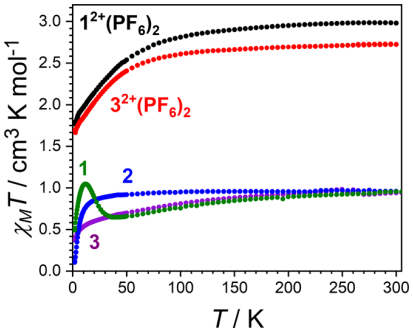

Figure 4. Temperature dependence of the χ_MT products for $\mathbf{1}^{2+}(\mathbf{PF_6})_2$·0.5DCE·0.5*i*Pr$_2$O (black), $\mathbf{3}^{2+}(\mathbf{PF_6})_2$·DCE (red), **1**·0.8EtOH (green), **2** (blue), and **3**·EtOH (purple) in the solid state at 0.1 T (χ_M, magnetic susceptibility, is defined as M/H per mole of complex; M and H are the magnetization and applied magnetic field, respectively).

structural analysis at 100 K. The $\chi_M T$ values are much higher than the spin-only value for $S = 3/2$ with $g = 2$, indicating spin−orbit coupling contributions to the magnetic susceptibility, common for HS-Co^{II} in a distorted ligand field.[59] The $\chi_M T$ value remains essentially constant upon cooling to 100 K, after which it decreases more rapidly to reach 1.8 and 1.7 cm^3 K mol^{-1} at 1.85 K for $\mathbf{1}^{2+}(\mathbf{PF_6})_2$·0.5DCE·0.5iPr$_2$O and $\mathbf{3}^{2+}(\mathbf{PF_6})_2$·0.6DCE, respectively, due to depopulation of the HS-Co^{II} spin−orbit coupled states. The observed behavior discounts thermally induced VT to the LS-Co^{III}-(L$^{\bullet-}$)(L^0)$_2$ state for both compounds.

At 300 K, $\chi_M T$ values for the neutral compounds **1**·0.8EtOH, **2**, and **3**·EtOH are all approximately 0.95 cm^3 K mol^{-1}, indicating a similar charge distribution (Figure 4). For **1**·0.8EtOH and **3**·EtOH, the $\chi_M T$ product decreases gradually below 200 K, while **2** remains approximately constant until 50 K. Below 50 K, the $\chi_M T$ response diverges for **1**·0.8EtOH compared to **2** and **3**·EtOH. For **1**·0.8EtOH, an increase is observed to reach a maximum of 1.1 cm^3 K mol^{-1} at 12 K, before rapidly decreasing to 0.49 cm^3 K mol^{-1} at 1.85 K. For **2** and **3**·EtOH, the $\chi_M T$ response below 50 K rapidly decreases to reach values of 0.10 and 0.37 cm^3 K mol^{-1}, respectively, at 1.85 K. The low-temperature feature exhibited by **1**·0.8EtOH is reminiscent of the onset of intermolecular interactions, which are perhaps mitigated in the case of **2** and **3**·EtOH due to differences in the coordinated ligands and the crystal lattice.

The room temperature $\chi_M T$ values for the neutral compounds **1**·0.8EtOH, **2**, and **3**·EtOH are much lower than expected for the HS-Co^{II}-(L$^{\bullet-}$)$_2$(L^0) state suggested by structural analysis and IR, with negligible, or weak, magnetic exchange interactions. For example, the exchange in two HS-Co^{II}-semiquinonate complexes was determined to be weakly antiferromagnetic, with room-temperature $\chi_M T$ values of 3.3 and 3.6 cm^3 K mol^{-1}, consistent with uncoupled HS-Co^{II} and semiquinonate ligand.[74] Assignment of the electronic state of the three neutral compounds based on the magnetic behavior is much more complex in comparison with the dicationic equivalents, with competing strong Co···L$^{\bullet-}$ and L$^{\bullet-}$···L$^{\bullet-}$ exchange interactions expected from the DFT calculations (Table S5) for all electronic states, and a mix of the HS-Co^{II} and LS-Co^{II} charge distributions indicated by the structural analysis. Despite the experimentally observed $\chi_M T$ values being close to the theoretical value of 1.125 cm^3 K mol^{-1} expected for both the LS-Co^{III}-(L$^{\bullet-}$)$_3$ (Scheme 3) and LS-Co^{II}-

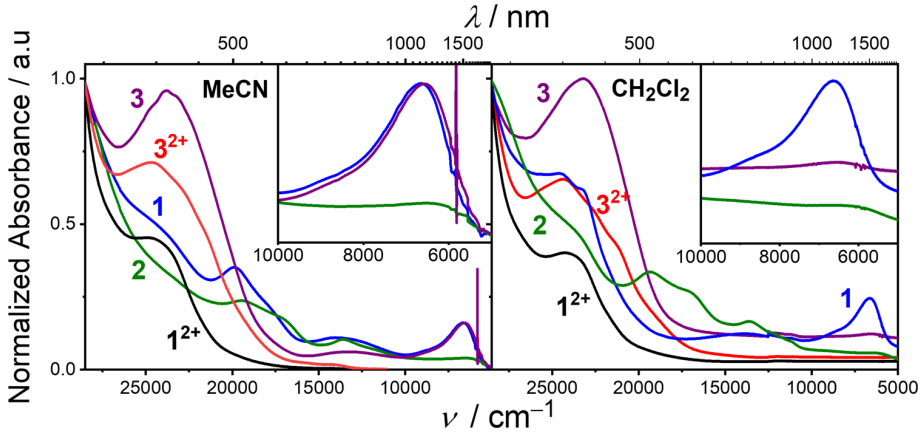

Figure 5. UV−vis−NIR absorption spectra for MeCN solutions (left) and CH_2Cl_2 (right) for $\mathbf{1}^{2+}$ (black), $\mathbf{3}^{2+}$ (red), **1** (blue), **2** (green), and **3** (purple) at room temperature, with insets emphasizing the NIR region for **1**, **2**, and **3**.

$(L^{\bullet-})_2(L^0)$ states, these electromers are discounted based on structural analysis and IR, with support from DFT. The behavior observed for **1**·0.8EtOH, **2**, and **3**·EtOH therefore arise from an HS-Co^{II}-$(L^{\bullet-})_2(L^0)$ state with substantial antiferromagnetic coupling between the HS-Co^{II} center and $L^{\bullet-}$ (calculated as −143 cm^{-1} for **1**, −76 cm^{-1} for **2**, −498 cm^{-1} for **3**) and between the two $L^{\bullet-}$ ligands (calculated as −128 cm^{-1} for **1**, −401 cm^{-1} for **2**, −30 cm^{-1} for **3**) (Scheme 3) as suggested by DFT studies. These antiferromagnetic exchange interactions dominate, even at room temperature, resulting in the observed low $\chi_M T$ values.

Previously investigated complexes with more than one radical ligand coordinated to HS-Co^{II} have also exhibited lower than expected $\chi_M T$ responses, and although attempts have been made to justify this, an exact understanding remains elusive.[33,75−77] Furthermore, related 3*d* metal and lanthanoid complexes coordinated to multiple Ar-BIAN$^{\bullet-}$ ligands display complex magnetic behavior.[36,38,69,78] These compounds exhibit strong antiferromagnetic metal···$L^{\bullet-}$, and $L^{\bullet-}$···$L^{\bullet-}$ exchange, with the competition between both modes of exchange and the trigonal symmetry of the system resulting in spin frustration.[79] In the 3*d* metal cases, the spin frustration was reported to give rise to multiple low-lying excited states, quenching the anisotropy of the metal, resulting in temperature-independent paramagnetism.[38,80,81]

In complex spin systems like those evident in adopted **1**, **2**, and **3**, the behavior is undoubtedly challenging to model, and a conventional spin-only Hamiltonian is not appropriate for HS-CoII. Certainly, there is more to be understood about magnetic exchange interactions in such compounds, but this falls outside of the scope of this study. One aspect that is clear is that for all measured compounds, $\chi_M T$ remains relatively constant from 50 to 300 K, suggesting that neither a VT nor SCO interconversion occurs in the solid state. Rather, the HS-Co^{II}-L^0 containing electromer (HS-Co^{II}-$(L^0)_3$ for $\mathbf{1}^{2+}(\mathbf{PF_6})_2$ and $\mathbf{3}^{2+}(\mathbf{PF_6})_2$, and HS-$Co^{II}$-$(L^{\bullet-})_2(L^0)$ for **1**, **2**, and **3**) is the ground state in the solid state. Although the possibility of VT is suggested for **3** by gas-phase DFT, the solid-state structural and magnetic data agree that the necessary LS-Co^{III}-$(L^{\bullet-})_3$ ground state is not observed.

Electronic Spectroscopy. In the solid state, compounds $\mathbf{1}^{2+}(\mathbf{PF_6})_2$, $\mathbf{3}^{2+}(\mathbf{PF_6})_2$, **1**, **2**, and **3** all exist in the HS-Co^{II}-L^0 containing electronic state at all measured temperatures. However, it is possible that a compound can exhibit a different electronic state in solution compared to the solid state,[33,46] which may be solvent-dependent.[82] Electronic absorption spectra (Figures 5 and S23−S27, Table S10) were recorded for $\mathbf{1}^{2+}(\mathbf{PF_6})_2$, **1**, **2**, **3**, and $\mathbf{3}^{2+}(\mathbf{PF_6})_2$ at room temperature in various solvents with a range of dielectric constants: MeCN (κ = 37.5), CH_2Cl_2 (κ = 8.93), tetrahydrofuran (THF) (κ = 7.58), and toluene (κ = 2.38) at room temperature. In MeCN and CH_2Cl_2, the visible region of the spectra of $\mathbf{1}^{2+}(\mathbf{PF_6})_2$ and $\mathbf{3}^{2+}(\mathbf{PF_6})_2$ is dominated by absorptions at approximately 25000 cm^{-1} arising from intraligand processes associated with the L^0 form of the Ar-BIAN ligand (Figures 5, S23, and S24).[48,83] The lack of features associated with Ar-BIAN$^{\bullet-}$ confirms a HS-Co^{II}-$(L^0)_3$ state in solution at room temperature for $\mathbf{1}^{2+}(\mathbf{PF_6})_2$ and $\mathbf{3}^{2+}(\mathbf{PF_6})_2$, as observed in the solid state. Compound $\mathbf{1}^{2+}(\mathbf{PF_6})_2$ also features a very weak broad band centered at 10160 cm^{-1} in the near infrared (NIR) region, assigned as a $^4T_{1g} \rightarrow {}^4T_{2g}$ d−d transition; the analogous transition was difficult to discern from the baseline in the case of $\mathbf{3}^{2+}(\mathbf{PF_6})_2$.

For **1**, **2**, and **3**, multiple broad absorption features are observed across the visible region in the range of solvents (MeCN, CH_2Cl_2, THF, toluene). Anecdotally, an octahedral HS-Co^{II} (d^7) ion displays more spin-allowed d−d transitions than LS-Co^{III} (d^6), which is consistent with the broad range of low-intensity, low-energy absorption features of **1**, **2**, and **3**. The dominant high-energy features arise from a combination of Ar-BIAN^0 intraligand transitionsand Ar-BIAN$^{\bullet-}$ intraligand transitions (Figures 5 and S25−S27).[48,83] The Ar-BIAN$^{\bullet-}$ intraligand transitions decrease in energy from **3** (23,810 cm^{-1}) to **1** (19,880 cm^{-1}) and **2** (19,493 cm^{-1}), corresponding to the shift from electron-donating to electron-withdrawing groups on the Ar-BIAN ligand. At lower energies (13,350−14,250 cm^{-1}), ligand-to-metal charge transfer (LMCT) features are also observed for all three neutral compounds (Figure 5). The assignment of features confirms that in solution at room temperature, **1**, **2**, and **3** are present as HS-Co^{II}-$(L^{\bullet-})_2(L^0)$, mirroring the solid state.

In MeCN, **1**, **2**, and **3** all feature a NIR band, assigned to a ligand-to-ligand intervalence charge transfer (IVCT) process involving the formally $L^{\bullet-}$ and L^0 ligand redox states.[36,38] This discounts a pure LS-Co^{III}-$(L^{\bullet-})_3$ state for the three compounds, further confirming the HS-Co^{II}-$(L^{\bullet-})_2(L^0)$ electronic state in solution at room temperature. The degree of electronic coupling between the Ar-BIAN ligands in **1**, **2**, and **3** can be described by the Robin and Day classification

system (see the Supporting Information),[84] and the electronic coupling parameter (H_{AB}) extracted from the energy and shape of the IVCT band in the framework of Marcus–Hush theory.[85]

Complex **1** in MeCN features an absorption envelope in the NIR region with an apparent maximum at 6645 cm^{-1}, which was deconvoluted by two Gaussian functions (Figure S28, Table S11) centered at ν_{max} = 6640(6) cm^{-1} with half-height width $\Delta\nu_{1/2}$ = 1441(3) cm^{-1} and at ν_{max} = 8400(90) cm^{-1} with $\Delta\nu_{1/2}$ = 3400(300) cm^{-1}. Similar low-energy absorption envelopes were also observed in MeCN for compounds **2** and **3** (Figures S29 and S30, Table S11) and deconvoluted in each case to two-band patterns ν_{max} = 6050(20) cm^{-1} ($\Delta\nu_{1/2}$ = 1580(90) cm^{-1}) and ν_{max} = 7700(100) cm^{-1} ($\Delta\nu_{1/2}$ = 2900(700) cm^{-1}) for **2** and ν_{max} = 6520(6) cm^{-1} ($\nu_{1/2}$ = 1470(40) cm^{-1}) and ν_{max} = 8100(100) cm^{-1} ($\Delta\nu_{1/2}$ = 3200(300) cm^{-1}) for **3**. These absorption features are solvent-dependent, reducing in intensity in CH_2Cl_2, and undetected in THF and toluene, allowing for assignment of **1**, **2**, and **3** to Class II. This indicates a localized electronic structure and solvent environment, and therefore the IVCT is linked to the reorganization energy, which in turn is linked to the energy of the optical charge transfer band. Marcus–Hush analysis of the lower-energy band shape allows estimation of H_{AB} for each of these ligand mixed-valence complexes (**1**, 721 cm^{-1}; **2**, 790 cm^{-1}; and **3**, 736 cm^{-1} (Table S11)). These values suggest similar weak electronic coupling and low levels of delocalization for **1**, **2** and **3**.[52,86]

Electrochemical and Spectroelectrochemical Studies. After establishing that in solution at room temperature compounds $\mathbf{1}^{2+}(\mathbf{PF_6})_2$ and $\mathbf{3}^{2+}(\mathbf{PF_6})_2$ adopt the HS-Co^{II}-$(L^0)_3$ state, and **1**, **2**, and **3** are in the HS-Co^{II}-$(L^{\bullet-})_2(L^0)$ state, mirroring solid-state observations, electrochemical and spectroelectrochemical studies were conducted. Cyclic voltammograms of the (air-stable) dicationic complexes $\mathbf{1}^{2+}(\mathbf{PF_6})_2$ and $\mathbf{3}^{2+}(\mathbf{PF_6})_2$ in CH_2Cl_2, with resting potentials of −0.1 and −0.2 V, respectively, reveal one oxidation process (I), assigned to the Co^{II}/Co^{III} redox couple, and four reduction processes (II, III, IV, and V) associated with the consecutive one-electron reduction of each L^0 to $L^{\bullet-}$ (II–IV) and further reduction of one $L^{\bullet-}$ to L^{2-} (V) within the measured potential range (Figure 6). In both cases, the first oxidation (I) and first reduction (II) were found to be electrochemically reversible (Figures S31 and S32). Processes III, IV, and V are completely irreversible. After reduction III, partial decomposition was detected electrochemically even while recording the voltammograms at higher scan rates, with an additional redox species with potential near process II becoming prominent as a result. As expected for the HS-Co^{II}-$(L^0)_3$ state adopted in solution at room temperature by $\mathbf{1}^{2+}(\mathbf{PF_6})_2$ and $\mathbf{3}^{2+}(\mathbf{PF_6})_2$, only ligand-based reductions (no oxidations) and cobalt-based oxidation are observed.

Static voltammograms were measured for the isolated neutral compounds **1**, **2**, and **3** under analogous conditions to the dicationic compounds $\mathbf{1}^{2+}(\mathbf{PF_6})_2$ and $\mathbf{3}^{2+}(\mathbf{PF_6})_2$ (Figures S33 and S34). The five processes identified in the neutral compounds **1** and **3** are at the same positions as their dicationic analogues, as expected for redox products. The resting potentials of −1.2, −0.9, and −1.3 V for **1**, **2**, and **3**, respectively, indicate that now process II and III are oxidations, consistent with the established HS-Co^{II}-$(L^{\bullet-})_2(L^0)$ electronic state in solution at room temperature.

Guided by the UV–vis–NIR spectra and electrochemical results, the reversible oxidation (I) and first reduction (II)

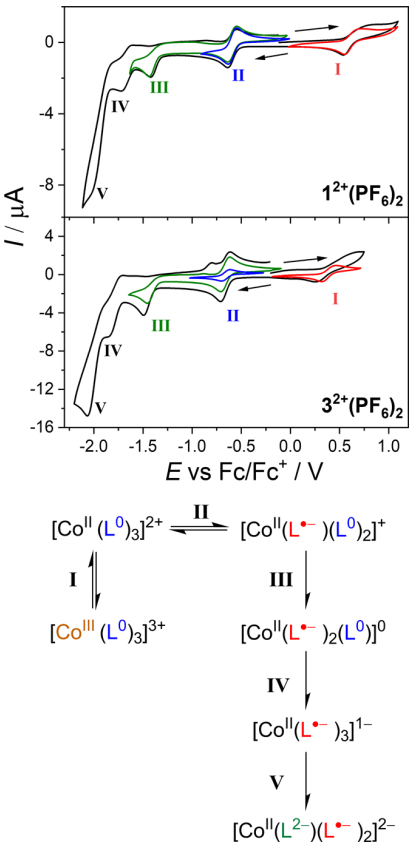

Figure 6. (Top) Cyclic voltammograms of $\mathbf{1}^{2+}(\mathbf{PF_6})_2$ and $\mathbf{3}^{2+}(\mathbf{PF_6})_2$ (0.1 M NBu_4PF_6, CH_2Cl_2) at a scan rate of 100 mV/s; the colored lines plot the voltammograms measured with a switching potential immediately past the first oxidation (red), first reduction (blue), and second reduction (green). (Bottom) Assignment of redox processes and associated species.

processes of $\mathbf{1}^{2+}(\mathbf{PF_6})_2$ and $\mathbf{3}^{2+}(\mathbf{PF_6})_2$ were studied by in situ UV–vis–NIR spectroelectrochemical methods in CH_2Cl_2 (Figure 7, Table S12). Upon oxidation of Co^{II} to Co^{III} for both compounds, all spectral features grow in intensity and shift toward lower energies. An isosbestic point is observed in the higher-energy region (ca. 33,300 cm^{-1}) and corresponds to the redshift of the high-energy π^* orbitals of the ligands, presumably through charge effects.[48] The lower-energy absorbances are all very similar between the Co^{II} species and the oxidized Co^{III} form, but with increased intensities for the Co^{III} containing species.

Upon reduction of $\mathbf{1}^{2+}(\mathbf{PF_6})_2$ and $\mathbf{3}^{2+}(\mathbf{PF_6})_2$ through process II, a clear isosbestic point is observed in the visible region (21,400 cm^{-1} for $\mathbf{1}^{2+}(\mathbf{PF_6})_2$ and 19,500 cm^{-1} for $\mathbf{3}^{2+}(\mathbf{PF_6})_2$), with features between 36,000 and 24,000 cm^{-1} (277–416 nm) that arise from the formation of the reduced form of the ligand, $L^{\bullet-}$, giving rise to the electronic state HS-Co^{II}-$(L^{\bullet-})(L^0)_2$ (analogous to $\mathbf{1}^{+}(\mathbf{PF_6})$). An additional absorbance in the visible region that appears at 13,330 cm^{-1} (750 nm) for $\mathbf{1}^{2+}(\mathbf{PF_6})_2$ and 13,100 cm^{-1} (763 nm) for $\mathbf{3}^{2+}(\mathbf{PF_6})_2$ has not been observed in the spectrum of free Ph-BIAN$^{\bullet-}$ or 4-MeO-Ph-BIAN$^{\bullet-}$,[83] discounting a $L^{\bullet-}$ intraligand transition, and suggesting a LMCT transition. The observed features resemble those present in the spectra for **1**, **2**, and **3**. Most interestingly, a peak emerges in the NIR region of the spectrum for both

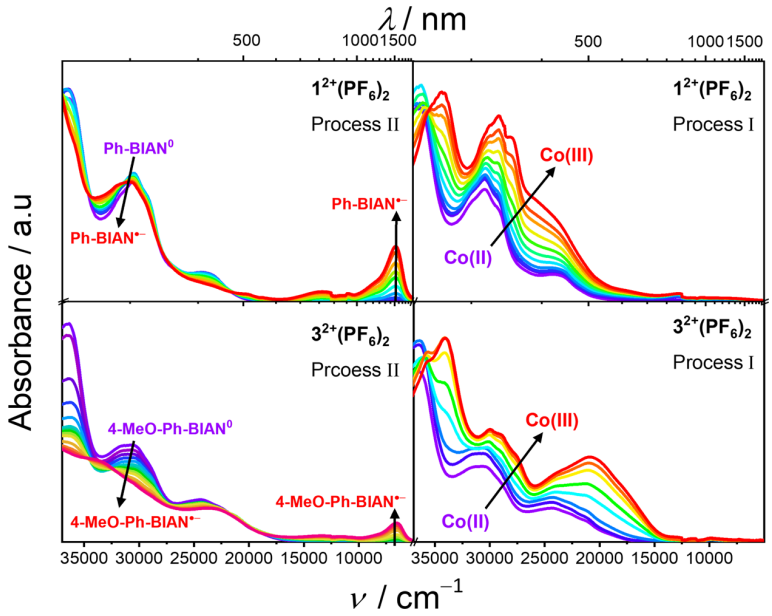

Figure 7. Spectroelectrochemical data (UV−vis−NIR) for the first reduction (left) and first oxidation (right) of complexes $\mathbf{1}^{2+}(\mathbf{PF_6})_2$ and $\mathbf{3}^{2+}(\mathbf{PF_6})_2$ (0.1 M NBu_4PF_6, CH_2Cl_2). The first reduction is $L^0 \rightarrow L^{\bullet-}$ (process II), and the first oxidation is $Co^{II} \rightarrow Co^{III}$ (process I).

compounds ($\mathbf{1}^+$, 6630 cm^{-1} (1508 nm); $\mathbf{3}^+$, 6600 cm^{-1} (1515 nm)) characteristic of the IVCT process arising from the presence of Ar-BIAN in different redox states ($L^0/L^{\bullet-}$), as observed for **1**, **2**, and **3**. Fitting the NIR peaks (Figures S35 and S36) produced upon cycling through process II to give the resulting monocationic ($\mathbf{1}^+$ and $\mathbf{3}^+$) complex gave ν_{max} = 6610(2) cm^{-1} ($\Delta\nu_{1/2}$ = 1310(10) cm^{-1}) and ν_{max} = 7930(30) cm^{-1} ($\Delta\nu_{1/2}$ = 2830(70) cm^{-1}) for $\mathbf{1}^+$, and ν_{max} = 6552(2) cm^{-1} ($\Delta\nu_{1/2}$ = 1350(10) cm^{-1}) and ν_{max} = 79,730(50) cm^{-1} ($\Delta\nu_{1/2}$ = 3000(100) cm^{-1}) for $\mathbf{3}^+$. The H_{AB} values for the lower-energy bands at 655 and 675 cm^{-1} for $\mathbf{1}^+$ and $\mathbf{3}^+$, respectively, indicate that like **1**, **2**, and **3**, a MV Class II is likely for both $\mathbf{1}^+$ and $\mathbf{3}^+$.

Variable-Temperature Electronic Spectroscopy. The electronic state of **1**, **2**, and **3** in solution at room temperature has been established as HS-Co^{II}-$(L^{\bullet-})_2(L^0)$ via electronic absorption spectroscopy, electrochemistry, and spectroelectrochemistry. This mirrors the solid-state observations. However, DFT calculations (vide supra) for **3** point to an LS-Co^{III}-$(L^{\bullet-})_3$ ground state and the possibility of thermally induced VT (Scheme 2). No evidence of VT was observed in the solid state. However, as mentioned, VT can still occur in solution even if not observed in the solid.[33] To investigate the possibility in solution, lower-temperature absorption spectra were measured for both **1** and **3** upon cooling down to our instrumental limit of 243 K in both CH_2Cl_2 and MeCN (Figures 8, S37, and S38).

For **3** in CH_2Cl_2, only minimal changes are evident in the visible range upon cooling, including a slight increase in the intensity of the $L^{\bullet-}$ intraligand band at 430 nm (23,200 cm^{-1}), but the IVCT peak exhibits little change, consistent with no VT (Figure S37). However, in MeCN, a more significant increase is evident in the intensity of the $L^{\bullet-}$ intraligand transition at 430 nm, with two closely spaced isosbestic points at 513 and 522 nm, indicating the onset of an equilibrium between two (or more) species (Figure 8). These isosbestic points are found at a similar energy to that observed in the

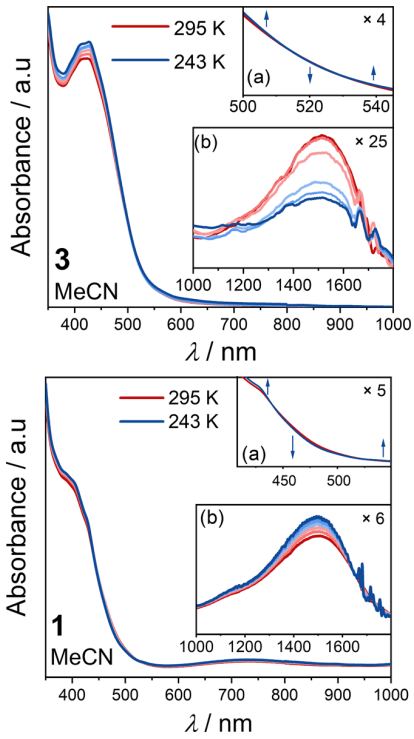

Figure 8. Variable-temperature UV−vis−NIR absorption spectra for **3** (top) and **1** (bottom) in MeCN between 243 and 295 K, with insets (a) highlighting isosbestic points and (b) the temperature dependence of the IVCT band in the NIR region.

spectroelectrochemical measurements on cycling through reduction process II. More intriguingly, on cooling, the IVCT band at ~1510 nm (6623 cm^{-1}) decreases significantly in intensity, indicating a decrease in the mixed-valence character of the ligands, suggestive of increased LS-Co^{III}-$(L^{\bullet-})_3$ population. This change is reversed upon warming to

room temperature, indicating a reversible thermal process (Figure S39). Similar changes in IVCT band intensities with temperature have been instrumental for monitoring thermally induced VT for cobalt complexes involving interconversion from two semiquinonate ligands to one semiquinonate and one catecholate ligand.[44,87−89] Therefore, the variable-temperature data suggests thermally induced VT for **3** in MeCN, involving interconversion between LS-Co^{III}-$(L^{\bullet-})_3$ at low temperature and HS-Co^{III}-$(L^{\bullet-})_2(L^0)$ at higher temperature (Scheme 3). This is consistent with DFT predictions. The observed effect of solvent on the VT transition is consistent with previous observations for cobalt-dioxolene systems, where the solvent is known to alter the relative stability of the different charge distributions and modulate the charge transfer processes.[82] Specifically, chlorinated solvents tend to stabilize the HS-Co^{II}-semiquinonate state, whereas nitrile solvents stabilize the LS-Co^{III}-catecholate tautomer.[19,43] For comparison, **1** was also measured down to 243 K in CH_2Cl_2 and MeCN. In both solvents, the intensity of the $L^{\bullet-}$ intraligand bands around 395 nm (25320 cm^{-1}) decrease very slightly with decreasing temperature, with isosbestic points around 437 and 522 nm. However, the IVCT band increases slightly in intensity upon cooling, rather than decreasing, , indicating no VT transition for this compound.

The $[Co(Ar\text{-}BIAN)_3]^{n+}$ (n = 0, 1, 2) family of homoleptic complexes incorporating an electronically diverse range of α-diimine Ar-BIAN ligands have been explored, and their electronic structures analyzed via a combination of computational, structural, magnetic, spectroscopic, and electrochemical techniques. The aim of this work at the outset was to investigate the possibility of molecular switchability in the form of thermally induced SCO or VT. Density functional theory calculations proved invaluable in guiding the choice of compounds to synthesize and investigate experimentally, with the critical DFT output being the relative energies of the electromeric forms relevant for the different types of interconversions. The DFT calculations of all members of the $[Co(Ar\text{-}BIAN)_3]^{n+}$ family complexes studied here suggested that SCO is likely unattainable for this family. This can be attributed to the inability of the Ar-BIAN/Ar-BIAN$^{\bullet-}$ ligands to provide a sufficiently strong ligand field to stabilize a LS-Co^{II} containing electromer. In contrast, the calculations suggested that a neutral $[Co(Ar\text{-}BIAN)_3]$ complex with a strongly electron-donating Ar-BIAN/Ar-BIAN$^{\bullet-}$ ligand combination might afford VT by stabilizing the LS-Co^{III}-$(L^{\bullet-})_3$ ground state and allowing interconversion to a low-lying HS-Co^{II}-$(L^{\bullet-})_2(L^0)$ state upon heating. The most promising candidate compound for VT was thus identified as $[Co(4\text{-}MeO\text{-}Ph\text{-}BIAN)_3]$.

Six members of the $[Co(Ar\text{-}BIAN)_3]^{n+}$ (n = 0, 1, 2) family with three different Ar-BIAN ligands were synthesized and characterized in the solid state and solution. Solid-state structural and magnetic data are consistent with a HS-Co^{II}-L^0 containing electronic structure for all six complexes, with no VT processes evident in the solid state. Detailed electronic absorption spectroscopy, electrochemistry, and spectroelectrochemistry studies performed on several analogues in solution at room temperature are consistent with the ground-state charge distributions observed in the solid state. However, variable-temperature electronic absorption spectra of $[Co(4\text{-}MeO\text{-}Ph\text{-}BIAN)_3]$ in MeCN show evidence of a valence tautomeric interconversion from the HS-Co^{II}-$(L^{\bullet-})_2(L^0)$ state at room temperature to LS-Co^{III}-$(L^{\bullet-})_3$ upon cooling to 243 K. Specifically, the ligand-based IVCT band in the NIR decreases significantly in intensity upon cooling, consistent with a decrease in the extent of ligand mixed-valency as HS-Co^{II}-$(L^{\bullet-})_2(L^0)$ interconverts to LS-Co^{III}-$(L^{\bullet-})_3$. Although the extent of the interconversion cannot be determined with the present data, the DFT prediction of thermally induced VT for $[Co(4\text{-}MeO\text{-}Ph\text{-}BIAN)_3]$ has been experimentally verified. This study has thus identified a new chemical family of VT complexes. Furthermore, this work has demonstrated that maximization of ligand electron donation via simultaneously maximizing the negative charge on the ligands, and incorporating electron-donating substituents, sufficiently stabilizes the LS-Co^{III}-$(L^{\bullet-})$ containing tautomer, which is key for accessing VT in this $[Co(Ar\text{-}BIAN)_3]^{n+}$ (n = 0, 1, 2) family of complexes. Although beyond the scope of this work, it is conceivable then that extending this principle by incorporating the dianionic Ar-BIAN^{2-} ligands might facilitate the alternative VT interconversion possible with these ligands: LS-Co^{III}-(L^{2-}) $\rightleftharpoons$ HS-Co^{II}-$(L^{\bullet-})$, rather than the LS-Co^{III}-$(L^{\bullet-})$ $\rightleftharpoons$ HS-Co^{II}-(L^0) observed for $[Co(4\text{-}MeO\text{-}Ph\text{-}BIAN)_3]$. Most importantly, this study clearly indicates the power of DFT-guided selection of candidate compounds for the efficient development of new functional molecules.

CCDC 2178597−2178602 contain the supplementary crystallographic data for this paper. These data can be obtained free of charge via www.ccdc.cam.ac.uk/data_request/cif, or by emailing data_request@ccdc.cam.ac.uk, or by contacting The Cambridge Crystallographic Data Centre, 12 Union Road, Cambridge CB2 1EZ, UK; fax: +44 1223 336033.

Corresponding Author

Colette Boskovic − *School of Chemistry, University of Melbourne, Parkville, Victoria 3010, Australia;* orcid.org/0000-0002-1882-2139; Email: c.boskovic@unimelb.edu.au

Authors

Moya A. Hay − *School of Chemistry, University of Melbourne, Parkville, Victoria 3010, Australia;* orcid.org/0000-0003-0667-7015

Jett T. Janetzki − *School of Chemistry, University of Melbourne, Parkville, Victoria 3010, Australia;* orcid.org/0000-0001-8646-3388

Varshini J. Kumar − *School of Molecular Sciences, University of Western Australia, Crawley, Western Australia 6009, Australia*

Robert W. Gable − *School of Chemistry, University of Melbourne, Parkville, Victoria 3010, Australia;* orcid.org/0000-0002-4626-0217

Rodolphe Clérac − *University of Bordeaux, CNRS, CRPP, UMR 5031, F-33600 Pessac, France;* orcid.org/0000-0001-5429-7418

Alyona A. Starikova − *Institute of Physical and Organic Chemistry, Southern Federal University, 344090 Rostov-on-Don, Russian Federation;* orcid.org/0000-0001-5842-0559

Paul J. Low − *School of Molecular Sciences, University of Western Australia, Crawley, Western Australia 6009, Australia;* orcid.org/0000-0003-1136-2296

Author Contributions

[⊥]M.A.H. and J.T.J. contributed equally to this paper. The manuscript was written through contributions of all authors. All authors have given approval to the final version of the manuscript.

C.B. thanks the Australian Research Council for financial support (DP190100854 and DP220100398). This research was undertaken in part using the MX1 and MX2 beamline at the Australian Synchrotron, part of ANSTO, Australia. A.A.S. thanks the Ministry of Science and Higher Education of the Russian Federation (State assignment in the field of scientific activity, project no. 0852-2020-0031). The authors are thankful to the University of Bordeaux, the Région Nouvelle Aquitaine, Quantum Matter Bordeaux (QMBx), the Centre National de la Recherche Scientifique (CNRS), and the Association Française de Magnétisme Moléculaire. They also thank Prof. Keith Murray, Dr. Wasinee Phonsri, and Maja Dunstan for preliminary magnetic measurements.

(1) Aviram, A.; Ratner, M. A. Molecular Rectifiers. *Chem. Phys. Lett.* **1974**, *29*, 277−283.
(2) Markov, I. L. Limits on Fundamental Limits to Computation. *Nature* **2014**, *512*, 147−154.
(3) Xiang, D.; Wang, X.; Jia, C.; Lee, T.; Guo, X. Molecular-Scale Electronics: From Concept to Function. *Chem. Rev.* **2016**, *116*, 4318−4440.
(4) Wasielewski, M. R.; Forbes, M. D. E.; Frank, N. L.; Kowalski, K.; Scholes, G. D.; Yuen-Zhou, J.; Baldo, M. A.; Freedman, D. E.; Goldsmith, R. H.; Goodson, T.; Kirk, M. L.; McCusker, J. K.; Ogilvie, J. P.; Shultz, D. A.; Stoll, S.; Whaley, K. B. Exploiting Chemistry and Molecular Systems for Quantum Information Science. *Nat. Rev. Chem.* **2020**, *4*, 490−504.
(5) Lefter, C.; Davesne, V.; Salmon, L.; Molnár, G.; Demont, P.; Rotaru, A.; Bousseksou, A. Charge Transport and Electrical Properties of Spin Crossover Materials: Towards Nanoelectronic and Spintronic Devices. *Magnetochemistry* **2016**, *2*, 18.
(6) Hao, G.; Cheng, R.; Dowben, P. A. The Emergence of the Local Moment Molecular Spin Transistor. *J. Phys. Condens. Matter* **2020**, *32*, No. 234002.
(7) Cornia, A.; Seneor, P. Spintronics: The Molecular Way. *Nat. Mater.* **2017**, *16*, 505−506.
(8) Yu, C. J.; Von Kugelgen, S.; Laorenza, D. W.; Freedman, D. E. A Molecular Approach to Quantum Sensing. *ACS Cent. Sci.* **2021**, *7*, 712−723.
(9) Paquette, M. M.; Plaul, D.; Kurimoto, A.; Patrick, B. O.; Frank, N. L. Opto-Spintronics: Photoisomerization-Induced Spin State Switching at 300 K in Photochrome Cobalt-Dioxolene Thin Films. *J. Am. Chem. Soc.* **2018**, *140*, 14990−15000.
(10) Senthil Kumar, K.; Ruben, M. Emerging Trends in Spin Crossover (SCO) Based Functional Materials and Devices. *Coord. Chem. Rev.* **2017**, *346*, 176−205.
(11) Urdampilleta, M.; Ayela, C.; Ducrot, P. H.; Rosario-Amorin, D.; Mondal, A.; Rouzières, M.; Dechambenoit, P.; Mathonière, C.; Mathieu, F.; Dufour, I.; Clérac, R. Molecule-Based Microelectromechanical Sensors. *Sci. Rep.* **2018**, *8*, No. 8016.
(12) Karuppannan, S. K.; Martín-Rodríguez, A.; Ruiz, E.; Harding, P.; Harding, D. J.; Yu, X.; Tadich, A.; Cowie, B.; Qi, D.; Nijhuis, C. A. Room Temperature Conductance Switching in a Molecular Iron(III) Spin Crossover Junction. *Chem. Sci.* **2021**, *12*, 2381−2388.
(13) Sato, O.; Tao, J.; Zhang, Y.-Z. Control of Magnetic Properties through External Stimuli. *Angew. Chem., Int. Ed.* **2007**, *46*, 2152−2187.
(14) Kumar, K. S.; Ruben, M. Sublimable Spin-Crossover Complexes: From Spin-State Switching to Molecular Devices. *Angew. Chem., Int. Ed.* **2021**, *60*, 7502−7521.
(15) Hay, M. A.; Boskovic, C. Lanthanoid Complexes as Molecular Materials: The Redox Approach. *Chem. - Eur. J.* **2020**, 3608−3637.
(16) Gransbury, G. K.; Boskovic, C. Valence Tautomerism in D-Block Complexes. In *Encyclopedia of Inorganic and Bioinorganic Chemistry*; Wiley, 2021; pp 1−24.
(17) Hayami, S.; Holmes, S. M.; Halcrow, M. A. Spin-State Switches in Molecular Materials Chemistry. *J. Mater. Chem. C* **2015**, *3*, 7775−7778.
(18) Halcrow, M. A. *Spin-Crossover Materials: Properties and Applications*; John Wiley & Sons Ltd., 2013.
(19) Tezgerevska, T.; Alley, K. G.; Boskovic, C. Valence Tautomerism in Metal Complexes: Stimulated and Reversible Intramolecular Electron Transfer between Metal Centers and Organic Ligands. *Coord. Chem. Rev.* **2014**, *268*, 23−40.
(20) Droghetti, A.; Sanvito, S. Electric Field Control of Valence Tautomeric Interconversion in Cobalt Dioxolene. *Phys. Rev. Lett.* **2011**, *107*, No. 047201.
(21) Li, B.; Zhao, Y. M.; Kirchon, A.; Pang, J. D.; Yang, X. Y.; Zhuang, G. L.; Zhou, H. C. Unconventional Method for Fabricating Valence Tautomeric Materials: Integrating Redox Center within a Metal-Organic Framework. *J. Am. Chem. Soc.* **2019**, *141*, 6822−6826.
(22) Vázquez-Mera, N. A.; Roscini, C.; Hernando, J.; Ruiz-Molina, D. Liquid-Filled Valence Tautomeric Microcapsules: A Solid Material with Solution-Like Behavior. *Adv. Funct. Mater.* **2015**, *25*, 4129−4134.
(23) Vázquez-Mera, N. A.; Novio, F.; Roscini, C.; Bellacanzone, C.; Guardingo, M.; Hernando, J.; Ruiz-Molina, D. Switchable Colloids, Thin-Films and Interphases Based on Metal Complexes with Non-Innocent Ligands: The Case of Valence Tautomerism and Their Applications. *J. Mater. Chem. C* **2016**, *4*, 5879−5889.
(24) Tezgerevska, T.; Rousset, E.; Gable, R. W.; Jameson, G. N. L.; Sañudo, E. C.; Starikova, A.; Boskovic, C. Valence Tautomerism and Spin Crossover in Pyridinophane−Cobalt−Dioxolene Complexes: An Experimental and Computational Study. *Dalton Trans.* **2019**, *48*, 11674−11689.
(25) Drath, O.; Boskovic, C. Switchable Cobalt Coordination Polymers: Spin Crossover and Valence Tautomerism. *Coord. Chem. Rev.* **2018**, *375*, 256−266.
(26) Goodwin, H. A. Spin Crossover in Cobalt(II) Systems. In *Spin Crossover in Transition Metal Compounds II*; Springer Berlin Heidelberg: Berlin, Heidelberg: Cambridge, 2012; Vol. *234*, pp 23−47.
(27) Krivokapic, I.; Zerara, M.; Daku, M. L.; Vargas, A.; Enachescu, C.; Ambrus, C.; Tregenna-Piggott, P.; Amstutz, N.; Krausz, E.; Hauser, A. Spin-Crossover in Cobalt(II) Imine Complexes. *Coord. Chem. Rev.* **2007**, *251*, 364−378.

(28) Kilner, C. A.; Halcrow, M. A. An Unusual Discontinuity in the Thermal Spin Transition in $[Co(terpy)_2][BF_4]_2$. *Dalton Trans.* **2010**, *39*, 9008−9012.
(29) Hayami, S.; Komatsu, Y.; Shimizu, T.; Kamihata, H.; Lee, Y. H. Spin-Crossover in Cobalt(II) Compounds Containing Terpyridine and Its Derivatives. *Coord. Chem. Rev.* **2011**, *255*, 1981−1990.
(30) Kobayashi, F.; Komatsumaru, Y.; Akiyoshi, R.; Nakamura, M.; Zhang, Y.; Lindoy, L. F.; Hayami, S. Water Molecule-Induced Reversible Magnetic Switching in a Bis-Terpyridine Cobalt(II) Complex Exhibiting Coexistence of Spin Crossover and Orbital Transition Behaviors. *Inorg. Chem.* **2020**, *59*, 16843−16852.
(31) Cowan, M. G.; Olguín, J.; Narayanaswamy, S.; Tallon, J. L.; Brooker, S. Reversible Switching of a Cobalt Complex by Thermal, Pressure, and Electrochemical Stimuli: Abrupt, Complete, Hysteretic Spin Crossover. *J. Am. Chem. Soc.* **2012**, *134*, 2892−2894.
(32) Yang, C.; Nikiforidis, G.; Park, J. Y.; Choi, J.; Luo, Y.; Zhang, L.; Wang, S. C.; Chan, Y. T.; Lim, J.; Hou, Z.; Baik, M. H.; Lee, Y.; Byon, H. R. Designing Redox-Stable Cobalt−Polypyridyl Complexes for Redox Flow Batteries: Spin-Crossover Delocalizes Excess Charge. *Adv. Energy Mater.* **2018**, *8*, No. 1702897.
(33) Fleming, C.; Chung, D.; Ponce, S.; Brook, D. J. R.; DaRos, J.; Das, R.; Ozarowski, A.; Stoian, S. A. Valence Tautomerism in a Cobalt-Verdazyl Coordination Compound. *Chem. Commun.* **2020**, *56*, 4400−4403.
(34) Bonanno, N. M.; Watts, Z.; Mauws, C.; Patrick, B. O.; Wiebe, C. R.; Shibano, Y.; Sugisaki, K.; Matsuoka, H.; Shiomi, D.; Sato, K.; Takui, T.; Lemaire, M. T. Valence Tautomerism in a $[2 \times 2]$ Co_4 Grid Complex Containing a Ditopic Arylazo Ligand. *Chem. Commun.* **2021**, *57*, 6213−6216.
(35) Wang, J.; Soo, H. S.; Garcia, F. Synthesis, Properties, and Catalysis of p-Block Complexes Supported by Bis(Arylimino)-Acenaphthene Ligands. *Commun. Chem.* **2020**, *3*, No. 113.
(36) Clark, K. M.; Bendix, J. Delocalization and Valence Tautomerism in Vanadium Tris(Iminosemiquinone) Complexes. *Angew. Chem., Int. Ed.* **2016**, *55*, 2748−2752.
(37) Fedushkin, I. L.; Maslova, O. V.; Morozov, A. G.; Dechert, S.; Demeshko, S.; Meyer, F. Genuine Redox Isomerism in a Rare-Earth-Metal Complex. *Angew. Chem., Int. Ed.* **2012**, *51*, 10584−10587.
(38) Clark, K. M.; Bendix, J.; Heyduk, A. F.; Ziller, J. W. Synthesis and Characterization of a Neutral Titanium Tris(Iminosemiquinone) Complex Featuring Redox-Active Ligands. *Inorg. Chem.* **2012**, *51*, 7457−7459.
(39) Hill, N. J.; Vargas-Baca, I.; Cowley, A. H. Recent Developments in the Coordination Chemistry of Bis(Imino)Acenaphthene (BIAN) Ligands with s- and p-Block Elements. *Dalton Trans.* **2009**, *9226*, 240−253.
(40) Fedushkin, I. L.; Skatova, A. A.; Chudakova, V. A.; Fukin, G. K. Four-Step Reduction of Dpp-Bian with Sodium Metal: Crystal Structures of the Sodium Salts of the Mono-, Di-, Tri- and Tetraanions of dpp-Bian. *Angew. Chem., Int. Ed* **2003**, *42*, 3294−3298.
(41) Gasperini, M.; Ragaini, F.; Cenini, S. Synthesis of Ar-BIAN Ligands (Ar-BIAN = Bis(Aryl)Acenaphthenequinonediimine) Having Strong Electron-Withdrawing Substituents on the Aryl Rings and Their Relative Coordination Strength toward Palladium(0) and (II) Complexes. *Organometallics* **2002**, *21*, 2950−2957.
(42) Beni, A.; Dei, A.; Laschi, S.; Rizzitano, M.; Sorace, L. Tuning the Charge Distribution and Photoswitchable Properties of Cobalt−Dioxolene Complexes by Using Molecular Techniques. *Chem. - Eur. J.* **2008**, *14*, 1804−1813.
(43) Gransbury, G. K.; Boulon, M. E.; Petrie, S.; Gable, R. W.; Mulder, R. J.; Sorace, L.; Stranger, R.; Boskovic, C. DFT Prediction and Experimental Investigation of Valence Tautomerism in Cobalt-Dioxolene Complexes. *Inorg. Chem.* **2019**, *58*, 4230−4243.
(44) Janetzki, J. T.; Zahir, F. Z. M.; Gable, R. W.; Phonsri, W.; Murray, K. S.; Goerigk, L.; Boskovic, C. A Convenient DFT-Based Strategy for Predicting Transition Temperatures of Valence Tautomeric Molecular Switches. *Inorg. Chem.* **2021**, *60*, 14475−14487.
(45) Schmitz, M.; Seibel, M.; Kelm, H.; Demeshko, S.; Meyer, F.; Krüger, H.-J. How Does a Coordinated Radical Ligand Affect the Spin Crossover Properties in an Octahedral Iron(II) Complex? *Angew. Chem., Int. Ed.* **2014**, *53*, 5988−5992.
(46) Fedushkin, I. L.; Maslova, O. V.; Baranov, E. V.; Shavyrin, A. S. Redox Isomerism in the Lanthanide Complex [(dpp-Bian)Yb(DME)-(μ-Br)]$_2$(dpp-Bian = 1,2-Bis[(2,6-diisopropylphenyl)imino]-acenaphthene). *Inorg. Chem.* **2009**, *48*, 2355−2357.
(47) Starikov, A. G.; Starikova, A. A.; Minkin, V. I. Quantum Chemical Study of the Adducts of Azomethine Cobalt Complexes with Acenaphthene-1,2-Diimines. *Russ. J. Gen. Chem.* **2017**, *87*, 98−106.
(48) Nadurata, V. L.; Hay, M. A.; Janetzki, J. T.; Gransbury, G. K.; Boskovic, C. Rich Redox-Activity and Solvatochromism in a Family of Heteroleptic Cobalt Complexes. *Dalton Trans.* **2021**, *50*, 16631−16646.
(49) Tao, J.; Perdew, J. P.; Staroverov, V. N.; Scuseria, G. E. Climbing the Density Functional Ladder: Nonempirical Meta−Generalized Gradient Approximation Designed for Molecules and Solids. *Phys. Rev. Lett.* **2003**, *91*, No. 146401.
(50) Staroverov, V. N.; Scuseria, G. E.; Tao, J.; Perdew, J. P. Comparative Assessment of a New Nonempirical Density Functional: Molecules and Hydrogen-Bonded Complexes. *J. Chem. Phys.* **2003**, *119*, 12129−12137.
(51) Frisch, M. J.; Trucks, G. W.; Schlegel, H. B.; Scuseria, G. E.; Robb, M. A.; Cheeseman, J. R.; Scalmani, G.; Barone, V.; Petersson, G. A.; Nakatsuji, H.; Li, X.; Caricato, M.; Marenich, A. V.; Bloino, J.; Janesko, B. G.; Gomperts, R.; Mennucci, B.; Hratch, D. J. et al.. *Gaussian 16*, revision C.01.
(52) Gransbury, G. K.; Livesay, B. N.; Janetzki, J. T.; Hay, M. A.; Gable, R. W.; Shores, M. P.; Starikova, A.; Boskovic, C. Understanding the Origin of One- or Two-Step Valence Tautomeric Transitions in Bis(Dioxolene)-Bridged Dinuclear Cobalt Complexes. *J. Am. Chem. Soc.* **2020**, *142*, 10692−10704.
(53) Minkin, V. I.; Starikov, A. G.; Starikova, A. A. Computational Insight into Magnetic Behavior and Properties of the Transition Metal Complexes with Redox-Active Ligands: A DFT Approach. *Pure Appl. Chem* **2018**, *90*, 811−824.
(54) Starikova, A. A.; Minkin, V. I. Adducts of Transition Metal Complexes with Redox-Active Ligands: The Structure and Spin-State-Switching Rearrangements. *Russ. Chem. Rev.* **2018**, *87*, 1049−1079.
(55) Wang, J. P.; Liu, W. T.; Yu, M.; Ji, X. Y.; Liu, J. L.; Chi, M. Z.; Starikova, A. A.; Tao, J. One-Step versus Two-Step Valence Tautomeric Transitions in Tetraoxolene-Bridged Dinuclear Cobalt Compounds. *Inorg. Chem.* **2022**, *61*, 4428−4441.
(56) Hammett, L. P. The Effect of Structure upon the Reactions of Organic Compounds. Temperature and Solvent Influences. *J. Chem. Phys.* **1936**, *4*, 613−617.
(57) Genix, P.; Jullien, H.; Le Goas, R. Estimation of Hammett Sigma Constants from Calculated Atomic Charges Using Partial Least Squares Regression. *J. Chemom.* **1996**, *10*, 631−636.
(58) Noodleman, L. Valence Bond Description of Antiferromagnetic Coupling in Transition Metal Dimers. *J. Chem. Phys.* **1981**, *74*, 5737−5743.
(59) Gransbury, G. K.; Boulon, M.-E.; Mole, R. A.; Gable, R. W.; Moubaraki, B.; Murray, K. S.; Sorace, L.; Soncini, A.; Boskovic, C. Single-Ion Anisotropy and Exchange Coupling in Cobalt(II)-Radical Complexes: Insights from Magnetic and Ab Initio Studies. *Chem. Sci.* **2019**, *10*, 8855−8871.
(60) Starikov, A. G.; Starikova, A. A.; Minkin, V. I. Quantum-Chemical Study of Spin Crossover in Cobalt Complexes with an o-Benzoquinone Ligand. *Dokl. Chem.* **2016**, *467*, 83−87.
(61) Khusniyarov, M. M.; Harms, K.; Burghaus, O.; Sundermeyer, J. Molecular and Electronic Structures of Homoleptic Nickel and Cobalt Complexes with Non-Innocent Bulky Diimine Ligands Derived from Fluorinated 1,4-Diaza-1,3-butadiene (DAD) and Bis(Arylimino)-Acenaphthene (BIAN). *Eur. J. Inorg. Chem.* **2006**, *2006*, 2985−2996.
(62) Cowieson, N. P.; Aragao, D.; Clift, M.; Ericsson, D. J.; Gee, C.; Harrop, S. J.; Mudie, N.; Panjikar, S.; Price, J. R.; Riboldi-Tunnicliffe,

A.; Williamson, R.; Caradoc-Davies, T. MX1: A Bending-Magnet Crystallography Beamline Serving Both Chemical and Macromolecular Crystallography Communities at the Australian Synchrotron. *J. Synchrotron Radiat.* **2015**, *22*, 187−190.
(63) Aragão, D.; Aishima, J.; Cherukuvada, H.; Clarken, R.; Clift, M.; Cowieson, N. P.; Ericsson, D. J.; Gee, C. L.; Macedo, S.; Mudie, N.; Panjikar, S.; Price, J. R.; Riboldi-Tunnicliffe, A.; Rostan, R.; Williamson, R.; Caradoc-Davies, T. T. MX2: A High-Flux Undulator Microfocus Beamline Serving Both the Chemical and Macromolecular Crystallography Communities at the Australian Synchrotron. *J. Synchrotron Radiat.* **2018**, *25*, 885−891.
(64) Camargo, P. H. C. The Chemical Bond in Inorganic Chemistry: The Bond Valence Model, 2nd Ed. *J. Mater. Sci.* **2017**, *52*, 9959−9962.
(65) Ketkaew, R.; Tantirungrotechai, Y.; Harding, P.; Chastanet, G.; Guionneau, P.; Marchivie, M.; Harding, D. J. OctaDist: A Tool for Calculating Distortion Parameters in Spin Crossover and Coordination Complexes. *Dalton Trans.* **2021**, *50*, 1086−1096.
(66) Llunell, M.; Casanova, D.; Cirera, J.; Alemany, P.; Alvarez, S. *SHAPE, 2.1*; Universitat de Barcelona: Barecelona, Spain, 2013.
(67) Fedushkin, I. L.; Lukoyanov, A. N.; Baranov, E. V. Lanthanum Complexes with a Diimine Ligand in Three Different Redox States. *Inorg. Chem.* **2018**, *57*, 4301−4309.
(68) Zhou, M.; Li, X.; Bu, D.; Lei, H. Synthesis, Crystal Structures and Electrochemical Properties of Co(II) and Mn(II) Complexes with Asymmetric Bulky BIAN Ligands. *Polyhedron* **2018**, *148*, 88−99.
(69) Zarkesh, R. A.; Ichimura, A. S.; Monson, T. C.; Tomson, N. C.; Anstey, M. R. Voltage Clustering in Redox-Active Ligand Complexes: Mitigating Electronic Communication through Choice of Metal Ion. *Dalton Trans.* **2016**, *45*, 9962−9969.
(70) Brown, I. D.; Altermatt, D. Bond-Valence Parameters Obtained from a Systematic Analysis of the Inorganic Crystal Structure Database. *Acta Crystallogr., Sect. B: Struct. Sci.* **1985**, *41*, 244−247.
(71) Halcrow, M. A. Jahn−Teller Distortions in Transition Metal Compounds, and Their Importance in Functional Molecular and Inorganic Materials. *Chem. Soc. Rev.* **2013**, *42*, 1784−1795.
(72) Coventry, D. N.; Batsanov, A. S.; Goeta, A. E.; Howard, J. A. K.; Marder, T. B. Synthesis and Molecular Structures of α-Diimines and Their Zinc and Palladium Dichloride Complexes. *Polyhedron* **2004**, *23*, 2789−2795.
(73) Mondal, P.; Agarwala, H.; Jana, R. D.; Plebst, S.; Grupp, A.; Ehret, F.; Mobin, S. M.; Kaim, W.; Lahiri, G. K. Sensitivity of a Strained C−C Single Bond to Charge Transfer: Redox Activity in Mononuclear and Dinuclear Ruthenium Complexes of Bis-(Arylimino)Acenaphthene (BIAN) Ligands. *Inorg. Chem.* **2014**, *53*, 7389−7403.
(74) Caneschi, A.; Dei, A.; Gatteschi, D.; Tangoulis, V. Antiferromagnetic Coupling in a Six-Coordinate High Spin Cobalt-(II)-Semiquinonato Complex. *Inorg. Chem.* **2002**, *41*, 3508−3512.
(75) Liang, H. W.; Kroll, T.; Nordlund, D.; Weng, T. C.; Sokaras, D.; Pierpont, C. G.; Gaffney, K. J. Charge and Spin-State Characterization of Cobalt Bis(o-Dioxolene) Valence Tautomers Using Co Kβ X-ray Emission and l-Edge X-ray Absorption Spectroscopies. *Inorg. Chem.* **2017**, *56*, 737−747.
(76) Protasenko, N. A.; Poddel'Sky, A. I.; Bogomyakov, A. S.; Somov, N. V.; Abakumov, G. A.; Cherkasov, V. K. Bis-o-Semiquinonato Complexes of Transition Metals with 5,7-di-tert-butyl-2-(pyridine-2-yl)benzoxazole. *Polyhedron* **2013**, *49*, 239−243.
(77) Bowman, A. C.; Milsmann, C.; Bill, E.; Lobkovsky, E.; Weyhermüller, T.; Wieghardt, K.; Chirik, P. J. Reduced N -Alkyl Substituted Bis(Imino)Pyridine Cobalt Complexes: Molecular and Electronic Structures for Compounds Varying by Three Oxidation States. *Inorg. Chem.* **2010**, *49*, 6110−6123.
(78) Hiller, M.; Sittel, T.; Wadepohl, H.; Enders, M. A New Class of Lanthanide Complexes with Three Ligand Centered Radicals: NMR Evaluation of Ligand Field Energy Splitting and Magnetic Coupling. *Chem. - Eur. J.* **2019**, *25*, 10668−10677.
(79) Tsukerblat, B. S.; Tarantul, A.; Müller, A. Antisymmetric Exchange and Pseudo Jahn-Teller Instability in Spin-Frustrated Metal Clusters. *J. Mol. Struct.* **2007**, *838*, 124−132.
(80) Van Den Heuvel, W.; Chibotaru, L. F. Elucidation of the Magnetism of $[Co_2PdCl_2(dpa)_4]$: Origin of a Large Temperature Domain of TIP Behavior. *Inorg. Chem.* **2009**, *48*, 7557−7563.
(81) Rohmer, M. M.; Liu, I. P. C.; Lin, J. C.; Chiu, M. J.; Lee, C. H.; Lee, G. H.; Bénard, M.; López, X.; Peng, S. M. Structural, Magnetic, and Theoretical Characterization of a Heterometallic Polypyridylamide Complex. *Angew. Chem., Int. Ed.* **2007**, *46*, 3533−3536.
(82) Nadurata, V. L.; Boskovic, C. Switching Metal Complexes via Intramolecular Electron Transfer: Connections with Solvatochromism. *Inorg. Chem. Front.* **2021**, *8*, 1840−1864.
(83) Fedushkin, I. L.; Skatova, A. A.; Chudakova, V. A.; Cherkasov, V. K.; Fukin, G. K.; Lopatin, M. A. Reduction of 1,2-Bis[(2,6-diisopropylphenyl)imino]acenaphthene (dpp-bian) with Alkali Metals− A Study of the Solution Behaviour of $(dpp\text{-}bian)^{n-}[M^+]_n$ (M = Li, Na; n = 1−4) with UV/Vis, ESR and ^{1}H NMR Spectroscopy. *Eur. J. Inorg. Chem.* **2004**, *2004*, 388−393.
(84) Robin, M. B.; Day, P. Mixed Valence Chemistry-A Survey and Classification. *Adv. Inorg. Chem. Radiochem.* **1968**, *10*, 247−422.
(85) Creutz, C. Mixed Valence Complexes of d5 - d6 Metal Centers. *Prog. Inorg. Chem.* **2007**, 1−73.
(86) Arnold, A.; Sherbow, T. J.; Sayler, R. I.; Britt, R. D.; Thompson, E. J.; Muñoz, M. T.; Fettinger, J. C.; Berben, L. A. Organic Electron Delocalization Modulated by Ligand Charge States in $[L_2M]^{n-}$ Complexes of Group 13 Ions. *J. Am. Chem. Soc.* **2019**, *141*, 15792−15803.
(87) Mörtel, M.; Oschwald, J.; Scheurer, A.; Drewello, T.; Khusniyarov, M. M. Molecular Valence Tautomeric Metal Complexes for Chemosensing. *Inorg. Chem.* **2021**, *60*, 14230−14237.
(88) Hearns, N. G. R.; Korčok, J. L.; Paquette, M. M.; Preuss, K. E. Dinuclear Cobalt Bis(Dioxolene) Complex Exhibiting Two Sequential Thermally Induced Valence Tautomeric Transitions. *Inorg. Chem.* **2006**, *45*, 8817−8819.
(89) Witt, A.; Heinemann, F. W.; Sproules, S.; Khusniyarov, M. M. Modulation of Magnetic Properties at Room Temperature: Coordination-Induced Valence Tautomerism in a Cobalt Dioxolene Complex. *Chem. - Eur. J.* **2014**, *20*, 11149−11162.

Modulation of Charge Distribution in Cobalt-α-Diimine Complexes towards Valence Tautomerism

Moya A. Hay,[⊥] Jett T. Janetzki,[⊥] Varshini J. Kumar, Robert W. Gable, Rodolphe Clérac, Alyona A. Starikova, Paul J. Low and Colette Boskovic[*]

Experimental and Synthetic Details

Synthesis

All synthetic manipulations were performed under anaerobic conditions under a N_2 atmosphere using standard Schlenk and glove box techniques, unless otherwise indicated. All chemicals purchased were of reagent grade or higher and used as received. Solvents THF and Et_2O which were dried using an MBraun SPS 7 system. Other solvents were dried over molecular sieves (3 Å) for a minimum of 3 days, and stored under N_2 on sieves until used. Solvents were degassed prior to use via 3 freeze-pump-thaw cycles. Molecular sieves were activated by heating at 300 °C for 48 hours and then cooled under vacuum. Ligands Ph-BIAN, 3,5-CF_3-Ph-BIAN, and 4-MeO-Ph-BIAN were prepared according to literature procedure (Ph-BIAN = bis[(phenyl)imino]acenaphthene; 3,5-CF_3-Ph-BIAN = bis[(3,5-bis(trifluoromethyl)phenyl)imino]acenaphthene; 4-MeO-Ph-BIAN = bis[(4-methoxy-phenyl)imino]acenaphthene).[1,2] Neutral ligands Ph-BIAN and 4-MeO-Ph-BIAN were reduced to forms Ph-BIAN^{2-} and 4-MeO-Ph-BIAN^{2-} and isolated as the protonated Ph-BIANH_2 and 4-MeO-Ph-BIANH_2, per a previously reported literature procedure.[3]

[Co(Ph-BIAN)$_3$](PF$_6$)$_2$ (1^{2+}(PF$_6$)$_2$). In air, a solution of $Co(OAc)_2 \cdot 4H_2O$ (0.0182 g, 0.103 mmol) in MeOH (10 ml) was added dropwise to a suspension of Ph-BIAN (0.0992 g, 0.299 mmol) in EtOH (40 ml). The solution rapidly changed color from orange to red. The reaction was allowed to stir for 1 hour at room temperature before concentrating to half the volume under reduced pressure. A solution of KPF_6 (0.0372 g, 0.202 mmol) in the minimum volume of MeOH was added dropwise to the concentrated reaction solution. A red precipitate then formed on slow addition of H_2O (30 ml). The precipitate was collected by filtration, washed with cold EtOH and diisopropyl ether (iPr$_2$O) and air-dried (0.11 g, 78%). Dark red single crystals suitable for X-ray diffraction were grown by layering a dichloroethane (DCE) solution of the crude compound with iPr$_2$O (0.082 g,

82%), with crystallographic analysis suggesting the formulation $\mathbf{1^{2+}(PF_6)_2}\cdot 2.5\text{DCE}\cdot 1.5i\text{Pr}_2\text{O}$. The bulk sample undergoes partial desolvation and analyzes as $\mathbf{1^{2+}(PF_6)_2}\cdot 0.5\text{DCE}\cdot 0.5i\text{Pr}_2\text{O}$. Elemental Analysis: $CoC_{76}H_{52}O_{0.5}N_2P_2F_{12}Cl$ [%], found: C 62.93, H 3.63, N 5.75; calc: C 63.10, H 3.97, N 5.81. Selected FT-IR data ($\bar{\nu}$ / cm^{-1}): ν_{CH} 3058 (w), ν_{CH} 2973 (w), ν_{CN} 1652 (w), ν_{CN} 1623 (m), ν_{CN} 1580 (m), 1482 (s), 1420 (m), 1287 (m), 1125 (m), 1050 (m), 835 (s), 730 (s), 696 (vs). ESI-MS analysis: calculated $[M]^{2+}$ at m/z = 527.66; found $[M]^{2+}$at m/z = 527.68. TGA data for the bulk samples are consistent with 0.5 molecules of DCE and 0.5 molecules of $i\text{Pr}_2\text{O}$. Pyrolysis-GCMS confirms loss of DCE (m/z 98) and $i\text{Pr}_2\text{O}$ (m/z 102) when heated to 180 °C.

[Co(Ph-BIAN)$_3$](PF$_6$) (1$^+$(PF$_6$)). A solution of $Co(OAc)_2\cdot 4H_2O$ (0.125 g, 0.500 mmol) in MeOH (10 mL) was added dropwise to a solution of Ph-BIAN (0.500 g, 1.50 mmol) in THF (40 mL). The solution rapidly turned from orange to red and allowed to stir for 1 hour at room temperature. Following this, $CoCp_2$ (0.0946 g, 0.500 mmol) in THF (10 mL) was added dropwise to the solution. The colour rapidly changed to green. The reaction was left stirring a further 2 hours. A solution of KPF_6 (0.092 g, 0.50 mmol) dissolved in a minimum volume of MeOH was added dropwise. The resulting solution was concentrated to approximately 2/3 the original volume and left in the freezer to yield a green crystalline solid, which was collected by vacuum-filtration and washed with Et_2O (0.18 g, 30%). Dark green rods suitable for X-ray diffraction were grown from the slow diffusion of Et_2O into a concentrated MeCN solution under N_2. It was not possible to reproducibly obtain an analytically pure bulk sample, and as such this compound was not used for bulk measurement. Crystallographic analysis afforded the formulation $\mathbf{1^+(PF_6)}\cdot 2Et_2O\cdot 0.6\text{MeCN}$.

[Co(Ph-BIAN)$_3$] (1). To an orange solution of Ph-BIAN (0.177 g, 0.533 mmol) in dry toluene (20 ml), a red-purple toluene/MeOH solution (20:2 ml) of Ph-BIANH_2 (0.0908 g, 0.270 mmol) and NaOMe (0.0286 g, 0.529 mmol) was added. A solution of $Co(OAc)_2\cdot 4H_2O$ (0.0482 g,

0.272 mmol) in EtOH (20 mL) was then added to afford a deep red-purple colored solution. The solution was evaporated to dryness under vacuum and then product extracted into dry toluene (20 ml), and filtered to remove the NaOAc by-product. The solution was reduced to 1/3 volume, affording a dark purple precipitate. The toluene mother liquor was removed via a cannula filter and the remaining solid washed with cold ethanol, collected (0.175 g, 59 %), and analyzed as **1**·0.8EtOH. Elemental Analysis: $CoC_{73.6}H_{52.8}O_{0.8}N_6$ [%], found: C 80.70, H 5.06, N 7.33; calc: C 80.88, H 4.87, N 7.69. Selected FT-IR data (ATR, $\bar{\nu}$ / cm^{-1}): 1657 (w), 1638 (w), 1622 (w), 1589 (m), 1588 (s) 1479 (m) 1257 (s), 1092 (s), 1021 (s), 797 (m), 780 (s), 688 (s), 528 (m), 504 (m). Single crystals were obtained by slow diffusion of pentane into a concentrated tetrahydrofuran (THF) solution under N_2, with the tentative formulation assigned as **1**·2.5THF·pentane.

[Co(3,5-CF_3-Ph-BIAN)$_3$] (**2**). Dicobalt octacarbonyl (0.0340 g, 0.100 mmol) was dissolved in dry toluene (15 mL). A solution of CF_3-Ph-BIAN (0.363 g, 0.600 mmol) in dry toluene (25 mL) was added in a steady stream, causing a rapid color change to dark purple. The solution was heated at 70 ^oC for 3 hours. The solution was then cooled to room temperature and left to stand overnight, after which dark green/purple crystals suitable for X-ray diffraction formed, which analyzed crystallographically as **2**·tol. The product was collected by vacuum filtration, washed with minimum cold hexane and air dried to yield desolvated **2** (0.21 g, 54%). Elemental Analysis: $C_{84}H_{36}N_6CoF_{36}$ [%], found: C, 53.77; H, 1,80; N, 4.38; calc: C, 53.89; H, 1.94; N, 4.49. Selected FT-IR data (ATR, $\bar{\nu}$ / cm^{-1}): 1600 (m), 1371 (s), 1273 (s), 1127 (m), 1016 (m), 969 (m), 889 (m), 769 (w), 726 (m), 703 (m), 680 (m), 532 (m).

[Co(4-MeO-Ph-BIAN)$_3$] (**3**) Compound **3** was synthesized in a manner analogous to that described for **1**, using 4-MeO-Ph-BIAN (0.167 g, 0.426 mmol), 4-MeO-Ph-BIANH_2 (0.0840 g, 0.230 mmol), NaOMe (0.0120 g, 0.222 mmol), and $Co(OAc)_2$ (0.0407 g, 0.230 mmol). Solid **3** was

collected as a dark black-red precipitate (0.193 g, 70 %) and analyzed as **3**·EtOH. Elemental Analysis: $CoC_{80}H_{66}O_7N_6$ [%], found: C 74.65, H 5.32, N 6.50; calc: C 74.93, H 5.19, N 6.55. Selected FT-IR data (ATR, $\bar{\nu}$ / cm^{-1}): 1643 (w), 1599 (m), 1576 (m), 1538 (w), 1498 (s), 1273 (m), 1238 (s), 1159 (m), 1027 (s), 829 (s), 775 (m), 610 (m), 537 (s). Single crystals suitable for X-ray analysis were isolated from toluene under a flow of steady N_2 and analyzed as solvent-free **3**.

[Co(4-MeO-Ph-BIAN)$_3$](PF$_6$)$_2$ (3^{2+}(PF$_6$)$_2$). Compound **3^{2+}(PF$_6$)$_2$** was synthesized in a manner analogous that that described for **1^{2+}(PF$_6$)$_2$**, from reaction of $Co(OAc)_2{\cdot}4H_2O$ (0.0182 g, 0.102 mmol), 4-MeO-Ph-BIAN (0.118 g, 0.300 mmol), and KPF_6 (0.0374 g, 0.203 mmol). The product was collected as a red powder (0.31 g, 64 %). Dark red single crystals suitable for X-ray diffraction were grown by layering a DCE solution with *i*Pr_2O and analyzed crystallographically as **3^{2+}(PF$_6$)$_2$**·DCE. The bulk sample analyzed as partially desolvated **3^{2+}(PF$_6$)$_2$**·0.6DCE (0.13 g, 81 %). Elemental Analysis $CoC_{79.2}H_{62.4}N_6O_6P_2F_{12}Cl_{1.2}$ [%], found: C 59.50, H 3.99, N 5.51; calc: C 59.99, H 3.97, N 5.30. Selected FT-TR data (ATR, $\bar{\nu}$ / cm^{-1}): 3030 (w), 2840 (w), 1650 (w), 1606 (m), 1582 (m), 1505 (s), 1439 (w), 1297 (m), 1264 (m), 1247 (s), 1027 (m), 828 (vs), 779 (m), 727 (m). ESI-MS analysis: calculated $[M]^{2+}$ at *m/z* = 618.18 found $[M]^{2+}$ at *m/z* = 617.73. TGA data are consistent with 0.6 molecules of DCE. Pyrolysis-GCMS confirms loss of DCE (*m/z* = 98) when heated to 180 °C.

Physical Methods

X-ray Data Collection and Structure Solution Single-crystal X-ray diffraction data for **1^{2+}(PF$_6$)$_2$**·2.5DCE·1.5*i*Pr_2O, **1^{+}(PF$_6$)**·2Et_2O·0.6MeCN, **2**, **3**, and **3^{2+}(PF$_6$)$_2$**·DCE, were collected using a Rigaku XtaLAB Synergy X-ray Diffractometer System using Cu Kα (λ = 1.5418 Å). The

data were reduced using CrysAlisPro software (Version 40.14a), employing a numerical absorption correction based on Gaussian integration over a multifaceted crystal.[4] Single-crystal X-ray diffraction data for neutral compound **1** was collected on the MX1[5] beamline at the Australian Synchrotron fitted with a silicon double crystal monochromator, the wavelength being tuned to approximate Mo Kα radiation (λ = 0.71073 Å). Data reduction was performed using XDS, using strong multi-scan absorption correction in SADABS. Crystals were transferred directly from the mother liquor to crystallographic oil to prevent loss of crystallinity/solvent. Structures were solved using SHELXT[6] routine and refined using a full matrix least squared procedure based on F^2 using SHELXL within OLEX2.[7] Additional refinement details are available in the Supporting Information. Powder X-ray diffraction (PXRD) data were measured on a Rigaku XtaLAB Synergy Dual Wavelength Rotating Anode X-ray Diffractometer System using CuKα (λ = 1.5418 Å) at room temperature for samples except $\mathbf{1}^{2+}(\mathbf{PF_6})_2$. PXRD data for $\mathbf{1}^{2+}(\mathbf{PF_6})_2$ was measured on a Rigaku Oxford Diffraction SuperNova Dual Wavelength single-crystal X-ray diffractometer using Mo Kα radiation at room temperature. Powder samples were prepared by grinding the dry bulk sample for $\mathbf{1}^{2+}(\mathbf{PF_6})_2$ and $\mathbf{3}^{2+}(\mathbf{PF_6})_2$, and gently crushing crystalline samples pf **1**, **2** and **3**. In each case, the sample was loaded into a borosilicate glass capillary for measurement. Data were collected between 2θ of 5 and 50° with an exposure time of 120 seconds per frame and processed using CrysAlisPro.

Solid-State Magnetic Measurements The magnetization measurements were performed on a Quantum Design MPMS-XL SQUID magnetometer operating between 1.8 and 400 K and applied dc fields of up to 7 T. These measurements were performed on powder or microcrystalline samples (10.39, 9.58, 10.60, 11.40 and 8.60 mg for $\mathbf{1}^{2+}(\mathbf{PF_6})_2$·0.5DCE·0.5i$Pr_2O$, $\mathbf{3}^{2+}(\mathbf{PF_6})_2$·0.6DCE, **1**·0.8EtOH, **2**, and **3**·EtOH, respectively) restrained in mineral oil (in order to avoid field-induced torqueing; mass between 10 and 20 mg) and sealed in polypropylene bags (size ~3 × 0.5 × 0.02 cm^3;

mass between 14 and 60 mg) under argon. Raw data were corrected for the intrinsic diamagnetic contributions of the sample,[54] the mineral oil and the sample holder.

Electronic and Infrared Spectroscopy All solutions were prepared in an inert Nitrogen atmosphere inside a nitrogen filled glovebox. Solution-state UV-Visible spectra in MeCN, THF, and toluene were measured on an Agilent Technology Cary 60 UV-Visible spectrometer and using a PerkinElmer Lambda 1050 in the UV-vis-NIR range. For all measurements in CH_2Cl_2, UV-vis spectra of the compounds were recorded in a sealed quartz cuvette of 1 mm pathlength. The data were recorded using a Cary 5000 UV-vis-NIR spectrometer. Static IR spectra of compounds were recorded using a Cary 660 FTIR spectrometer in a Specac solution cell fitted with CaF_2 windows and a nominal path length of 0.5 mm. Solid-state attenuated total reflectance infrared spectra were measured on a Bruker Alpha spectrometer and normalized as absorbance spectra

Electrochemistry and Spectroelectrochemistry Cyclic voltammetry measurements were conducted in a standard three-electrode cell, with Pt disc working electrode, Pt wire counter and pseudo-reference electrodes under a N_2 atmosphere inside the glove box with data collected from an EmStat^{3+} potentiostat. The measurements were carried out in 0.1 M NBu_4PF_6 / CH_2Cl_2 solution and the voltammograms were internally referenced against the Fc/Fc^+ redox couple. Spectroelectrochemistry measurements were conducted in a transmission cell of Hartl design fitted with CaF_2 windows[8] and controlled by the EmStat^{3+} from solutions of the analyte (ca. 1mM) in 0.1 M NBu_4PF_6 / CH_2Cl_2. The data was recorded on a Cary 5000 UV-vis-NIR spectrometer.

Other Elemental C, H, N analyses were performed at the Campbell Microanalytical Laboratory, University of Otago. Thermogravimetric analysis were performed on a Mettler Toledo TGA/SDTA851e using a ramp rate of 5 °C min^{-1} to a maximum temperature of 400 °C in a flow of N_2. Electrospray ionization mass spectrometry was performed on an Agilent 6220 Series TOF on

samples in acetonitrile solution. Pyrolysis-gas chromatography mass spectrometry (GCMS) was performed by the TrACEES (Trace Analysis for Chemical, Earth and Environmental Sciences) platform at the University of Melbourne.

Computational Methods Density functional theory (DFT) calculations for all compounds were performed using the Gaussian 16[9] with the UTPSSh functional[10,11] and the 6-311++G(d,p) basis set. The stationary points on the potential energy surface were located by full geometry optimization with calculation of force constants and checked for the stabilities of DFT wave function. The atomic coordinates obtained from experimental crystal structures were used as input files, including the counterions. The estimation of exchange spin coupling parameters J (in cm^{-1}; $= -2JS_1 \cdot S_2$) was carried out by means of calculation of all possible charge distributions in the framework of 'broken symmetry' formalism and with the use of generalized spin-projection method developed by Yamaguchi and co-workers.[12] Figures were prepared using ChemCraft with the calculated atomic coordinates as input parameters.[13]

Additional Single Crystal X-ray Diffraction Refinement Details

Compound $\mathbf{1^{2+}(PF_6)_2 \cdot 2.5DCE \cdot 1.5}$*i*$\mathbf{Pr_2O}$ Crystals were found to be consistently twinned; attempts to resolve the twin components were unsuccessful and so the data was processed as a single crystal. The oxidation state of the metal in the two crystallographically independent molecules in the asymmetric unit were both Co^{II} (in-line with bond length analysis) necessitating four PF_6^- anions. Only three PF_6^- anions were able to be located, two of the PF_6^- anions were ordered, and one was disordered over two orientations. It was not possible to find the location of the other anion, and so the remaining electron density was located in solvent voids which appeared to contain a mixture of

disordered/diffuse solvent and disordered PF_6^- anions, necessary for charge balance. The solvent mask routine in the OLEX2[7] program indicated two solvent voids in the unit cell, each with a volume and electron density consistent with one PF_6^- anion, five 1,2-dichloromethane molecules and three diisopropyl ether molecules. This gives a formula of $\mathbf{1^{2+}(PF_6)_2}\cdot 2.5DCE\cdot 1.5i Pr_2O$ or a composition of $\mathbf{(1^{2+})_2(PF_6)_4}\cdot 5DCE\cdot 3\ i Pr_2O$ in the asymmetric unit.

Compound $\mathbf{1^+(PF_6)\cdot 2Et_2O\cdot 0.6MeCN}$ This structure contains one co-crystallised molecule of diethyl ether which is well-resolved, with one of the terminal carbon atoms exhibiting disorder over 2 positions; the relative occupancies were refined freely. The use of the SADI restraint over the two parts of the disordered diethyl ether was necessary to resolve the disorder. Diffuse and disorder solvent was also indicated in the data, with the solvent mask routine in the OLEX2 program indicating two solvent accessible voids in the unit cell, each with a volume consistent with 1 molecule of diethyl ether, and 0.5 molecules of acetonitrile.

1·2.5THF·pentane There were numerous attempts to collect single-crystal data for compound **1**, making use of both in-house and synchrotron facilities. However, due to the weakly diffracting nature of the crystals, only a fraction of the complete data was able to be collected; the weak data resulted in a high R_{int} value. Despite numerous attempts to prepare samples via multiple methods, all gave poorly diffracting crystals. The data presented here are the best quality data that were able to be obtained. Despite this, the structure was able to be solved and refined satisfactorily. The solvent mask routine in the OLEX2 program indicated solvent voids in the unit cell, with a volume and electron density consistent with the solvents of crystallization, which were assigned as 2.5 molecules of tetrahydrofuran (THF) and 1 molecule of pentane.

Compound 2·tol Positional disorder of the CF_3 moieties was observed for compound **2**, with both the SIMU restraint and EADP constraint employed where necessary. Modelling over additional

positions did not improve the overall refinement, but due to the residual electron difference a maximum electron density peak of 1.3 is observed. One molecule of toluene is present within the lattice, disordered over two positions with the relative occupancies refined freely. Adjacent atoms in the toluene molecule were also constrained to have the same atomic displacement parameters using the EADP constraint.

Compound $\mathbf{3^{2+}(PF_6)_2}$·DCE Systematic absences were consistent with the space groups *Pnna* and *Pna*2_1 and a satisfactory solution (using SHELXT) was obtained in the latter space group; the final *R* value was 0.043. The entire cation, two PF_6^- anions and one 1,2-dichloroethane (DCE) molecule comprise the asymmetric unit. One of the methoxy groups of the ligand was found to be disordered over two orientations (0.42(2):0.58(2)); the carbon atoms were assigned equal ADP values. One PF_6^- anion was found to be disordered over two orientations (0.740(4):0.260(4)) while the two other sites each appeared to be a mixture of PF_6^- and 1,2-dichloroethane. In one site, the ratio of the two moieties was 0.733(3):0.267(3) while in the other position the ratio was 0.267(3):0.733(3) giving an overall formula of $\mathbf{3^{2+}(PF_6)_2}$·DCE. The atoms of the PF_6^- and DCE groups were restrained to ideal geometry, with the F atoms of each component having similar ADP values. The crystal was refined as a racemic twin, the contributions were 0.943(5):0.057(5).

CheckCIF suggested that a solution should be possible in the centrosymmetric space group *Pnna*. E-statistics and a Wilson plot also did suggest the possibility that the space group was centrosymmetric. However, inspection of the data showed that 1314 additional reflections would have to be rejected as systematically absent for *Pnna*, over those already rejected for *Pna*2_1, many of which had $I > 10\ \sigma(I)$. It was, however, possible to obtain a solution in *Pnna*, using SHELXS; half of the molecule is unique with the cobalt lying on a 2-fold axis. This should give positions for one PF_6^- anion and half of a 1,2-dichloroethane molecule in the asymmetric unit. This could be

either an ordered arrangement or a disordered arrangement where each position contains a mixture of PF_6^- and 1,2-dichloroethane. Refinement of all atoms of the cation in *Pnna* gave one site attributable to a PF_6^- anion which was disordered over two orientations; this site did not appear to have any contribution from the 1,2-dichloroethane. A second position had to be refined as a 50:50 mixture of PF_6^- and 1,2-dichloroethane, due to the symmetry of the space group, and as required for charge balance. It was difficult to refine the structure below $R = 0.112$. Refining only the atoms of the cation, using solvent mask to account for the contribution of the solvent and anions, did not improve the *R* value.

This is consistent with the true space group being $Pna2_1$; the cations in the structure are almost centrosymmetrically related, but the anions and solvent are not. In the space group $Pna2_1$ the $[CoL]^{2+}$ cation is unique, there is one fully occupied PF_6^- but the other two positions are an asymmetric mixture of PF_6^- and 1,2-dichloroethane. For the higher symmetry space group to be retained, the anion/solvent site would have to have a 50:50 mixture of PF_6^- and 1,2-dichloroethane. Since there is an asymmetric distribution of PF_6^- and 1,2-dichloroethane in the crystal, the symmetry is lowered, which results in the correct space group being $Pna2_1$.

Compound 3 There were numerous attempts to collect single-crystal data for compound **3**, making use of both in-house and synchrotron facilities. Many samples were prepared via multiple methods. However, due to the weakly diffracting nature of the crystals, from all preparations, only a fraction of the complete data was able to be collected; the weak data resulted in a high value of the R_{int} value in all cases. The dataset presented here is the best quality data. Despite this, the structure was able to be solved and refined satisfactorily.

Table S1. Tabulated bond lengths taken from geometry optimized electromers in the gas phase (DFT UTPSSh/6-311++G(d,p) method) of $\mathbf{1^{2+}(PF_6)_2}$ and $\mathbf{1^{+}(PF_6)}$ with the experimental values determined via single-crystal X-ray diffraction taken from Table 1 (main text). The electromer with best agreement to the experimental has been highlighted in light grey.

	Compound $1^{2+}(PF_6)_2$				**Compound $1^{+}(PF_6)$**			
	HS-Co^{II}-$(L^0)_3$	**LS-Co^{II}-$(L^0)_3$**	**LS-Co^{III}-$(L^{\bullet-})(L^0)_2$**	**Exp[a]**	**HS-Co^{II}-$(L^{\bullet-})(L^0)_2$**	**LS-Co^{II}-$(L^{\bullet-})(L^0)_2$**	**LS-Co^{III}-$(L^{\bullet-})_2(L^0)$**	**Exp**
$Co–N_1$	2.187	2.005	1.986	2.127(2)	2.155	2.246	1.967	2.112(3)
$Co–N_2$	2.160	2.266	1.997	2.154(2)	2.148	1.994	1.987	2.127(3)
$Co–N_3$	2.167	1.997	2.021	2.133(2)	2.189	2.022	2.009	2.137(3)
$Co–N_4$	2.159	1.996	1.992	2.123(2)	2.187	2.264	2.010	2.153(3)
$Co–N_5$	2.184	2.244	1.980	2.150(2)	2.161	1.986	1.988	2.104(3)
$Co–N_6$	2.169	1.988	1.975	2.159(2)	2.163	1.994	1.966	2.123(3)
$C_1–N_1$	1.290	1.297	1.296	1.288(3)	1.313	1.297	1.337	1.296(4)
$C_2–N_2$	1.289	1.289	1.295	1.283(3)	1.314	1.308	1.337	1.297(4)
$C_3–N_3$	1.291	1.298	1.294	1.283(3)	1.292	1.297	1.296	1.290(4)
$C_4–N_4$	1.292	1.300	1.295	1.276(3)	1.292	1.288	1.296	1.286(4)
$C_5–N_5$	1.288	1.289	1.331	1.277(4)	1.308	1.326	1.337	1.297(4)
$C_6–N_6$	1.290	1.299	1.341	1.278(4)	1.309	1.326	1.337	1.302(4)
$C_1–C_2$	1.514	1.507	1.494	1.522(3)	1.470	1.483	1.428	1.484(3)
$C_3–C_4$	1.510	1.488	1.493	1.508(4)	1.512	1.509	1.496	1.493(4)
$C_5–C_6$	1.508	1.504	1.430	1.512(4)	1.477	1.443	1.428	1.480(4)

[a] Experimental bond lengths for **1^{2+}A in $1^{2+}(PF_6)_2$**·0.5DCE·0.5*i*Pr_2O.

Table S2. Tabulated bond lengths taken from geometry optimized electromers in the gas phase (DFT UTPSSh/6-311++G(d,p) method) of **1** and **2** with the experimental values determined via single-crystal X-ray diffraction taken from Table 1 (main text). The electromer with best agreement to the experimental has been highlighted in light grey.

	Compound 1				**Compound 2**		
	HS-Co^{II}-$(L^{\bullet-})_2(L^0)$	**LS-Co^{II}-$(L^{\bullet-})_2(L^0)$**	**LS-Co^{III}-$(L^{\bullet-})_3$**	**Exp**	**HS-Co^{II}-$(L^{\bullet-})_2(L^0)$**	**LS-Co^{III}-$(L^{\bullet-})_3$**	**Exp**
$Co–N_1$	2.172	2.260	1.989	2.142(4)	2.177	1.992	2.114(2)
$Co–N_2$	2.173	2.000	1.989	2.116(4)	2.175	1.992	2.135(2)
$Co–N_3$	2.168	2.259	1.989	2.142(4)	2.184	1.990	2.114(2)
$Co–N_4$	2.172	1.999	1.989	2.116(4)	2.185	1.997	2.135(2)
$Co–N_5$	2.168	1.993	1.989	2.096(4)	2.175	1.997	2.131(2)
$Co–N_6$	2.167	1.992	1.989	2.096(4)	2.176	1.990	2.131(2)
$C_1–N_1$	1.317	1.307	1.335	1.299(6)	1.325	1.339	1.302(3)
$C_2–N_2$	1.317	1.322	1.335	1.305(5)	1.323	1.339	1.303(3)
$C_3–N_3$	1.317	1.322	1.335	1.299(6)	1.318	1.338	1.302(3)
$C_4–N_4$	1.317	1.307	1.335	1.305(5)	1.318	1.341	1.303(3)
$C_5–N_5$	1.318	1.330	1.335	1.284(5)	1.323	1.341	1.330(3)
$C_6–N_6$	1.318	1.330	1.335	1.284(5)	1.325	1.338	1.330(3)
$C_1–C_2$	1.460	1.463	1.429	1.460(7)	1.456	1.429	1.481(3)
$C_3–C_4$	1.460	1.463	1.429	1.460(7)	1.465	1.430	1.481(3)
$C_5–C_6$	1.459	1.438	1.429	1.474(9)	1.458	1.430	1.440(4)

Table S3. Tabulated bond lengths taken from geometry optimized electromers in the gas phase (DFT UTPSSh/6-311++G(d,p) method) of $\mathbf{3^{2+}(PF_6)_2}$ and **3** with the experimental values determined via single-crystal X-ray diffraction taken from Table 1 (main text). The electromer with best agreement to the experimental has been highlighted in light grey.

	Compound $3^{2+}(PF_6)_2$			Compound **3**			
	HS-Co^{II}-$(L^0)_3$	LS-Co^{II}-$(L^0)_3$	Exp	HS-Co^{II}-$(L^{\bullet-})_2(L^0)$	LS-Co^{II}-$(L^{\bullet-})_2(L^0)$	LS-Co^{III}-$(L^{\bullet-})_3$	Exp
Co–N_1	2.214	1.997	2.120(3)	2.168	2.261	1.988	2.182(4)
Co–N_2	2.193	1.993	2.141(3)	2.169	1.999	1.988	2.114(5)
Co–N_3	2.165	2.291	2.123(3)	2.168	2.261	1.988	2.182(4)
Co–N_4	2.167	2.012	2.120(3)	2.166	1.999	1.988	2.114(5)
Co–N_5	2.216	1.976	2.142(3)	2.168	1.987	1.988	2.106(5)
Co–N_6	2.133	2.264	2.135(3)	2.167	1.987	1.988	2.106(5)
C_1–N_1	1.293	1.303	1.286(5)	1.316	1.308	1.335	1.300(6)
C_2–N_2	1.297	1.301	1.298(5)	1.317	1.321	1.335	1.318(7)
C_3–N_3	1.294	1.283	1.282(5)	1.317	1.321	1.335	1.300(6)
C_4–N_4	1.294	1.303	1.286(5)	1.317	1.308	1.335	1.318(7)
C_5–N_5	1.299	1.301	1.288(5)	1.318	1.331	1.335	1.279(7)
C_6–N_6	1.293	1.298	1.290(5)	1.318	1.331	1.335	1.279(7)
C_1–C_2	1.507	1.486	1.504(5)	1.461	1.463	1.429	1.449(8)
C_3–C_4	1.507	1.500	1.511(5)	1.460	1.463	1.429	1.449(8)
C_5–C_6	1.505	1.499	1.508(5)	1.459	1.437	1.429	1.501(11)

Table S4. Spin states (S), total energies without (E) and with (E^{ZPE}) taking into account for zero-point harmonic vibrations, total enthalpies (H^{298}) and expectation values of the spin-squared operator ($\hat{S}^2$) of complexes $\mathbf{1^{2+}(PF_6)_2}$, $\mathbf{1^{+}(PF_6)}$, **1**, **2**, **3** and $\mathbf{3^{2+}(PF_6)_2}$ calculated by the DFT UTPSSh/6-311++G(d,p) method.

	Electromer	S	E (a.u.)	E^{ZPE} (a.u.)	H^{298} (a.u.)	$\hat{S}^2$
$\mathbf{1^{2+}(PF_6)_2}$	HS-Co^{II}-$(L^0)_3$	3/2	-6366.455958	-6365.424788	-6365.344156	3.767
	LS-Co^{III}-$(L^{\bullet-})(L^0)_2$	1/2	-6366.441549	-6365.400993	-6365.323528	0.765
	LS-Co^{II}-$(L^0)_3$	1/2	-6366.451565	-6365.418800	-6365.339040	0.774
$\mathbf{1^{+}(PF_6)}$	HS-Co^{II}-$(L^{\bullet-})(L^0)_2$	2	-5425.664388	-5424.655691	-5424.583314	6.019
	αβ*	1	-5425.674022	–	–	2.606
	LS-Co^{III}-$(L^{\bullet-})_2(L^0)$	1	-5425.657473	-5424.645174	-5424.574425	2.017
	αβ	0	-5425.657568	–	–	1.030
	LS-Co^{II}-$(L^{\bullet-})(L^0)_2$	1	-5425.660854	-5424.650544	-5424.580731	2.037
	αβ	0	-5425.660677	–	–	1.040
1	HS-Co^{II}-$(L^{\bullet-})_2(L^0)$	5/2	-4484.886573	-4483.900142	-4483.836280	8.769
	αβα	3/2	-4484.889775	–	–	4.446
	αββ	1/2	-4484.890694	–	–	2.426
	LS-Co^{III}-$(L^{\bullet-})_3$	3/2	-4484.885484	-4483.894975	-4483.832663	3.777
	αβ	1/2	-4484.885189	–	–	1.775
	LS-Co^{II}-$(L^{\bullet-})_2(L^0)$	3/2	-4484.880435	-4483.891018	-4483.827643	3.781
	αβα	1/2	-4484.878441	–	–	1.862
	βαα	1/2	-4484.876847	–	–	1.810
2	HS-Co^{II}-$(L^{\bullet-})_2(L^0)$	5/2	-8530.570926	-8529.536573	-8529.426844	8.768
	αβα	3/2	-8530.574141	–	–	4.451
	αββ	1/2	-8530.573101	–	–	2.464
	LS-Co^{III}-$(L^{\bullet-})_3$	3/2	-8530.564261	-8529.525586	-8529.417558	3.777
	αβ	1/2	-8530.563805	–	–	1.776
3	HS-Co^{II}-$(L^{\bullet-})_2(L^0)$	5/2	-5172.237079	-5171.057189	-5170.978537	8.770
	αβα	3/2	-5172.240006	–	–	4.539
	αββ	1/2	-5172.237944	–	–	2.507
	LS-Co^{III}-$(L^{\bullet-})_3$	3/2	-5172.241028	-5171.057717	-5170.979287	3.777
	αβ	1/2	-5172.240606	–	–	1.775
	LS-Co^{II}-$(L^{\bullet-})_2(L^0)$	3/2	-5172.232667	-5171.052615	-5170.973141	3.780
	αβα	1/2	-5172.229991	–	–	1.866
	βαα	1/2	-5172.228274	–	–	1.823
$\mathbf{3^{2+}(PF_6)_2}$	HS-Co^{II}-$(L^0)_3$	3/2	-7053.826731	-7052.602063	-7052.505635	3.767
	LS-Co^{II}-$(L^0)_3$	1/2	-7053.823817	-7052.597669	-7052.502020	0.776

α corresponds to spin-up, β corresponds to spin-down.

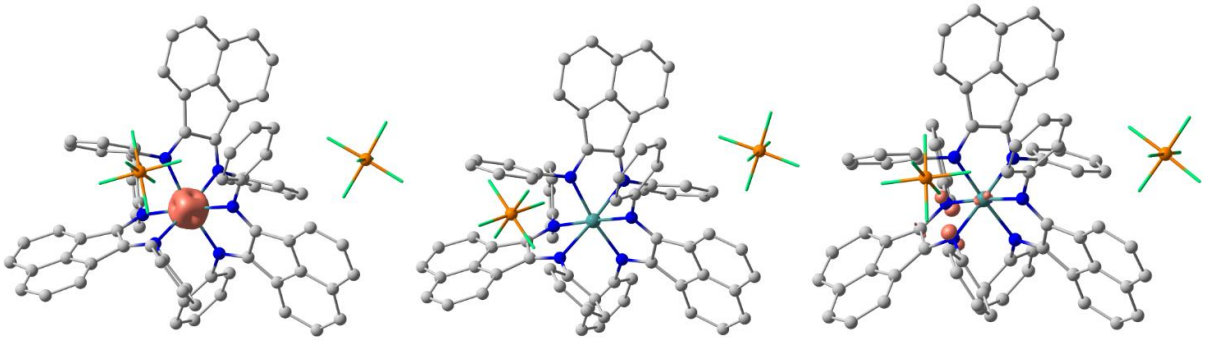

HS-Co^{II}-(L^{0})$_3$ **LS-Co^{II}-(L^{0})$_3$** **LS-Co^{III}-(L$^{\bullet-}$)(L^{0})$_2$**

Figure S1. Spin density distributions in the electromers of **1^{2+}(PF$_6$)$_2$** calculated by DFT UTPSSh/6-311++G(d,p) method. Hydrogen atoms are omitted for clarity. Contour value = 0.03 e Å^{-3}.

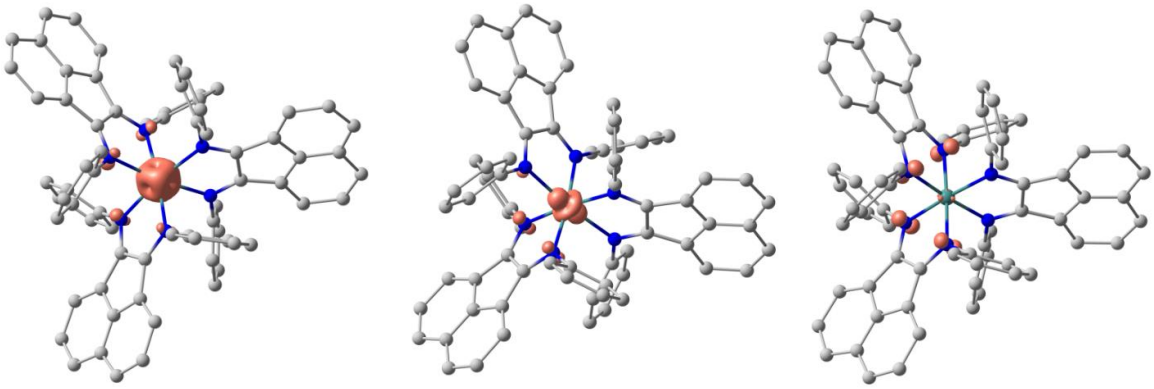

HS-Co^{II}-(L$^{\bullet-}$)(L^{0})$_2$ **LS-Co^{II}-(L$^{\bullet-}$)(L^{0})$_2$** **LS-Co^{III}-(L$^{\bullet-}$)$_2$(L^{0})**

Figure S2. Spin density distributions in the electromers of **1^{+}(PF$_6$)** calculated by DFT UTPSSh/6-311++G(d,p) method. Hydrogen atoms and counterions are omitted for clarity. Contour value = 0.03 e Å^{-3}.

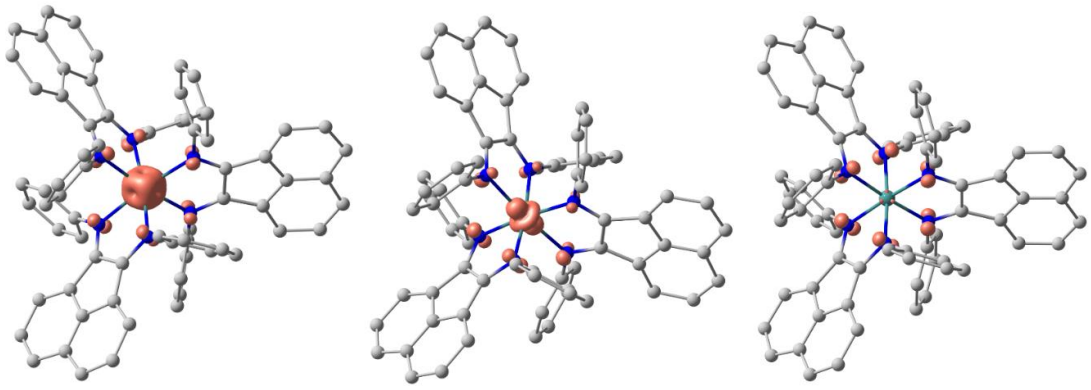

HS-Co^{II}-(L$^{\bullet-}$)$_2$(L^0) **LS-Co^{II}-(L$^{\bullet-}$)$_2$(L^0)** **LS-Co^{III}-(L$^{\bullet-}$)$_3$**

Figure S3. Spin density distributions in the electromers of **1** calculated by DFT UTPSSh/6-311++G(d,p) method. Hydrogen atoms are omitted for clarity. Contour value = 0.03 e Å^{-3}.

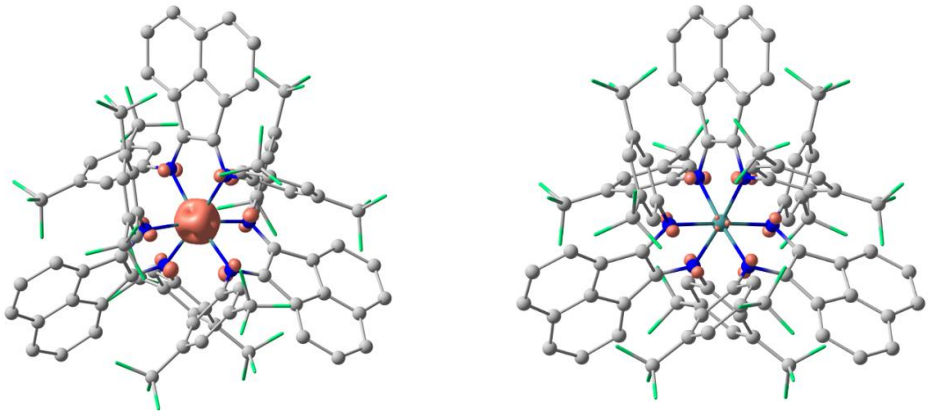

HS-Co^{II}-(L$^{\bullet-}$)$_2$(L^0) **LS-Co^{III}-(L$^{\bullet-}$)$_3$**

Figure S4. Spin density distributions in the electromers of **2** calculated by DFT UTPSSh/6-311++G(d,p) method. Hydrogen atoms are omitted for clarity. Contour value = 0.03 e Å^{-3}.

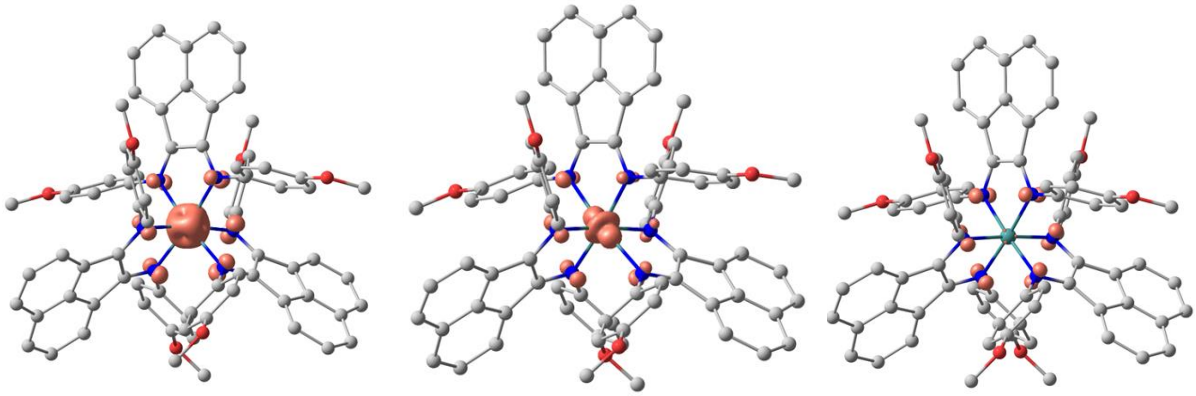

HS-Co^{II}-(L$^{\bullet-}$)$_2$(L^0) **LS-Co^{II}-(L$^{\bullet-}$)$_2$(L^0)** **LS-Co^{III}-(L$^{\bullet-}$)$_3$**

Figure S5. Spin density distributions in the electromers of **3** calculated by DFT UTPSSh/6-311++G(d,p) method. Hydrogen atoms are omitted for clarity. Contour value = 0.03 e Å^{-3}.

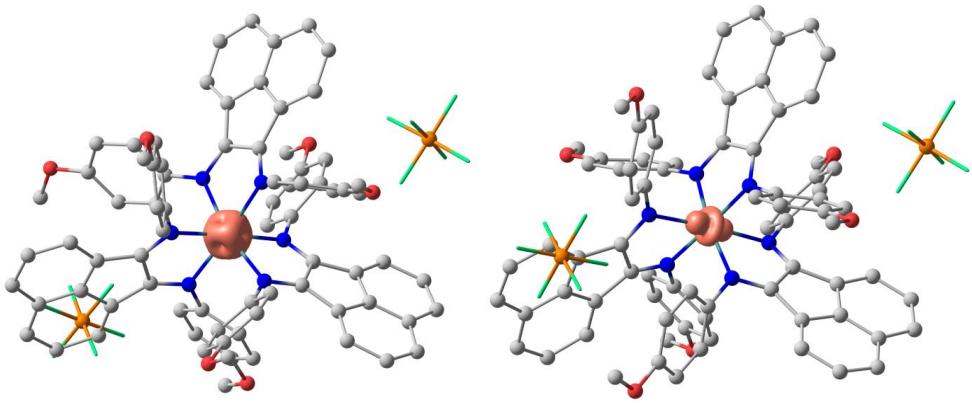

HS-Co^{II}-(L^0)$_3$ **LS-Co^{II}-(L^0)$_3$**

Figure S6. Spin density distributions in the electromers of **3^{2+}(PF$_6$)$_2$** calculated by DFT UTPSSh/6-311++G(d,p) method. Hydrogen atoms are omitted for clarity. Contour value = 0.03 e Å^{-3}.

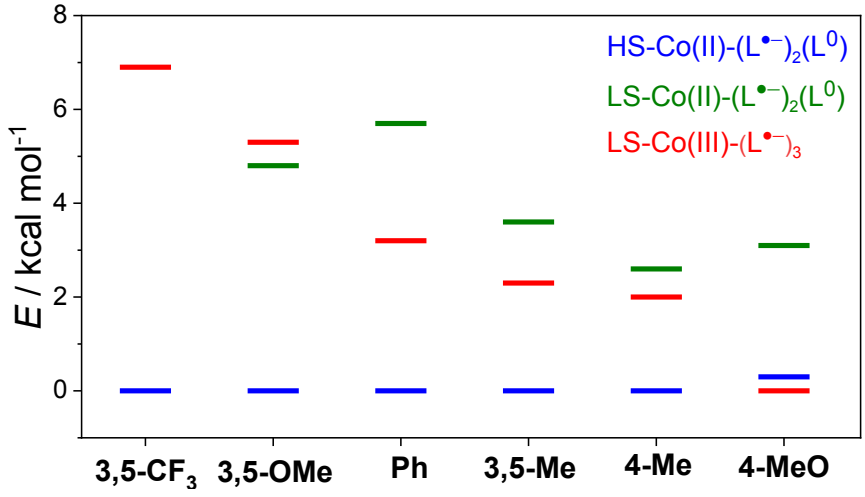

Figure S7. Schematic showing the different calculated relative energies of the different electromeric forms for the neutral compounds with Ar = 3,5-CF_3-Ph (**2**), 3,5-OMe-Ph, Ph (**1**), 3,5-Me-Ph, 4-Me-Ph, and 4-MeO-Ph (**3**) calculated by DFT (UTPSSh/6-311++G(d,p)) with ZPE.

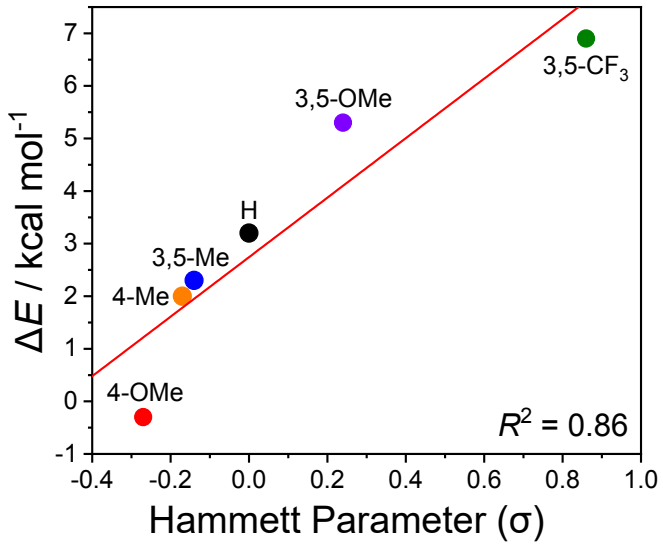

Figure S8. Correlation between the calculated energy difference (ΔE / kcal mol^{-1}) between the HS-Co^{II}-L^0 and LS-Co^{III}-$L^{\bullet-}$ tautomer states for [Co(Ar-BIAN)$_3$] versus the σ Hammett parameters for the relevant aryl substituents: H (**1**), 3,5-CF_3 (**2**), 4-OMe (**3**), 3,5-Me, 4-Me, and 3,5-MeO. Inset R^2 value for the linear fit.[14,15]

Table S5. Exchange coupling parameters (cm^{-1}) calculated by the DFT UTPSSh/6-311++G(d,p) method.

	Electromer	*J* (HS-Co^{II}···$L^{\bullet-}$)	*J* (LS-Co^{II}···$L^{\bullet-}$)	*J* ($L^{\bullet-}$···$L^{\bullet-}$)
$1^{+}(PF_6)$	HS-Co^{II}-($L^{\bullet-}$)(L^0)$_2$	–620		
	LS-Co^{III}-($L^{\bullet-}$)$_2$(L^0)			–21
	LS-Co^{II}-($L^{\bullet-}$)(L^0)$_2$		39	
1	HS-Co^{II}-($L^{\bullet-}$)$_2$(L^0)	–143		–218
	LS-Co^{III}-($L^{\bullet-}$)$_3$			32
	LS-Co^{II}-($L^{\bullet-}$)$_2$(L^0)		400	47
2	HS-Co^{II}-($L^{\bullet-}$)$_2$(L^0)	–76		–401
	LS-Co^{III}-($L^{\bullet-}$)$_3$			50
3	HS-Co^{II}-($L^{\bullet-}$)$_2$(L^0)	–498		–30
	LS-Co^{III}-($L^{\bullet-}$)$_3$			46
	LS-Co^{II}-($L^{\bullet-}$)$_2$(L^0)		493	112

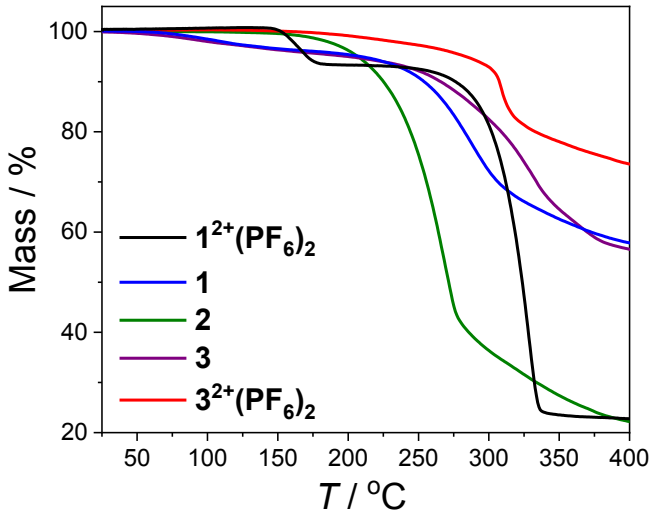

Figure S9. TGA data for **$1^{2+}(PF_6)_2$**·0.5DCE·0.5*i*Pr_2O, **1**·0.8EtOH, **2**, **3**·EtOH and **3^{2+}**$(PF_6)_2$·DCE.

Table S6. Crystallographic data and structure refinement parameters for compounds **1**$^{2+}$**(PF$_6$)$_2$**·2.5DCE·1.5iPr$_2$O, **1**$^{+}$**(PF$_6$)**·2Et$_2$O·0.6MeCN and **1**·2.5THF·pentane.

	1^{2+}**(PF$_6$)$_2$**	**1**$^{+}$**(PF$_6$)**	**1**
Empirical formula	$Co_2C_{208}H_{158}N_{12}P_2F_{12}Cl_{10}O_3$	$CoC_{81}H_{67.5}N_{6.5}O_2PF_6$	$CoC_{87}H_{80}N_6O_{2.5}$
Formula weight	1746.67	1367.81	1308.50
Temperature (K)	100.0(2)	100.0(2)	100.0(1)
Crystal system	triclinic	triclinic	monoclinic
Space group	*P*-1	*P*-1	*C*2/*c*
a (Å)	16.96693(18)	12.59860(10)	18.930(4)
b (Å)	16.97887(18)	15.92660(10)	17.230(3)
c (Å)	27.8956(4)	18.05520(10)	21.140(4)
α (°)	94.6345(10)	93.2470(10)	90
β (°)	93.7103(10)	103.4190(10)	104.09(3)
γ (°)	90.0960(9)	102.1310(10)	90
Volume (Å^3)	7992.90(17)	3424.00(4)	6688(2)
Z	4	2	4
ρ_{calc} (g/cm^3)	1.451	1.327	1.300
μ (mm^{-1})	4.284	2.764	0.315
F(000)	3596.0	1422.0	2764.0
Crystal size (mm^3)	0.318 × 0.22 × 0.055	0.204 × 0.109 × 0.068	0.1 × 0.1 × 0.1
Radiation	Cu Kα (λ = 1.54184)	Cu Kα (λ = 1.54184)	Mo Kα (λ = 0.71073)
2θ range for data collection (°)	5.222 to 155.154	5.062 to 156.464	3.242 to 58.916
Index ranges	$-21 \le h \le 21$ $-21 \le k \le 18$ $-34 \le l \le 35$	$-15 \le h \le 15$ $-20 \le k \le 20$ $-22 \le l \le 20$	$-24 \le h \le 25$ $-21 \le k \le 23$ $-28 \le l \le 28$
Reflections collected	106856	61038	90685
Independent reflections	32616 [R_{int} = 0.0313, R_{sigma} = 0.0321]	14392 [R_{int} = 0.0480, R_{sigma} = 0.0375]	8371 [R_{int} = 0.1073, R_{sigma} = 0.0569]
Data/restraints/parameters	32616/2038/1743	14392/820/834	8371/342/358
Goodness-of-fit on F^2	1.026	1.100	0.929
Final *R* indexes [$I \ge 2\sigma(I)$]	R_1 = 0.0617 wR_2 = 0.1867	R_1 = 0.0486 wR_2 = 0.1350	R_1 = 0.0822 wR_2 = 0.2469
Final *R* indexes [all data]	R_1 = 0.0674 wR_2 = 0.1921	R_1 = 0.0524 wR_2 = 0.1378	R_1 = 0.1689 wR_2 = 0.3143
Largest diff. peak/hole (e Å^{-3})	0.63/-0.50	0.62/-0.58	0.52/-0.20

Table S7. Crystallographic data and structure refinement parameters for compounds **2**·tol, $\mathbf{3}^{2+}(\mathbf{PF_6})_2$·DCE and **3**.

	2	$\mathbf{3}^{2+}(\mathbf{PF_6})_2$	**3**
Empirical formula	$CoC_{98}H_{52}N_6F_{36}$	$CoC_{80}H_{64}N_6O_6Cl_2P_2F_{12}$	$CoC_{78}H_{60}N_6O_6$
Formula weight	2056.38	1625.14	1236.25
Temperature (K)	100.0(1)	100.15	120.0(2)
Crystal system	monoclinic	orthorhombic	orthorhombic
Space group	*C*2/*c*	$Pna2_1$	*Pbcn*
a (Å)	28.6491(3)	25.15270(10)	22.1968(12)
b (Å)	13.40210(10)	13.16760(10)	17.6144(14)
c (Å)	22.8635(2)	21.64810(10)	15.2764(7)
α (°)	90	90	90
β (°)	102.2200(10)	90	90
γ (°)	90	90	90
Volume ($Å^3$)	8579.72(14)	7169.87(7)	5972.8(6)
Z	4	4	4
ρ_{calc} (g/cm^3)	1.592	1.506	1.375
μ (mm^{-1})	2.760	3.778	2.767
F(000)	4132.0	3332.0	2580.0
Crystal size (mm^3)	0.372 × 0.104 × 0.08	0.15 × 0.092 × 0.014	0.092 × 0.056 × 0.04
Radiation	Cu Kα (λ = 1.54184)	Cu Kα (λ = 1.54184)	Cu Kα (λ = 1.54184)
2θ range for data collection (°)	6.314 to 156.048	7.028 to 156.322	6.406 to 153.34
Index ranges	$-35 \le h \le 36$ $-16 \le k \le 16$ $-28 \le l \le 22$	$-19 \le h \le 31$ $-16 \le k \le 16$ $-26 \le l \le 27$	$-26 \le h \le 26$ $-21 \le k \le 19$ $-13 \le l \le 18$
Reflections collected	58313	90388	22962
Independent reflections	9061 [R_{int} = 0.0400, R_{sigma} = 0.0240]	14701 [R_{int} = 0.0512, R_{sigma} = 0.0309]	5656 [R_{int} = 0.1330, R_{sigma} = 0.0990]
Data/restraints/parameters	9061/843/756	14701/149/1119	5656/387/415
Goodness-of-fit on F^2	1.112	1.062	0.975
Final *R* indexes [$I \ge 2\sigma(I)$]	R_1 = 0.0581 wR_2 = 0.1590	R_1 = 0.0441 wR_2 = 0.1169	R_1 = 0.0853 wR_2 = 0.2042
Final *R* indexes [all data]	R_1 = 0.0600 wR_2 = 0.1607	R_1 = 0.0508 wR_2 = 0.1232	R_1 = 0.1676 wR_2 = 0.2532
Largest diff. peak/hole / e $Å^{-3}$	1.26/-1.31	0.43/-0.40	0.78/-0.26
Flack parameter	-	0.058(5)	-

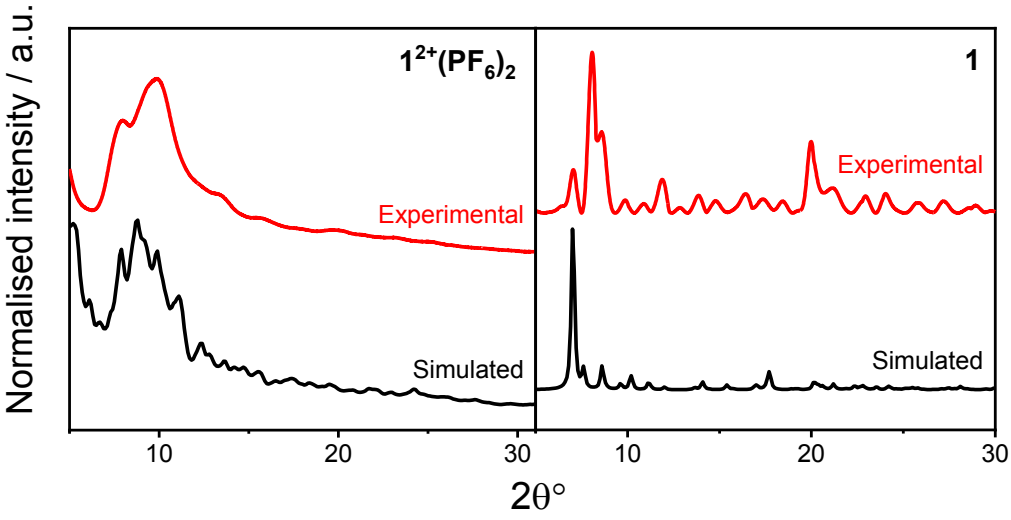

Figure S10. Experimental ($\mathbf{1}^{2+}(\mathbf{PF_6})_2$·0.5DCE·0.5iPr$_2$O and **1**·0.8EtOH; at room temperature) vs simulated PXRD patterns from respective crystal structures ($\mathbf{1}^{2+}(\mathbf{PF_6})_2$·2.5DCE·1.5iPr$_2$O at 100 K and **1**·2.5THF·pentane at 100 K).

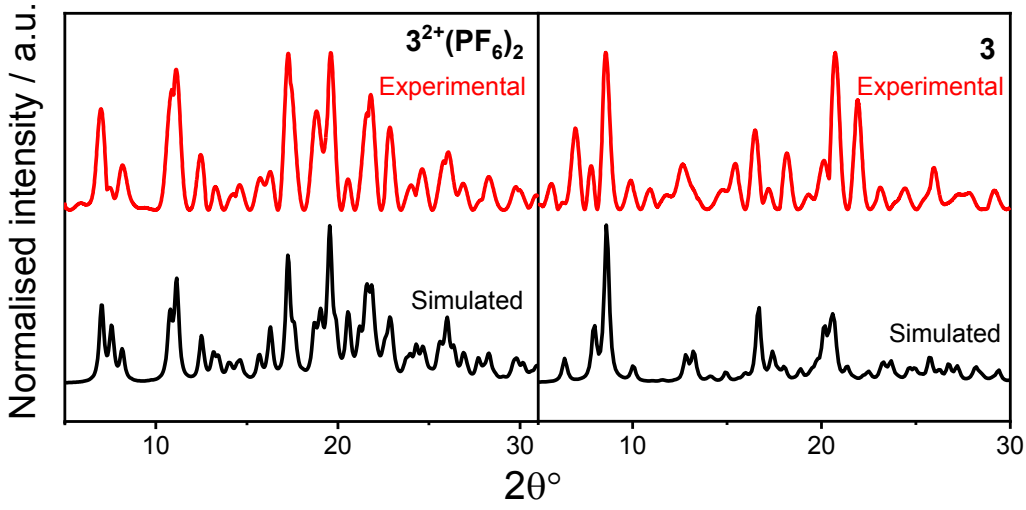

Figure S11. Experimental ($\mathbf{3}^{2+}(\mathbf{PF_6})_2$·DCE and **3**·EtOH; at room temperature) vs simulated PXRD patterns from respective crystal structures ($\mathbf{3}^{2+}(\mathbf{PF_6})_2$·(DCE) at 100 K and **3** at 120 K).

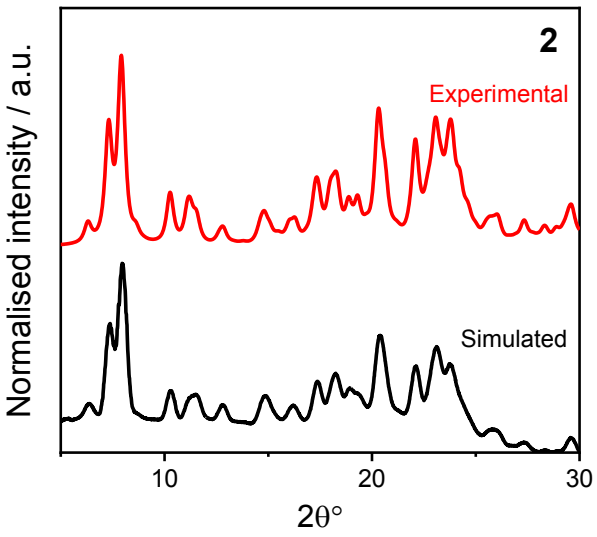

Figure S12. Experimental (**2**; at room temperature) vs simulated PXRD patterns from respective crystal structures (**2**·tol); at 100 K).

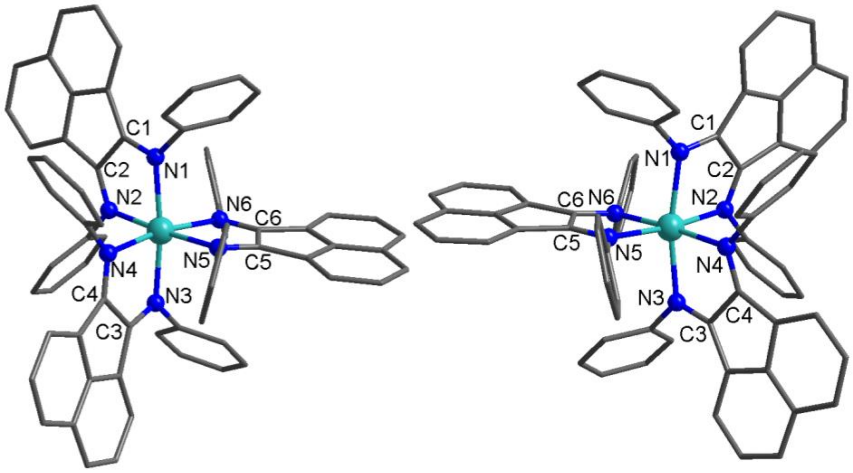

Figure S13. Molecular structure of the independent complexes A (left) and B (right) of $\mathbf{1}^{2+}$ in $\mathbf{1}^{2+}\mathbf{(PF_6)_2}\cdot 2.5DCE\cdot 1.5iPr_2O$ at 100 K with relevant atoms labelled. Hydrogen atoms, solvent molecules and PF_6^- anions have been omitted for clarity. Colour code: C (dark grey), N (blue), Co (light blue).

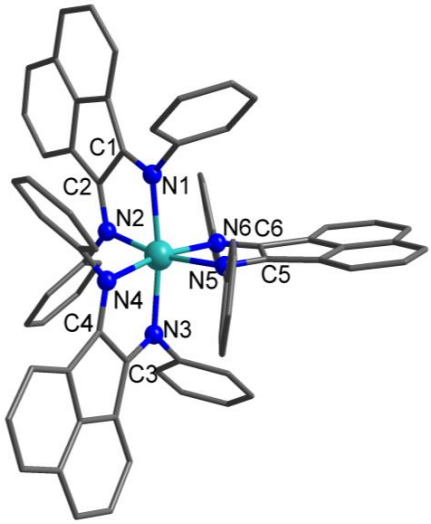

Figure S14. Molecular structure of $\mathbf{1}^{+}$ in $\mathbf{1}^{+}\mathbf{(PF_6)}\cdot 2Et_2O\cdot 0.6MeCN$ at 100 K with relevant atoms labelled. Hydrogen atoms, solvent molecules and PF_6^- anions have been omitted for clarity. Colour code: C (dark grey), N (blue), Co (light blue).

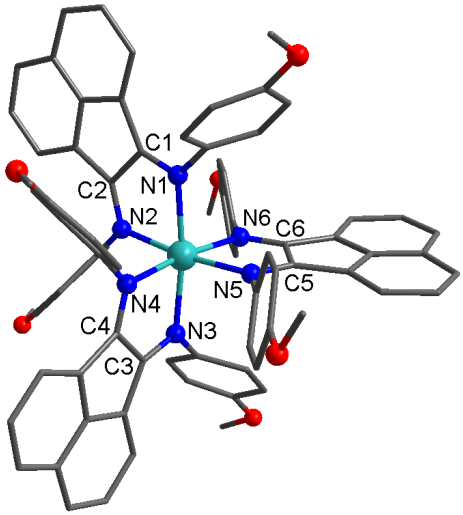

Figure S15. Molecular structure of $\mathbf{3}^{2+}$ in $\mathbf{3}^{2+}(\mathbf{PF_6})_2$·DCE at 100 K with relevant atoms labelled. Hydrogen atoms, solvent molecules and PF_6^- anions have been omitted for clarity. Colour code: C (dark grey), N (blue), O (red), Co (light blue).

Table S8. Bond valence sum (BVS) values[§] with bond distances used presented in Table 1 of the main text.

	$\mathbf{1^{2+}A}$	$\mathbf{1^{2+}B}$	$\mathbf{1^{+}}$	**1**	**2**	**3**	$\mathbf{3^{2+}}$
			Co^{II}				
Co-N1	0.33	0.31	0.33	0.33	0.35	0.34	0.32
Co-N2	0.34	0.33	0.35	0.34	0.33	0.29	0.34
Co-N3	0.33	0.31	0.35	0.33	0.35	0.35	0.32
Co-N4	0.31	0.30	0.34	0.34	0.33	0.35	0.34
Co-N5	0.31	0.33	0.32	0.37	0.33	0.34	0.33
Co-N6	0.31	0.30	0.31	0.37	0.33	0.29	0.33
BVS Value	1.93	1.88	2.00	2.08	2.00	1.97	1.98
			Co^{III}				
Co-N1	0.30	0.28	0.31	0.30	0.32	0.32	0.30
Co-N2	0.31	0.31	0.32	0.32	0.30	0.26	0.31
Co-N3	0.31	0.29	0.33	0.30	0.32	0.32	0.30
Co-N4	0.29	0.28	0.31	0.32	0.30	0.32	0.31
Co-N5	0.28	0.30	0.30	0.34	0.30	0.32	0.30
Co-N6	0.29	0.28	0.29	0.34	0.30	0.26	0.30
BVS Value	1.78	1.74	1.85	1.91	1.85	1.81	1.83

[§] Determined using equation $s = \exp[(r_0-r)/B]$ with values taken from literature ($B = 0.37$, $r_0(Co^{II}) = 1.72$, $r_0(Co^{III}) = 1.60$), with a value close to 2 indicating Co^{II} and 3 for Co^{III}.[16–18]

Table S9. Distortion and oxidation state parameters based on geometry optimized structures for different electromers of **1**, **2** and **3**, and values determined from experimental single-crystal X-ray diffraction data.

	1				**2**			**3**			
	HS-Co^{II}	**LS-Co^{II}**	**LS-Co^{III}**	**Exp**	**HS-Co^{II}**	**LS-Co^{III}**	**Exp**	**HS-Co^{II}**	**LS-Co^{II}**	**LS-Co^{III}**	**Exp**
SHAPE	1.214	1.116	0.327	1.180	1.344	0.352	1.119	1.214	1.129	0.324	1.216
Σ/°	87.33	65.21	43.80	75.30	94.3	43.81	74.8	87.73	66.79	44.93	74.9
Θ/°	262.0	215.2	133.0	239.9	280.0	138.0	242.0	262.8	214.56	132.9	237.2
BVS[c]	1.78	2.36	2.90	2.08	1.74	2.87	2.00	1.79	2.38	2.91	1.97

Estimation of the % fraction of LS-Co^{II}

To provide an estimate of the fraction of LS-Co^{II} present, we compared the % difference between Co-N_{ax} and Co-N_{eq} (averaged) lengths for the geometry optimized structures versus the experimentally obtained bond-lengths. Geometry optimized values indicate a 12 % difference between the Co-N_{ax} and Co-N_{eq} for the geometry optimized bond lengths of **1** and **3**. As we were not able to locate the geometry optimized LS-Co^{II} tautomer for **2**, we cannot determine this value, and so 12 % was used as a proxy. For the experimental data, the percentage difference is much smaller: 2 % for **1**, 1 % for **2**, and 4% for **3**. If we then consider the fraction based on geometry optimized versus experimental values (e.g. 4/12 for **3**) we can propose that the % fraction of LS-Co^{II} can be approximated to 16 % for **1**, 8 % for **2**, and 33 % for **3**. We stress that this is only an approximation but regardless, the experimental data suggest all neutral compounds involve the coordination of Co^{II} ruling out the LS-Co^{III}-(L$^{\bullet-}$) charge distribution at the measured temperature. Thus, we can propose that compounds **1**, **2** and **3** are isolated in the form [Co^{II}(Ar-BIAN$^{\bullet-}$)$_2$(Ar-BIAN)].

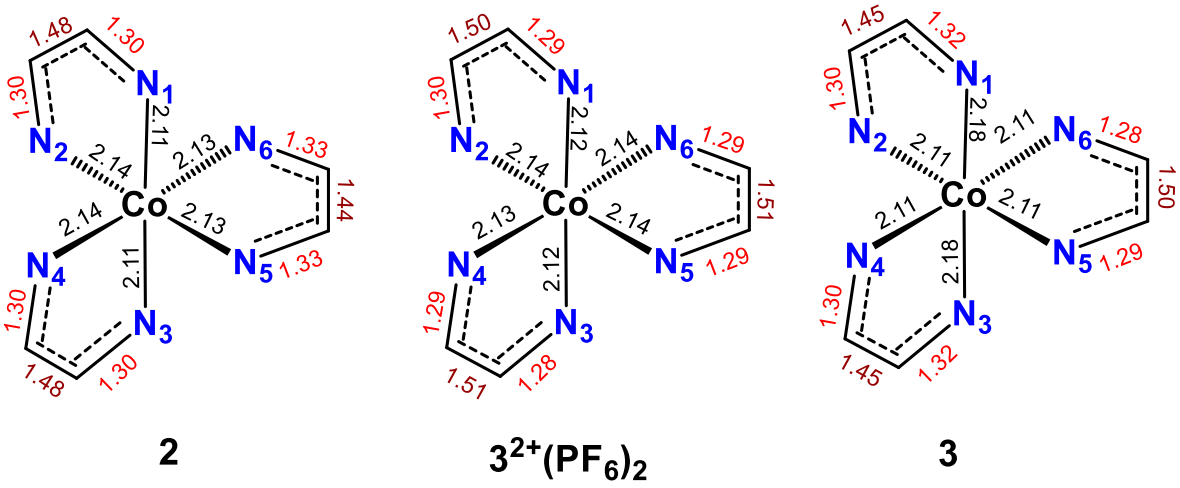

Figure S16. Comparison of bond lengths used to assign oxidation states for **2**, $\mathbf{3^{2+}(PF_6)_2}$ and **3**.

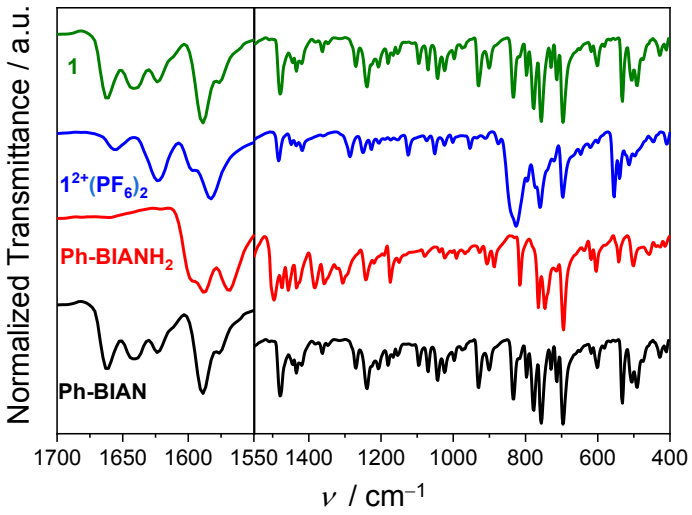

Figure S17. Solid state infrared spectra of free ligands Ph-BIAN, Ph-BIANH$_2$ and compounds $\mathbf{1^{2+}(PF_6)_2}$·(DCE) (iPr2O) and **1**·0.8(EtOH) at room temperature.

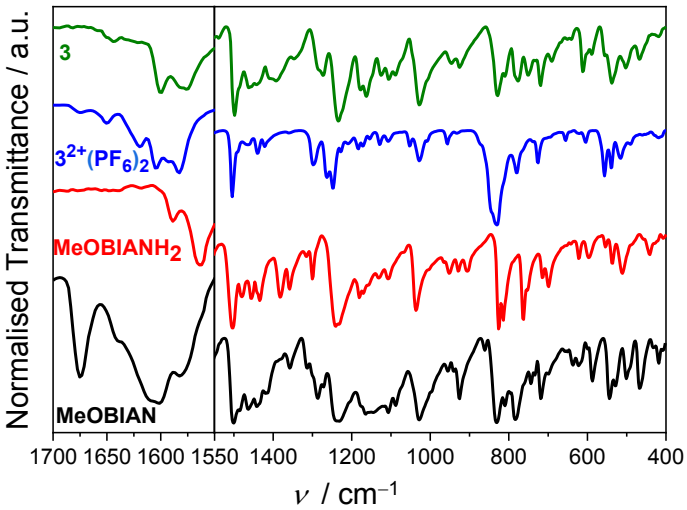

Figure S18. Solid state infrared spectra of free ligands MeO-BIAN, MeO-BIANH$_2$ and compounds **3**$^{2+}$**(PF$_6$)$_2$**·(DCE) and **3**·(EtOH) at room temperature.

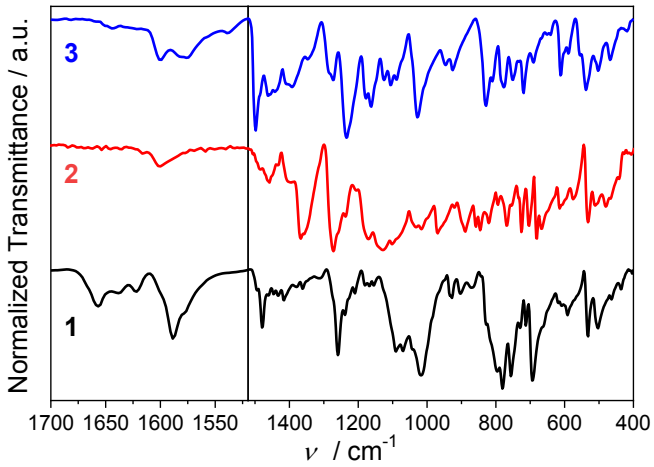

Figure S19. Solid state infrared spectra of neutral compounds **1**·0.8(EtOH), **2** and **3**·(EtOH) at room temperature.

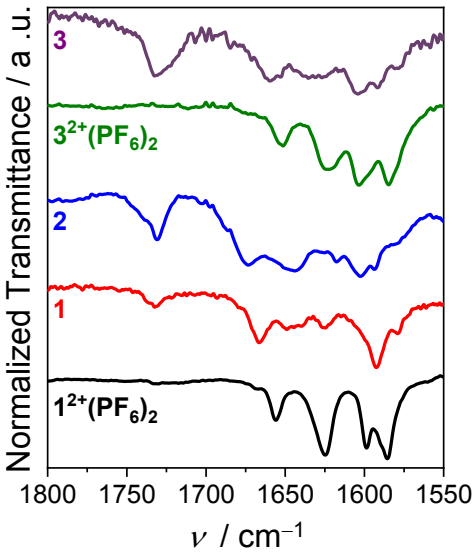

Figure S20. Static infrared spectrum in solution state (CH_2Cl_2) for compounds $\mathbf{1}^{2+}(\mathbf{PF_6})_2$, **1**, **2**, $\mathbf{3}^{2+}(\mathbf{PF_6})_2$ and **3** at room temperature.

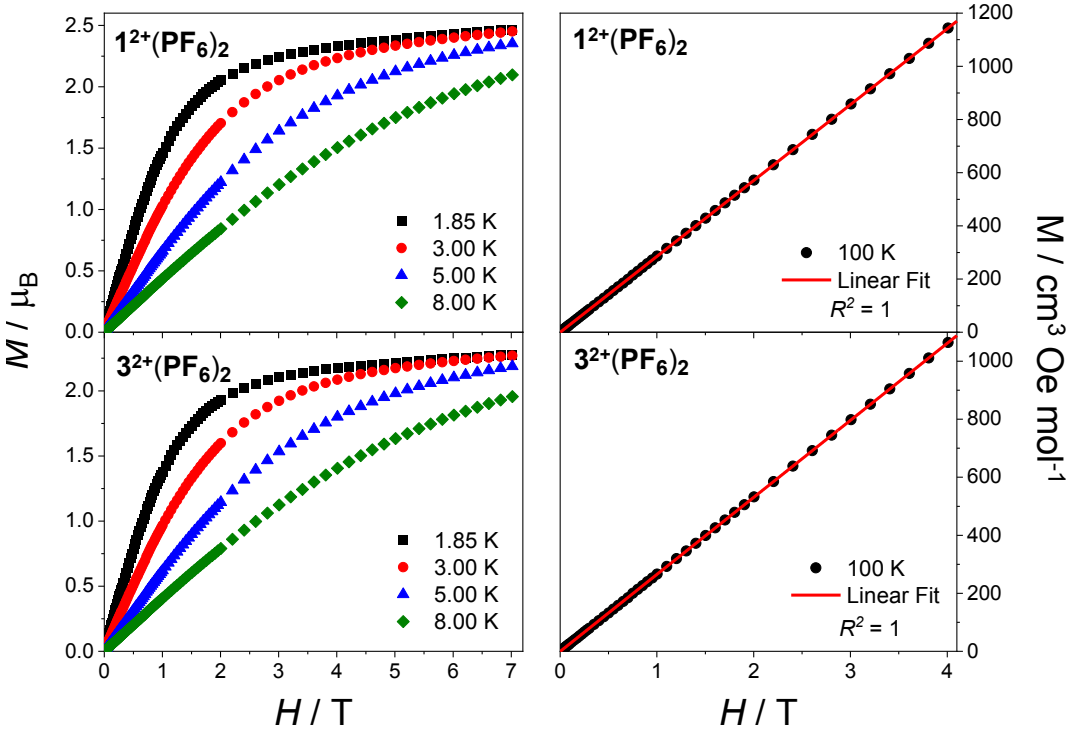

Figure S21. Variable field magnetization plots at 1.85, 3, 5, 8 K between 0-7 T (left) and at 100 K between 0–4 T (right) for compounds $\mathbf{1^{2+}(PF_6)_2}$ and $\mathbf{3^{2+}(PF_6)_2}$.

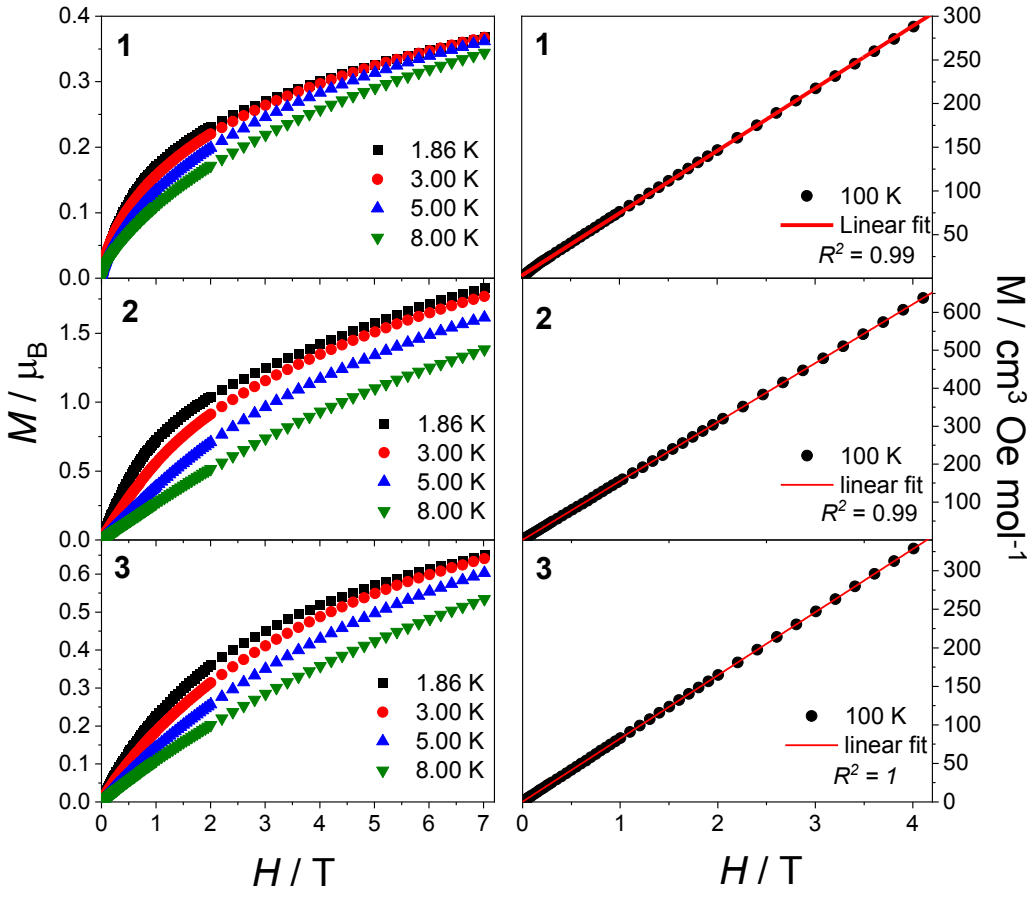

Figure S22. Variable field magnetization plots at 1.85, 3 K, 5 K, 8 K between 0–7 T (left) and at 100 K between 0–4 T (right) for compounds **1**·0.8EtOH, **2**, and **3**·EtOH

Table S10. Summary of observed transitions in the Vis-NIR region in MeCN and CH_2Cl_2 with associated assignments.

MeCN λ / nm	CH_2Cl_2 λ / nm	Assignment
	$1^{2+}(PF_6)_2$	
401	413	IL^0
984	-	$^4T_{1g} \rightarrow {}^4T_{2g}$
	$3^{2+}(PF_6)_2$	
406	408	IL^0
	1	
503	-	$IL^{\bullet-}$
572	440	$IL^{\bullet-}$
712	712	LMCT
1148	1148	IVCT
1505	1505	IVCT
	2	
513	514	$IL^{\bullet-}$
586	583	$IL^{\bullet-}$
736	736	LMCT
1594	-	IVCT
	3	
420	426	$IL^{\bullet-}$
758	746	LMCT
1090	-	IVCT
1524	1524	IVCT

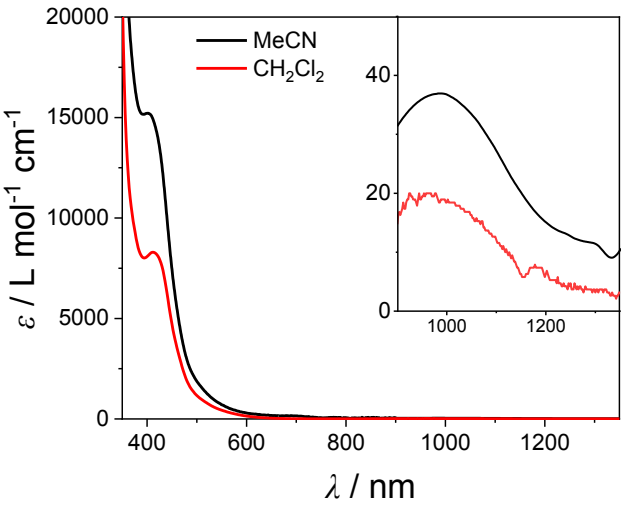

Figure S23. UV-Vis-NIR spectra of $\mathbf{1^{2+}(PF_6)_2}$ in MeCN and CH_2Cl_2 at room temperature. Inset emphasizes the IR region between 900-1350 cm^{-1}.

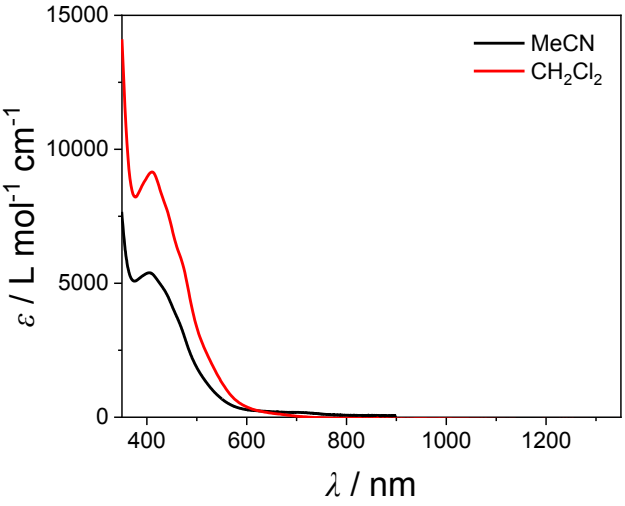

Figure S24. UV-Vis-NIR spectra of $\mathbf{3^{2+}(PF_6)_2}$ in MeCN and CH_2Cl_2 at room temperature.

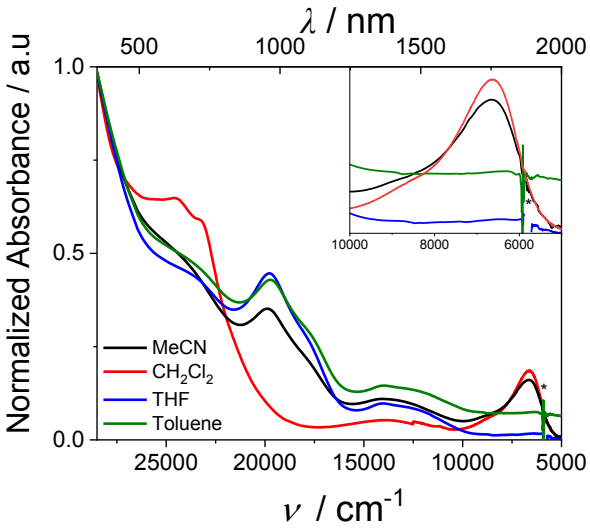

Figure S25. UV-Vis-NIR spectra of **1** in in MeCN, CH_2Cl_2, THF, and toluene at room temperature. Inset emphasizes the NIR region between 10000 – 5000 cm^{-1}.

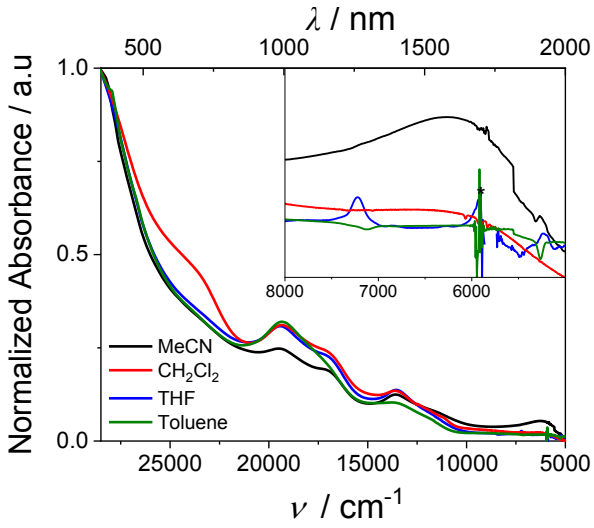

Figure S26. UV-Vis-NIR spectra of **2** in in MeCN, CH_2Cl_2, THF, and toluene at room temperature. Inset emphasizes the NIR region between 8000 – 5000 cm^{-1}.

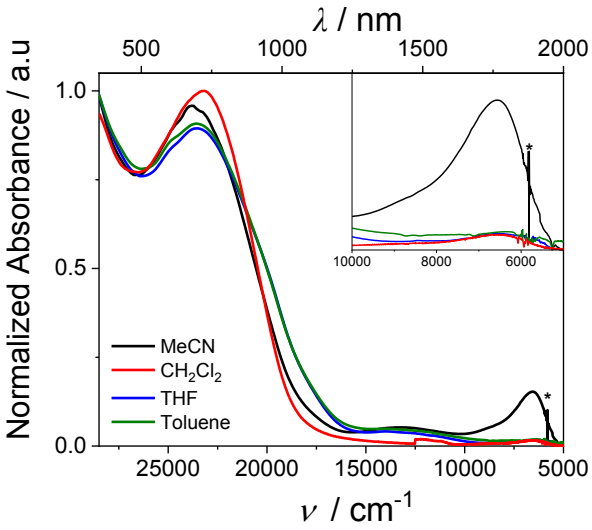

Figure S27. UV-Vis-NIR spectra of **3** in MeCN, CH_2Cl_2, THF, and toluene at room temperature. Inset emphasizes the NIR region between 10000 – 5000 cm^{-1}.

Further Details of Robin-Day Mixed-Valence Classification Analysis

The degree of electronic communication between the Ar-BIAN ligands can be measured by the Robin and Day mixed-valence (MV) class of ligands.[19] Robin-Day Class I mixed-valence systems have a fully localized electronic structure and therefore have no interactions and electron transfer between the centers, with H_{AB} = 0 cm^{-1}. Class II corresponds to a localized electronic structure and solvent environment, and as such intervalence charge transfer is intimately linked to the reorganization energy, λ (corrected for the emerging charge delocalization), and which in turn is linked to the energy of the optical charge transfer band ($h\nu_{max} = \lambda$); for Class II systems $H_{AB} \leq \lambda/2$. There is a non-zero H_{AB} and a IVCT band with energy $h\nu_{max}$ and full width at half maximum, $\Delta\nu_{1/2}$. The IVCT band for class II are typically solvent-dependent ($\Delta\nu_{max}$ > 200 cm^{-1} for a range of dielectric constant of 30), weak in intensity (ε_{max} < 5000 L mol^{-1} cm^{-1}), broad ($\Delta\nu_{1/2}$ > 2000 cm^{-1}), H_{AB} < 800 cm^{-1}, and $2H_{AB}/\nu_{max} \ll 1$.[20–23] As the electronic coupling term increases, the thermal barrier to charge transfer in the ground state decreases, and the system becomes increasingly delocalized. In the limit where there is no ground state barrier to charge transfer, the system moves to Class III, and the coupling term can be simply related to the (solvent independent) IVCT band energy as $2H_{AB} = h\nu_{max}$, with the IVCT band displaying a pronounced asymmetric shape with a cut-off on the low-energy side. Meyer and colleagues have identified an intermediate case (Class II-III), distinct from the Class II/Class III boundary, in which the redox sites are localized (valence trapped) but electron transfer is faster than the rate of solvent reorganization.[20,24] This leads to a curious scenario in which the IVCT band offers the symmetric shape associated with Class II, but is not solvatochromic. Class II-III correspond to localized electronic structure and averaged solvent interactions, with $0.7 < 2H_{AB}/\nu_{max} < 1$, and class III represent electronic and solvent delocalization with $2H_{AB}/\nu_{max} \gg 1$. Both MV class II-III and III contain IVCT that are solvent independent ν_{max} <

200 cm^{-1} for a range of dielectric constant of 30), narrow ($\Delta\nu_{1/2}$ < 2000 cm^{-1}), and intense (ε_{max} > 5000 L mol^{-1} cm^{-1}).[21]

Class II species obey:[24]

$$(\Delta\upsilon_{1/2}°)^2 = 16k_{\mathrm{B}}T\nu_{\mathrm{max}}\ln 2 \qquad \text{(eq. 1)}$$

where $\Delta\nu_{1/2}°$ is the theoretical bandwidth at half maximum (in cm^{-1}), k_B is the Boltzmann constant and T is the temperature in K. For a spectrum measured at 298 K, this gives:

$$\Delta\upsilon_{1/2}° = 47.93\sqrt{\nu_{max}} \qquad \text{(eq. 2)}$$

The MV class can be determined by parameter Γ, given by:

$$\Gamma = 1 - (\Delta\upsilon_{1/2})/(\Delta\upsilon_{1/2}°) \qquad \text{(eq. 3)}$$

where $\Gamma < 0.5$ indicate class III, $\Gamma \approx 0.5$ indicate class II-III and $\Gamma > 0.5$ indicate class II.

In the class III limit, H_{AB} can be calculated using:[25]

$$H_{AB} = 1/2\nu_{1/2} \qquad \text{(eq. 4)}$$

In general, H_{AB} is 0 for MV class I, up to ~800 cm^{-1} for MV class II,[22,23] ~1000-2000 cm^{-1} for MV class II-III[22,25] and 2500-5500 cm^{-1} for MV class III.[22,23]

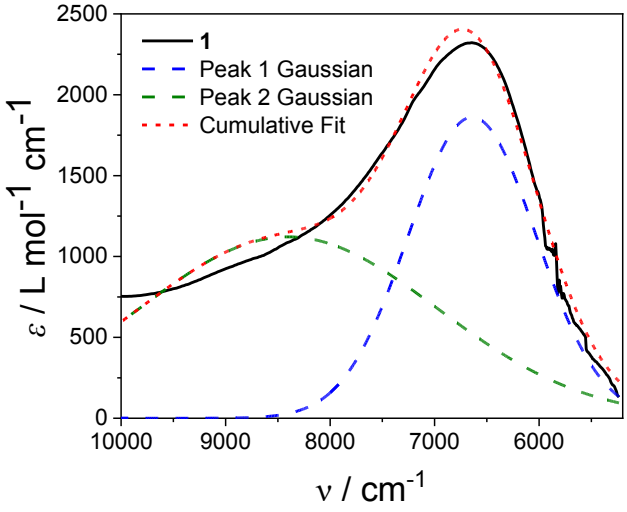

Figure S28. NIR spectrum of **1** in MeCN with a two peak Gaussian fit (R^2 = 0.987).

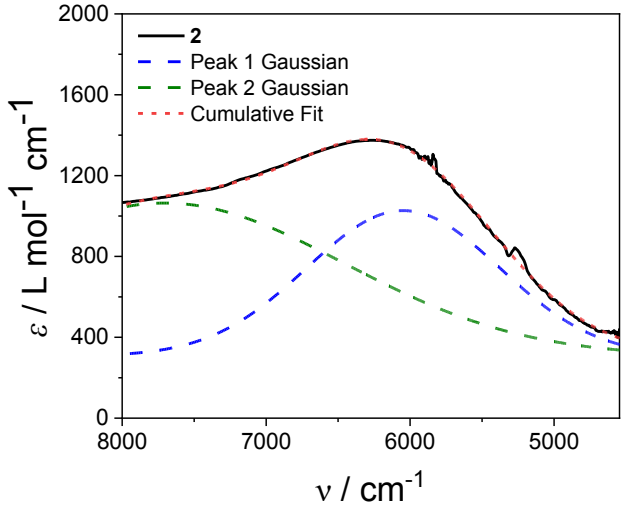

Figure S29. NIR spectrum of **2** in MeCN with a two peak Gaussian fit (R^2 = 0.998).

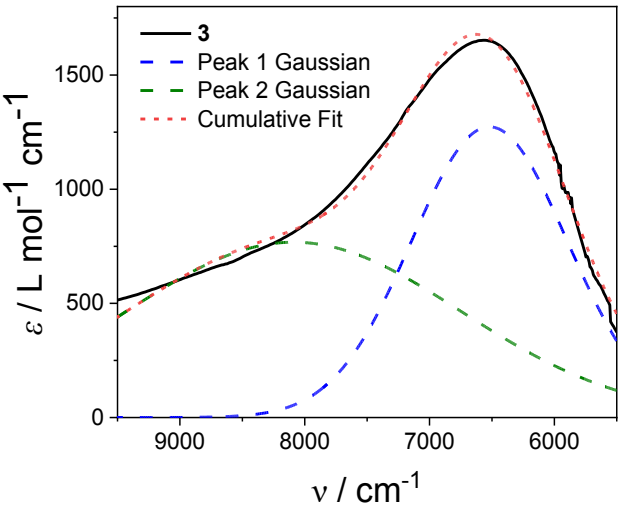

Figure S30. NIR spectrum of **3** in MeCN with a two peak Gaussian fit (R^2 = 0.993).

Table S11. Parameters relating to the analysis of the IVCT band for compounds **1**, **2** and **3** in MeCN.

	ν_{max} / cm^{-1}	$\Delta\nu_{1/2}$ / cm^{-1}	$\Delta\nu_{1/2}°$ / cm^{-1}	Γ	H_{AB} / cm^{-1}
1	6640(6)	1441(3)	3906	0.63	721
	8400(91)	3353(313)	4393	0.24	1677
2	6048(17)	1579(92)	3727	0.58	790
	7704(133)	2938(712)	4207	0.30	1469
3	6520(6)	1471(37)	3870	0.62	736
	8088(112)	3153(338)	4311	0.27	1577
1^+ spectroelectrochemistry	6610(2)	1310(10)	3897	0.66	655
	7930(30)	2830(70)	4268	0.34	1415
3^+ spectroelectrochemistry	6552(2)	1350(14)	3880	0.65	675
	7973(45)	3010(100)	4280	0.30	1505

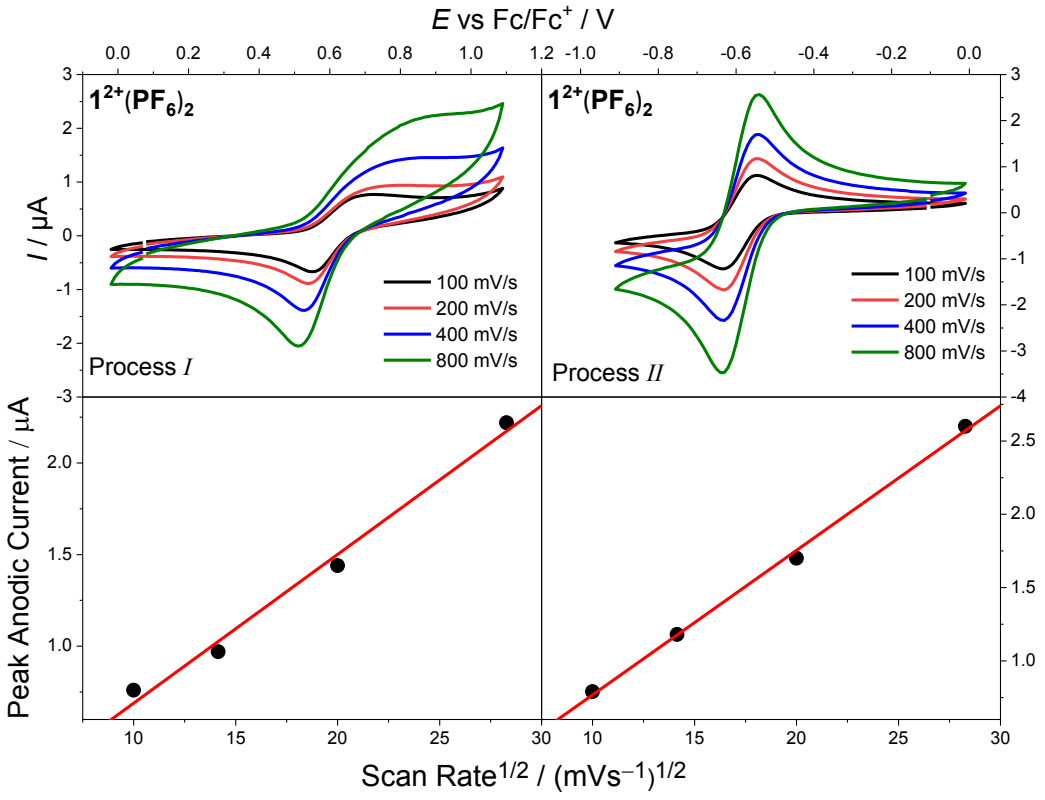

Figure S31. Cyclic voltammograms of processes *I* and *II* of $\mathbf{1^{2+}(PF_6)_2}$ in CH_2Cl_2 at various scan rates (mV s^{-1}) and plot of the I_{pa} against the square root of the scan rate for processes *I* and *II* with the linear fit shown as solid red line.

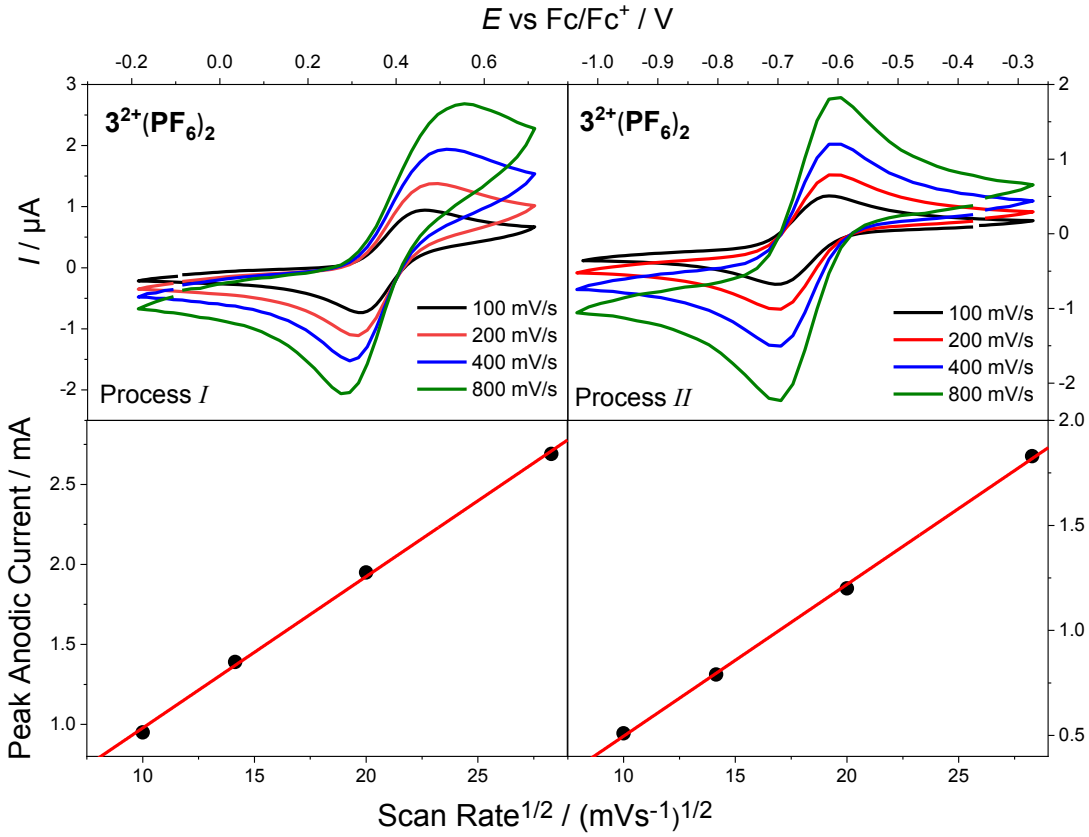

Figure S32. Cyclic voltammograms of processes *I* and *II* of $\mathbf{3^{2+}(PF_6)_2}$ in CH_2Cl_2 at various scan rates (mV s^{-1}) and plot of the I_{pa} against the square root of the scan rate for processes *I* and *II* with the linear fit shown as solid red line.

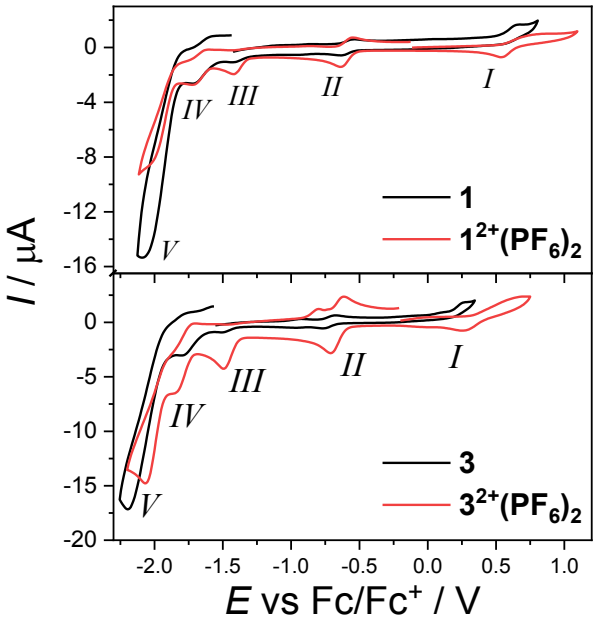

Figure S33. Cyclic voltammograms (0.1 M NBu_4PF_6 / CH_2Cl_2) of **1** and **3** (black) and related $\mathbf{1^{2+}(PF_6)_2}$ and $\mathbf{3^{2+}(PF_6)_2}$ (red) at 100 mV s^{-1}.

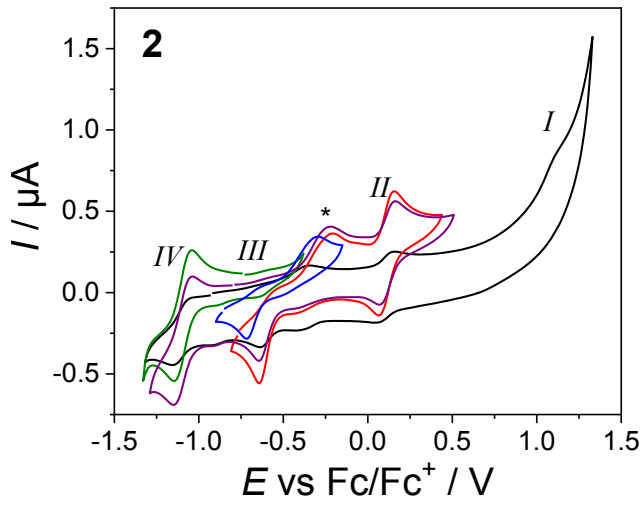

Figure S34. Cyclic voltammograms (0.1 M NBu_4PF_6 / CH_2Cl_2) at scan rate of 100 mV s^{-1} for compound **2**. The colored lines plot the voltammograms measured with a switching potential immediately past each process. The process marked * appears when cycling through process *III* and appears in all measured neutral compounds.

Table S12. Assignments of absorbances observed in spectroelectrochemistry in CH_2Cl_2.

E / cm^{-1}	λ / nm	Assignment	E / cm^{-1}	λ / nm	Assignment
$1^{2+}(PF_6)$			**$3^{2+}(PF_6)$**		
30500	328	IL^0	36500	274	IL^0
24400	410	IL^0	30900	324	IL^0
			24400	410	IL^0
1st Oxidation (I)					
34300	292	IL^0	34000	294	IL^0
24500	408	IL^0	30000	333	IL^0
			24400	410	IL^0
			20800	480	IL^0
1st Reduction (II)					
30850	324	IL^0	39800	251	IL^0
20090	498	$IL^{\bullet-}$	33800	296	$IL^{\bullet-}$
13330	750	LMCT ($L^{\bullet-} \rightarrow Co^{II}$)	23300	429	IL^0
6630	1508	IVCT ($L^{\bullet-} \rightarrow L^0$)	13100	763	LMCT ($L^{\bullet-} \rightarrow Co^{II}$)
			6600	1515	IVCT ($L^{\bullet-} \rightarrow L^0$)

IL^0 = Ar-BIAN^0 intraligand transition, $IL^{\bullet-}$ = Ar-BIAN$^{\bullet-}$ intraligand transition, LMCT = ligand-to-metal-charge-transfer, IVCT = intervalence charge transfer

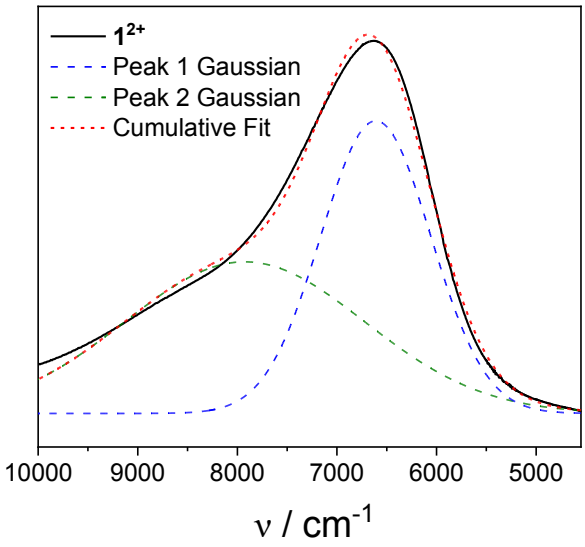

Figure S35. Fit of the resultant NIR features upon first reduction of $\mathbf{1}^{2+}$ (spectroelectrochemistry) in CH_2Cl_2 with two peak Gaussian fit ($R^2 = 0.997$).

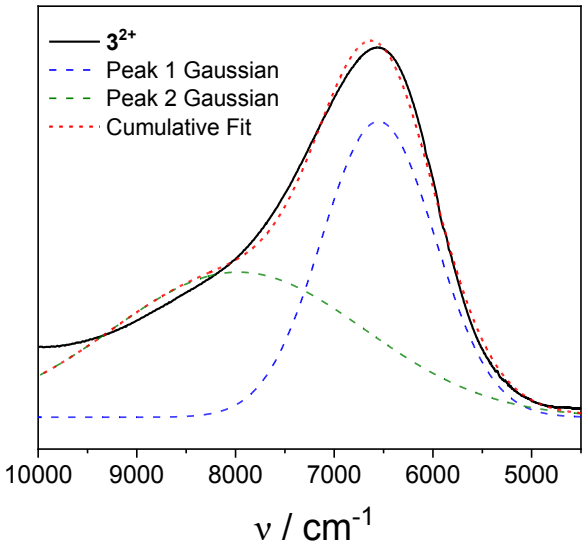

Figure S36. Fit of the resultant NIR features upon first reduction of $\mathbf{3}^{2+}$ (spectroelectrochemistry) in CH_2Cl_2 with two peak Gaussian fit ($R^2 = 0.996$).

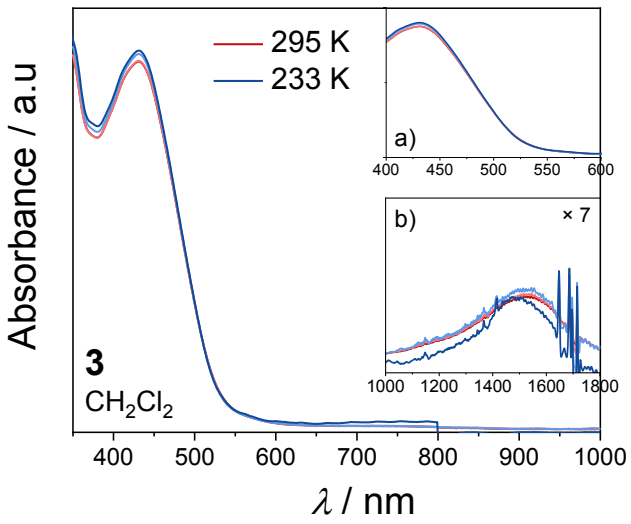

Figure S37. Temperature dependence of the UV−visible spectrum of **3** in CH_2Cl_2 from 295 K to 233 K, with inset (a) highlighting isosbestic points and (b) the IVCT band in the NIR region.

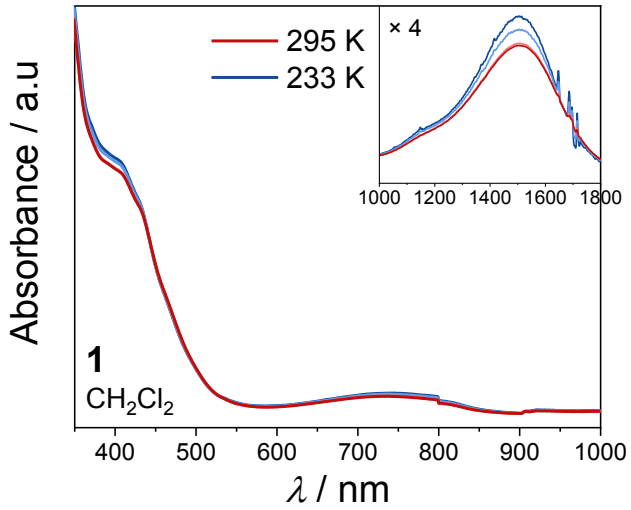

Figure S38. Temperature dependence of the UV−visible spectrum of **1** in CH_2Cl_2 from 295 K to 233 K, with inset showing the IVCT band in the NIR region.

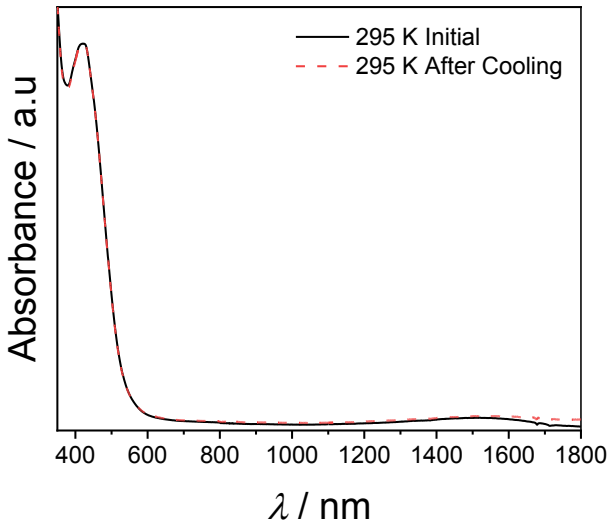

Figure S39. UV-Vis-NIR spectra of **3** in MeCN at 295 K measured immediately (black line) and after cooling to 243 K (red line).

References

(1) Cimino, A.; Moscatelli, F.; Ferretti, F.; Ragaini, F.; Germain, S.; Hannedouche, J.; Schulz, E.; Luconi, L.; Rossin, A.; Giambastiani, G. Novel Yttrium and Zirconium Catalysts Featuring Reduced Ar-BIANH2 Ligands for Olefin Hydroamination (Ar-BIANH$_2$ = Bis-Arylaminoacenaphthylene). *New J. Chem.* **2016**, *40*, 10285–10293.

(2) van Asselt, R.; Elsevier, C. J.; Smeets, W. J. J.; Spek, A. L.; Benedix, R. Synthesis and Characterization of Rigid Bidentate Nitrogen Ligands and Some Examples of Coordination to Divalent Palladium. X-ray Crystal Structures of Bis(P-tolylimino) Acenaphthene and Methylchloro [Bis(o,o′-diisopropylphenyl-imino) Acenaphthene] Palla. *Recl. des Trav. Chim. des Pays-Bas* **1994**, *113*, 88–98.

(3) Viganò, M.; Ferretti, F.; Caselli, A.; Ragaini, F.; Rossi, M.; Mussini, P.; Macchi, P. Easy Entry into Reduced Ar-BIANH$_2$ Compounds: A New Class of Quinone/Hydroquinone-Type Redox-Active Couples with an Easily Tunable Potential. *Chem. - Eur. J.* **2014**, *20*, 14451–14464.

(4) Twin, M. Twin Samples with CrysAlisPro: Experiments, Unit Cell Finding, Data Reduction and Post Corrections. *Acta Crystallogr A* **2012**, *68*, S83.

(5) Cowieson, N. P.; Aragao, D.; Clift, M.; Ericsson, D. J.; Gee, C.; Harrop, S. J.; Mudie, N.; Panjikar, S.; Price, J. R.; Riboldi-Tunnicliffe, A.; Williamson, R.; Caradoc-Davies, T. MX1: A Bending-Magnet Crystallography Beamline Serving Both Chemical and Macromolecular Crystallography Communities at the Australian Synchrotron. *J. Synchrotron Radiat.* **2015**, *22*, 187–190.

(6) Sheldrick, G. M. SHELXT – Integrated Space-Group and Crystal-Structure Determination.

Acta Crystallogr. Sect. A Found. Adv. **2015**, *71*, 3–8.

(7) Dolomanov, O. V.; Bourhis, L. J.; Gildea, R. J.; Howard, J. A. K. K.; Puschmann, H. OLEX2: A Complete Structure Solution, Refinement and Analysis Program. *J. Appl. Crystallogr.* **2009**, *42*, 339–341.

(8) Krejčik, M.; Daněk, M.; Hartl, F. Simple Construction of an Infrared Optically Transparent Thin-Layer Electrochemical Cell. *J. Electroanal. Chem. Interfacial Electrochem.* **1991**, *317*, 179–187.

(9) Frisch, M. J.; Trucks, G. W.; Schlegel, H. B.; Scuseria, G. E.; Robb, M. A.; Cheeseman, J. R.; Scalmani, G.; Barone, V.; Petersson, G. A.; Nakatsuji, H.; Li, X.; Caricato, M.; Marenich, A. V.; Bloino, J.; Janesko, B. G.; Gomperts, R.; Mennucci, B.; Hratch, D. J. Gaussian 16 Rev. C.01.

(10) Tao, J.; Perdew, J. P.; Staroverov, V. N.; Scuseria, G. E. Climbing the Density Functional Ladder: Nonempirical Meta–Generalized Gradient Approximation Designed for Molecules and Solids. *Phys. Rev. Lett.* **2003**, *91*, 146401.

(11) Staroverov, V. N.; Scuseria, G. E.; Tao, J.; Perdew, J. P. Comparative Assessment of a New Nonempirical Density Functional: Molecules and Hydrogen-Bonded Complexes. *J. Chem. Phys.* **2003**, *119*, 12129–12137.

(12) Shoji, M.; Koizumi, K.; Kitagawa, Y.; Kawakami, T.; Yamanaka, S.; Okumura, M.; Yamaguchi, K. A General Algorithm for Calculation of Heisenberg Exchange Integrals *J* in Multispin Systems. *Chem. Phys. Lett.* **2006**, *432*, 343–347.

(13) Chemcraft. 2013.

(14) Genix, P.; Jullien, H.; Le Goas, R. Estimation of Hammett Sigma Constants from Calculated Atomic Charges Using Partial Least Squares Regression. *J. Chemom.* **1996**, *10*, 631–636.

(15) Hammett, L. P. The Effect of Structure upon the Reactions of Organic Compounds. Temperature and Solvent Influences. *J. Chem. Phys.* **1936**, *4*, 613–617.

(16) Camargo, P. H. C. The Chemical Bond in Inorganic Chemistry: The Bond Valence Model, 2nd Ed. *J. Mater. Sci.* **2017**, *52*, 9959–9962.

(17) Brown, I. D.; Altermatt, D. Bond-Valence Parameters Obtained from a Systematic Analysis of the Inorganic Crystal Structure Database. *Acta Crystallogr. Sect. B Struct. Sci.* **1985**, *244*, 244–247.

(18) Brese, N. E.; O'Keeffe, M. Bond-Valence Parameters for Solids. *Acta Crystallogr. Sect. B Struct. Sci.* **1991**, *47*, 192–197.

(19) Robin, Melvin B.; Day, P. Mixed Valence Chemistry-A Survey and Classification. *Adv. Inorg. Chem. Radiochem.* **1967**, *10*, 247–422.

(20) D'alessandro, D. M.; Keene, F. R. Current Trends and Future Challenges in the Experimental, Theoretical and Computational Analysis of Intervalence Charge Transfer (IVCT) Transitions. *Chem. Soc. Rev.* **2006**, *35*, 424–440.

(21) Arnold, A.; Sherbow, T. J.; Sayler, R. I.; Britt, R. D.; Thompson, E. J.; Muñoz, M. T.; Fettinger, J. C.; Berben, L. A. Organic Electron Delocalization Modulated by Ligand Charge States in $[L_2M]^{n-}$ Complexes of Group 13 Ions. *J. Am. Chem. Soc.* **2019**, *141*, 15792–15803.

(22) Tahara, K.; Kadowaki, T.; Kikuchi, J.; Ozawa, Y.; Yoshimoto, S.; Abe, M. Synthesis and Characterization of a New Series of Binuclear Pd(II) Biscatecholato Complexes: Non-

Innocent Ligand-Based Approach to a Wide Range of Variation in Near-Infrared Absorptions of Mixed-Valence Complexes. *Bull. Chem. Soc. Jpn.* **2018**, *91*, 1630–1639.

(23) Moneo, Á.; Justino, G. C.; Carvalho, M. F. N. N.; Oliveira, M. C.; Antunes, A. M. M.; Bléger, D.; Hecht, S.; Telo, J. P. Electronic Communication in Linear Oligo(Azobenzene) Radical Anions. *J. Phys. Chem. A* **2013**, *117*, 14056–14064.

(24) Demadis, K. D.; Hartshorn, C. M.; Meyer, T. J. The Localized-to-Delocalized Transition in Mixed-Valence Chemistry. *Chem. Rev.* **2001**, *101*, 2655–2685.

(25) Loughrey, J. J.; Sproules, S.; McInnes, E. J. L.; Hardie, M. J.; Halcrow, M. A. Stable Mixed-Valent Radicals from Platinum(II) Complexes of a Bis(Dioxolene) Ligand. *Chem. - Eur. J.* **2014**, *20*, 6272–6276.